DEMONSTRATING THE IMPACT OF HIGH-FIDELITY POLARIZATION CALIBRATION ON HIGH-PRECISION PULSAR TIMING

by

Axl Floyd Rogers

Supervised by

Dr. Willem van Straten

A thesis submitted to Auckland University of Technology
in fulfilment of the requirements for the degree of
Masters of Science (Research)

Engineering, Computer & Mathematical Sciences
Institute for Radio Astronomy and Space Research
July 2020

"Two roads diverged in a yellow wood,
And sorry I could not travel both
And be one traveller, long I stood
And looked down one as far as I could
To where it bent in the undergrowth;

Then took the other, as just as fair,
And having perhaps the better claim,
Because it was grassy and wanted wear;
Though as for that the passing there
Had worn them really about the same,

And both that morning equally lay
In leaves no step had trodden black.
Oh, I kept the first for another day!
Yet knowing how way leads on to way,
I doubted if I should ever come back.

I shall be telling this with a sigh
Somewhere ages and ages hence:
Two roads diverged in a wood, and I—
I took the one less travelled by,
And that has made all the difference."

—Robert Frost

Abstract

Pulsars are highly magnetised, rapidly rotating neutron stars most frequently observed in radio wavelengths as their emitted beam path crosses an observer's line-of-sight. Millisecond pulsars (MSPs) demonstrate exceptional rotational stability over long timescales, rivalling the accuracy of the best terrestrial atomic clocks. Pulsar timing investigations can uncover a wealth of knowledge when high-precision, such as 1 μs or better, is achieved. In this thesis we present the novel approach of using a combination of state-of-the-art, high-precision pulsar timing tools for polarimetric calibration, mitigation of radio frequency interference (RFI), pulse time-of-arrival (TOA) analysis, and post processing into one pulsar processing pipeline (PSRPL). We have integrated the CoastGuard algorithm for RFI excision, performed instrumental calibration via Measurement Equation Template Matching (METM) followed by the Matrix Template Matching (MTM) algorithm for producing TOA estimates, and analysed the resulting TOAs with Tempo2 and Temponest. Our method has been applied to a sample of five pulsars that

are highly susceptible to calibration errors, as predicted by van Straten (2013): PSR J0437-4715, PSR J1022+1001, PSR J1045-4509, PSR J1600-3053, and PSR J1643-1224. Approximately 8 years of historical, observational data were analysed from the Parkes 64-m radio telescope's CASPSR backend (or instrument) for each pulsar in our sample. We have improved the timing residuals of all MSPs in our sample (e.g. achieving 60-ns timing residuals for PSR J0437-4715), with four out of five better than predicted, and shown that PSRPL is the optimal pipeline for high-precision pulsar timing over those using conventional methods (e.g. the Ideal Feed Assumption (IFA) and Scalar Template Matching (STM) algorithms). This result is an important step in the search for low frequency (nHz) Gravitational Waves (GWs) using Pulsar Timing Arrays (PTAs). We conclude by discussing possible further improvements to PSRPL and its intended application for both new and historical data from Parkes PTA instruments, as well as international telescopes such as MeerKAT, as we have demonstrated that PSRPL can improve timing results.

Contents

List of Figures

List of Tables

Attestation of Authorship

"I hereby declare that this submission is my own work or and that, to the best of my knowledge and belief, it contains no material previously published or written by another person (except where explicitly defined in the acknowledgements), nor material which to a substantial extent has been submitted for the award of any other degree or diploma of a university or other institution of higher learning."

Acknowledgements

First and foremost, I would like to give thanks to my supervisor and mentor, Dr Willem van Straten, Associate Professor for the Institute of Radio Astronomy and Space Research at Auckland University of Technology, who has played a vital role in my growth and education. van Straten's contagious enthusiasm for, and knowledge of, pulsar timing is an inspiration. His gentle encouragement and steadfast availability are always appreciated. A master of code and pulsar shaman. I am forever grateful for his supervision and for all the wisdom that he has imparted on me.

I would also like to thank the TEMPONEST expert Dr Aditiya Parthasarathy, post doctoral scholar at the Max Planck Institute for Radio astronomy, for his passionate participation, input and validation. I appreciate your precious time and the invaluable knowledge shared.

I would also like to acknowledge Professor Sergei Gulyaev and the team in the Institute of Radio Astronomy and Space Research at Auckland University of Technology. I am gratefully indebted to you for all your support and

providing the perfect environment for a young man's curious mind to thrive as he ponders the great wonders and mysteries of the cosmos.

Finally, I wish to express my very profound gratitude to my mother and grandmother, who have provided me with support and encouragement throughout my years of study. This accomplishment would not have been possible without you. Thank you.

Chapter 1

Introduction

Throughout this chapter, the most important topics relevant to this thesis will be discussed in detail to provide the reader with a comprehensive understanding of the subject matter. Each topic will be provided in an order that is aimed to gradually guide the reader toward the main aims and objectives considered in this research. Section §**1.1** will provide the reader with an overview of the processes associated with star formation, their life, their death via supernova explosions, and the nature of their afterlife counterparts (i.e. White Dwarfs (WD), Neutron Stars (NS) and Black Holes (BH)). Section §**1.2** details the nature of Gravitational Waves (GW) - ripples in the fabric of space-time predicted by Albert Einstein in his theory of General Relativity (GR), the current and near-future instruments capable of detecting these GWs, and the latest discoveries obtained with these instruments. Section §**1.3** discusses pulsar timing and the process of

data analysis including the implementation of timing conversions and delay corrections which are required for retrieving relevant information from pulsar observation data. Section §**1.4** dives deeper into the importance of GR and the strong field tests attainable by observing NS and/or Super Massive Black Hole (SMBH) mergers. And finally, Section §**1.5** will wrap the chapter with a detailed description of both the scope and purpose of this research.

1.1 Compact Stars

A single glimpse of the night sky by an unaided eye is enough to provide anyone with an awareness of the undeniably vast abundance of stars presiding in the heavens above. Astronomy - the study of these stars as well as other observable celestial objects and phenomena in the cosmos - has been considered one of the most ancient of the natural sciences, playing an imperative role in religion, culture, and navigation since the very beginning of recorded ancient civilisation.

Let us fast forward to when the first optical telescope was invented in 1608 by Hans Lipperhey to magnify objects by three times their original size. A year later, in 1609, astronomer Galileo Galilei improved upon this model to allow twenty times the magnification. Galileo used this device to closely observe the Sun, Moon, and some planets, for which he recorded their

positions and other physical characteristics. These findings justified Nicolaus Copernicus's theory from 1532 that the solar system was heliocentric - the Earth and other planets revolve around the Sun [27]. This invention also led to Galileo's famous discovery of Jupiter's four moons: Callisto, Europa, Io, and Ganymede [39]. Issac Newton later discovered the laws of motion from which he derived the theory of Universal Gravitation in 1687 to describe the forces that act on all matter in the universe as a function of both mass and distance [82]. Albert Einstein did not believe gravity to be a force, instead suggesting in his widely accepted 1916 theory of GR that this effect is a distortion in the fabric of space-time [34].

These inventions, theories, centuries of improved instrumentation, and the extension of observational wavelengths beyond optical into other bands of the electromagnetic (EM) spectrum (i.e. radio, x-ray, γ-ray, and infrared), as well as many great discoveries since, have led to the knowledge that billions of stars (including our own Sun) - large, incandescent orbs of plasma - inhabit our galaxy, the Milky Way. Furthermore, we are now fully aware that space consists of billions of galaxies, each filled with their own great scores of stars, populating the farthest reaches of the known universe. Stellar evolution describes the complex nature and processes around the birth, life and death of stars which is heavily influenced by a star's mass and the transformations of this mass that occur with age [108].

1.1.1 Stellar Evolution

Within the heart of hot, dense molecular clouds of accumulated interstellar gas and dust, the primary stage of stellar evolution begins. These slow-rotating stellar nurseries contain an abundance of Hydrogen and Helium, the primal fuel that helps young stars flourish [78]. Star forming regions become incredibly compact, increasing in both rotational speed and temperature until the clouds start to collapse under their own weight, the primary stage in stellar evolution [131]. The heat and pressure will continue to rise until the thermonuclear process of nuclear fusion - the release of atomic energy by combining lighter elements to create heavier atoms - can occur which ignites the core and marks the birth of a new star [109]. The outflow of energy from the stellar core, created during this process, maintains "hydrostatic equilibrium" by countering the inward pressure of gravity and preventing further collapse under its own weight [133].

The several billion stars in our Milky Way galaxy are comprised of varying ages, sizes, and masses. Stellar lifetime can be determined from its initial mass, e.g. greater mass stars typically have shorter life cycles as they burn through their fuel supply faster [108]. Standard main-sequence stars like our Sun with solar mass $M_{\odot} \sim 2 \times 10^{30}$ kg can live for millions to billions of years and shine bright due to the continued nuclear fusion occurring deep within their cores [78]. Stellar attributes such as magnitude, luminosity, and temperature determine its position on the Hertzsprung-Russell (H-R)

diagram (see Figure §**1.1**). The H-R diagram was created by Enjar Hertzsprung and Henry Russell in 1914 to show the relationship between a star's absolute magnitude (intrinsic brightness) and its colour. The colour index is closely related to the star's surface temperature, with hottest to coldest stars positioned from left to right [93]. These diagrams are also useful in depicting the phase of stellar evolution for main-sequence stars [99]. At the end of a long life, after many millions of years, a star will have exhausted the extent of its Hydrogen supply. Once the majority of these lighter chemicals are depleted, energy will cease to flow, triggering the final phase of stellar evolution - an inevitable demise. As the last nuclear fusions occur, where elements up to Iron can form, a star will commence swelling and reddening, becoming a red giant star [109]. At this stage, a star is incapable of generating enough energy to maintain hydrostatic equilibrium [131]. The fusion history of most red giants only goes as far as converting Helium to Carbon and Oxygen, whereas red supergiants will continue to fuse elements until an Iron core is produced. At this point, for the red supergiants, their inner star has an onion-like cross section of increasingly large atoms (from hydrogen and helium in the outer-most "atmosphere" to iron and nickel in the inner-most core). When this degenerate core (supported only by electron degeneracy) can no longer support itself against gravity, the stars core will then collapse under its own weight, resulting in one of the most chaotic events to occur throughout the expanse of the cosmos [133], a supernova - a violent explosion accompanied by a

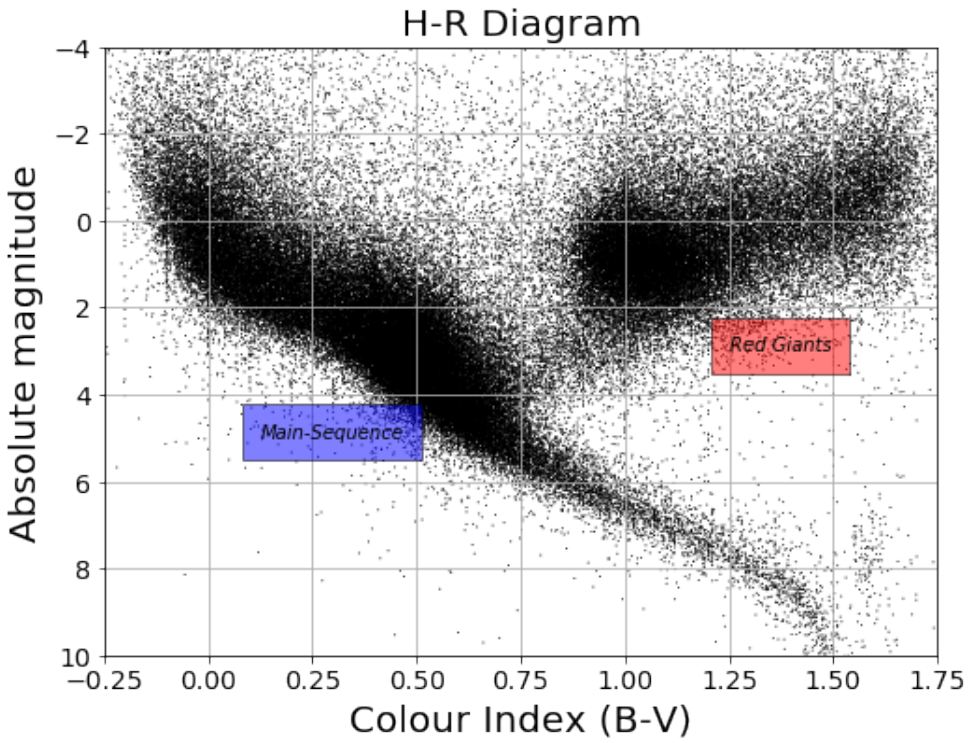

Figure 1.1: **An H-R diagram with data from the Hipparchus data catalogue [93]. The diagram shows the stellar evolution of main-sequence and red giant stars as a function of absolute magnitude against colour index (B-V). A stars location on the diagram can be used to indicate its luminosity, spectral type, colour, temperature, mass and age [99].**

great burst of light as luminous as 10 billion Suns - expelling all its chemically rich nutrients throughout the surrounding universe. These nutrients may eventually seed molecular clouds where new stellar life will begin to form [108].

Depending on the mass of the red supergiant star, either a NS or BH is

formed during supernovae. However, WDs are not formed during supernovae. Rather, most form from red giants that blow away their shell in a stellar wind (forming a planetary nebula) as the core continues to cool and "settle" into a compact configuration supported only by electron degeneracy pressure, but there is no implosion/explosion like the one that forms a NS or BH. For a star with similar or less mass than our Sun, it is destined to become a WD - a dense stellar core about the size of Earth [131]. Above this mass, electron degeneracy pressure is not capable of preventing further collapse of the star. However, neutron degeneracy pressure prevents further collapse of progenitor stars with masses between 1.4 $M_{\odot}$ and less than 3 $M_{\odot}$ the Tolman-Oppenheimer-Volkoff limit [121][85] - the upper bound - supporting the formation of a NS [131]. For any star greater than 3 $M_{\odot}$, no known force can prevent further collapse, resulting in a stellar mass BH - the densest known object to reside within the universe after SMBHs like Sagittarius A* at the centre of our Milky Way galaxy [108].

1.1.2 The Nature of Neutron Stars

NS are stellar remnants that originate within the aftermath of supernova explosions, the dying bursts of main-sequence stars whose masses were greater than 1.4 $M_{\odot}$, the Chandrasekhar limit [22], when undergoing gravitational collapse [73]. Neutron degeneracy pressure prevents further collapse resulting in a small $\sim$20 km diameter, incredibly dense

$\sim 10^{15}$ g cm^{-3} compact star with mass $\sim$1.4 $M_{\odot}$ [63]. NS were first proposed as supernova remnants in 1934 by Walter Baade and Fritz Zwicky who stated: *"With all reserve we advance the view that a super-nova represents the transition of an ordinary star into a NS, consisting mainly of neutrons. Such a star may possess a very small radius and an extremely high density"* [10].

During an investigation on scintillation - an effect caused by the irregular structure of ionised gas in the interplanetary medium - of compact radio sources in 1967, Anthony Hewish and Jocelyn Bell Burnell detected an unusual signal that passed overhead each day at the same sidereal time, indicating the source to not be of terrestrial origin. Further investigation revealed the signal consisted of 0.3 s lengths repeating every 1.337 s with incredible accuracy. Three more of these periodic sources were found to exhibit similar behaviours, suggesting a common source. The stability of the signal's oscillations showed regular periodicity with only some very small irregularities over time. Hewish and Bell observed these periodic, pulsating radio waves to be propagating from within our Milky Way galaxy [46]. Their discovery provided the first observational evidence for the existence of the neutron stars that had been predicted by Baade and Zwicky [10].

Pulsars are a type of NS that exhibit fast rotational periods (s to ms),

incredibly strong magnetic fields (10^4 to 10^{11} Tesla), and average densities around $p < 3\pi/GP^2$ where $G = 6.674{\times}10^{-11}$ m^3 kg^{-1} s^{-2} is Newton's gravitational constant [73]. It may be that most NSs share these properties and pulsars are simply the ones from which we detect pulsed emission (e.g. others might also be emitting, but their beams do not sweep past Earth). The first models to constrain the physical properties of NSs were proposed in 1939 by Robert Oppenheimer and George Volkoff [85]. However, after the discovery of pulsars, better models were presented in 1968 by Thomas Gold, which described the lighthouse model of pulsars [41], and Franco Pacini, detailing the pulsar spin down rate.

$$\frac{dE_{\text{rot}}}{dt} = \frac{-4\pi^2 I\dot{P}}{P^3} \tag{1.1}$$

where $\dot{P}$ is the spin period derivative [87]. Both described the misalignment between a pulsar's magnetic dipole from its rotational axis, resulting in narrow beams of accelerated particle emission to sweep out and along their magnetic axes, similar to a lighthouse [87][41]. These emissions can be observed with radio telescopes on Earth as the beams pass across the line-of-sight path between the pulsar and an observer [73]. A pulsar's rapid spin period is a consequence of the conservation of angular momentum during the core collapse of its progenitor star [63]. The magnetic field is also preserved and compressed during the supernova, resulting in a highly magnetized stellar object [73]. Over the last few decades, many theories

have been put forward in an attempt to explain the physics of NS interiors, but the most commonly accepted proposes that a supernovae remnant would consist of both a super fluid and superconducting core, encapsulated within a thin, fragile crust (a crystalline type structure) [62].

A pulsar is an extremely stable, highly accurate, space-based atomic clock due to its high moment of inertia. The narrow beams of emission radiate out and along their magnetic poles, observable in the optical, radio, x-ray, and γ-ray spectra. They are extremely useful, natural laboratories for various areas of astrophysical research. Assuming pulsar rotation exhibits braking due to magnetic dipole radiation - a pulsar's surface magnetic field can be determined from the spin period P and its derivative $\dot{P}$.

$$B_{\mathrm{s}} = 3.2 \times 10^{19} \sqrt{P\dot{P}} \tag{1.2}$$

where P measured in seconds and B_{s} in Gauss [73]. The braking index $n = \ddot{\nu}\nu/\dot{\nu}^2$ depends on the braking mechanism for pulsar spin-down, where measured values span orders of magnitude. Magnetic dipole braking is $n = 3$, and braking due to gravitational radiation (i.e. GW emissions) is $n = 5$ [98]. A pulsar's characteristic age τ can also be derived from P and $\dot{P}$.

$$\tau = \frac{P}{2\dot{P}} \tag{1.3}$$

These values help determine the two distinct pulsar populations; young or "normal" pulsars, and millisecond pulsars (MSPs), the latter of which are believed to be older recycled pulsars spun-up through accretion of material from a companion star in binary systems [73].

In 1975, Russell Hulse and Joseph Taylor discovered the first pulsar in a binary system, PSR B1913+16, providing the first opportunity to calculate accurate pulsar mass measurements, as well as to study the physics of compact stars and binary systems as PSR B1913+16 is a natural laboratory for testing Einstein's theory of GR in a high-speed system with an accurate clock, eccentric orbit and strong gravitational field [55]. The study of this binary system yielded the first evidence for the emission of GWs (see Section §**1.2**), inspiring many techniques used for pulsar timing (see Section §**1.3**) analysis today [73].

The discovery of the first MSP [11] raised challenging questions regarding its origin. After ruling out all other possibilities, PSR B1937+21 is believed to be spun-up through the transfer of energy and momentum from a companion star in a binary system. This companion star is thought to have gained the necessary escape velocity during the transfer. PSR B1937+21 has provided the basis of our understanding behind accretion systems in binary compact star systems - the birthing environment for MSPs. About 2800 pulsars have been recorded to date, mostly all residing within the

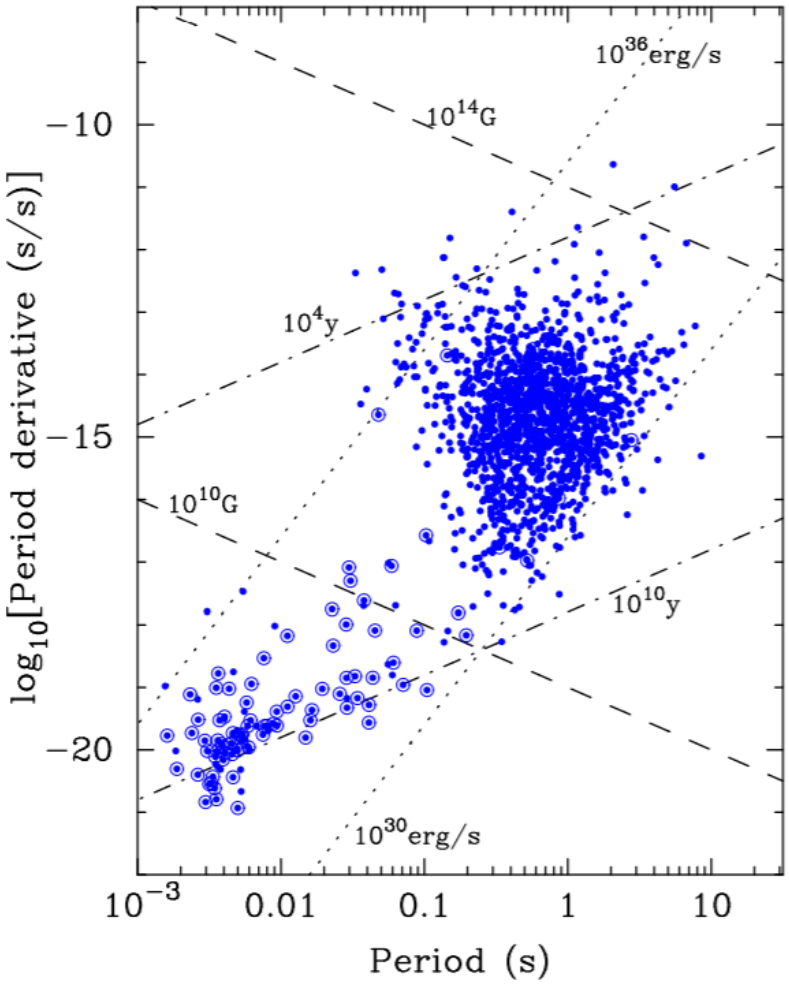

Figure 1.2: **Pulsar $P\dot{P}$ diagram [70] with data from the Australian Telescope National Facility (ATNF) pulsar data catalogue [76]. This plot shows the recorded radio pulsar population as a function of spin period P (seconds) versus the spin derivative $\dot{P}$ (dimensionless) on a log-log scale. The general cluster in the top mid-to-right of the diagram represent the "normal" pulsar population, with MSPs in bottom left cluster. Pulsars in a binary system are distinguished by open circles. Superimposed lines are the characteristic ages lines (dash-dotted), the magnetic field lines (dashed), and the pulsar death line (dotted) estimated by Chen and Ruderman [24].**

Milky Way galaxy [76]. There are two main species of pulsar (see Figure §**1.2**), distinguished by comparing their observed pulse periods: (i) normal, with pulse periods from 0.3 to 30 s, and (ii) recycled, predominantly binary pulsars with pulse period between 1 to 100 ms [73]. MSPs (also known as "recycled" pulsars) have gone through a specific evolutionary path that included mass transfer, and therefore mostly occur in binaries. However, you can find both normal pulsars in binaries, as well as solitary MSPs. Although not constant as rotational kinetic energy is released through relativistic particle winds and the emission of radiation, the stability of pulse periods and the corresponding/correlated predictability over long timescales are consequences of the extremely large pulsar moment of inertia [112]. Many pulsar parameters, including the rate of slowdown $\dot{P}$, can be derived from pulse time of arrival (TOA) measurements made over long time intervals [63]. High-precision timing observations for MSPs, combined with improved instrumental capabilities and accuracy will enable deeper understanding of pulsars e.g. contributing to the understanding the NS equation of state [28], and improve detection sensitivity in the search for low frequency GWs [125].

1.1.3 The Nature of Black Holes

Einstein first predicted the existence of BHs in 1916 while formulating his theory of GR [34]. There a two main species of BHs known to astronomers: (i) stellar mass BHs and (ii) SMBHs. However, GR includes the possibility

that BHs could exist at any mass.

Supernova explosions of stars with mass greater than the Tolman-Oppenheimer-Volkoff limit [121][85] constrain the entirety of the star within an infinitely dense singularity. This "point of no return" is referred to as a stellar mass BH. The singularity is a point with no volume, encapsulated within an event horizon - the region where nothing can escape its gravitational force, not even light [45]. Stellar mass BHs are fascinating stellar artefacts with physical conditions that would be impossible to replicate on Earth.

For a non-rotating stellar mass BH, the event horizon is defined by the Schwarzschild radius R_{S} (named after Karl Schwarzschild who discovered this parameter),

$$R_{\mathrm{S}} = \frac{2GM}{c^2} \tag{1.4}$$

where G is the gravitational constant, M is the star's mass before supernova, and $c = 2.99{\times}10^8$ m s^{-1} is the speed of light [104]. Things are even more complicated for a rotating BH. The only properties determinable are the mass, spin and electric charge [45].

Stellar mass BHs are modelled as Kerr BHs, named after the New Zealand astronomer Roy Kerr who found the first exact solutions to Einstein's field

equations in 1963, describing the physics of rotating BHs. Kerr's solution to the equation of state is a dimensionless spin parameter a of a rotating stellar mass BH.

$$a = \frac{cJ}{GM^2} \tag{1.5}$$

where J is the angular momentum [59]. A non-spinning BH would then have the solution $a/M = 0$ [104], and a spinning one would have $a/M = 1$ for maximum rotation. Kerr BHs are modelled with a ring singularity and some static limit which describes the boundary between the ergosphere - an egg shaped region where space-time at the ergosurface moves at the speed of light (this speed decreases within) - and normal space (see Figure §**1.3**) [59]. Objects within the ergosphere may be ejected from the BH if they gain enough rotational energy here, but once an object passes over the outer sphere of the event horizon, it will be lost forever [104]. Even radiation is unable to escape the gravitational pull inside the event horizon, therefore most stellar mass BHs are observed in binary systems where the accretion of gas can be measured by x-ray and γ-ray, allowing for indirect detection of the system [106]. GWs emitted during stellar mass BH binary inspirals and mergers provide the best method for studying their complex nature [68]. SMBHs are rarer, containing a million to a billion times more mass than stellar mass BHs [80]. These objects reside within the heart of all large galaxies, including our Milky Way (i.e. Sagittarius A* with a mass approximately $4{\times}10^6$ $M_\odot$) [108]. Over 100 have determined masses [100]. SMBHs can also radiate

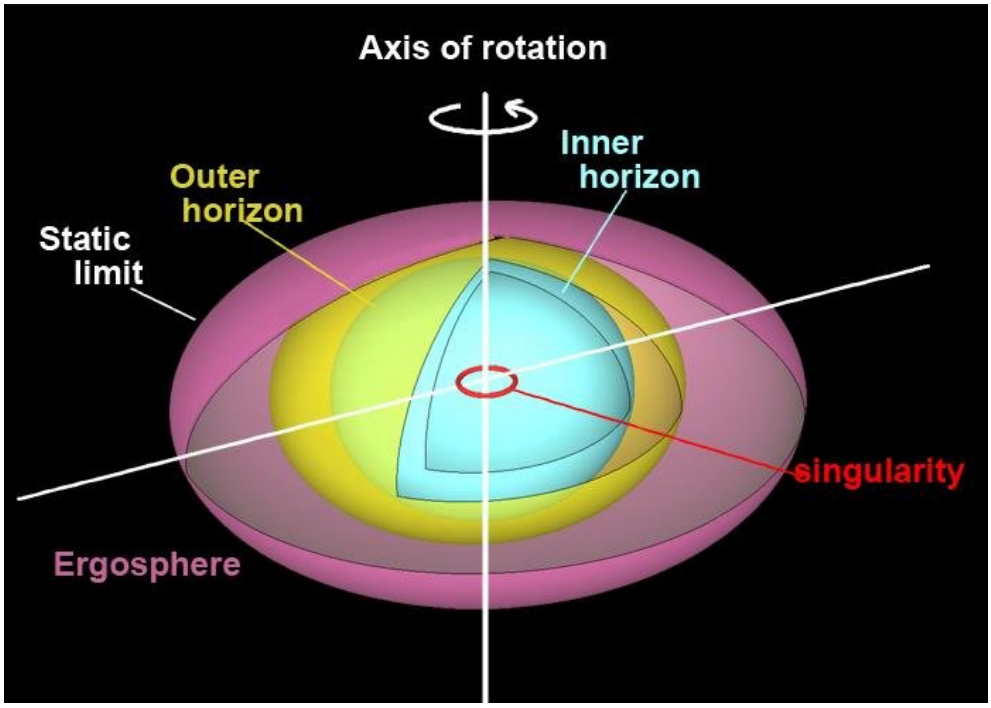

Figure 1.3: **Artistic rendition of a Kerr BH [91] with a ring singularity (red), inner (blue) and outer (yellow) event horizons, encapsulated within the ergosphere (purple), and the static limit, or boundary between the ergosphere and normal space [59].**

energy through the annihilation and creation of particle and anti-particle pairs, providing a calculable measure of temperature T, which was derived by Stephen Hawking in 1964.

$$T = \frac{hc^3}{8\pi\ k_{\mathrm{B}} GM} \tag{1.6}$$

where h is Planck's constant and k_{B} is Boltzmann's constant [45]. It is still uncertain how SMBHs form. These objects may have birthed within the massive gas and dust clouds present in the early stages of the universe [80], or grew from stellar mass BHs over billions of years by consuming enormous amounts of energy from: interstellar gas, dust, stars, and other stellar objects. Alternatively, they may have formed from stellar mass BH binary mergers [108].

The first observational evidence, GW150914 (see Section §**1.2.3**), for the existence of BH binary systems that inspiral and merge within a hubble time was discovered by the Laser Interferometer Gravitational wave Observatory (LIGO) collaboration [6], providing unique information about the nature of BHs and testing our understanding of gravity and galaxy evolution. Until early 2019, no BH was ever directly detected. The first and only image was captured by the Event Horizon Telescope (EHT) of a BH residing in the centre of the neighbouring galaxy M87, located ∼55 Mly from Earth [40]. Before the recent EHT direct detection of a BH, only

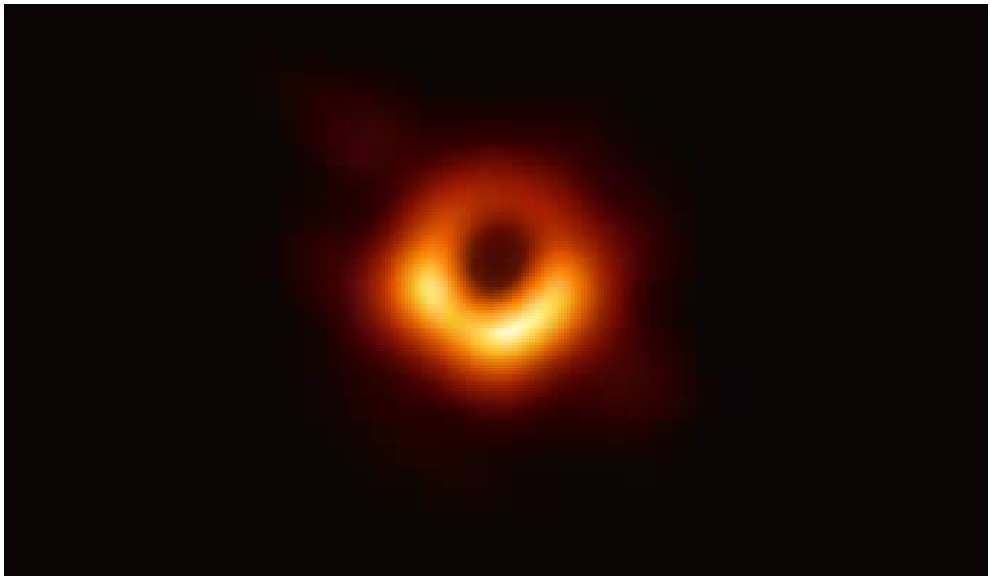

Figure 1.4: **The first direct image of a BH taken by EHT in early 2019 [40].**

indirect evidence existed, mostly gained from observations of high-energy producing quasars in active galactic nuclei [106]. Quasars, quasi-stellar objects, were discovered in 1962 by Martin Schmidt [103]. These are the brightest objects in the Universe next to supernovae and γ-ray bursts. Quasars are believed to be powered by SMBHs and the observable light comes from the accretion disks of materials being pulled into the BH from surrounding stars [40]. Quasars are also observable in the radio spectrum as radio waves are emitted through the quasar's jets [108]. These objects radiate a trillion times more energy than the Sun, thus suggesting that the only mechanism capable of producing such immense energy must be SMBHs converting gravitational energy into light [80].

1.2 Gravitational Waves

The young Issac Newton first discovered gravity whilst deep in thought about the forces of nature, when a lone apple fell from the tree under which he sat, landing on his head and bringing him to a realization that there must be some invisible force acting upon falling objects (or so the story goes). By 1687, Newton had developed the theory of Universal Gravity to describe the physical attraction between two bodies, equivalent to the product of their respective masses divided by the square of distance between them; i.e.

$$F = G\frac{m_1 m_2}{r^2} \tag{1.7}$$

where F is the gravitational force acting on two objects, m_1 and m_2 the objects masses, and r is the distance between them [82]. This fundamental theorem was later improved upon by Albert Einstein, who realised that gravity and acceleration are synonymous, leading to his 1916 theory of GR. GR differs from Newton's Universal Gravity theory by incorporating gravity into the space-time metric, resulting in the curvature of both space and time in the presence of some mass [34]. For example, in scenarios where more mass is confined within a limited volume of space (i.e. a compact star), more space-time fabric curvature is expected within and around the region [45]. In extreme cases such as the merger of compact stars, the accelerating objects swirl inwards towards coalescence, causing convulsions throughout the curvature which results in "ripples" - the

propagation of GWs [6]. These ripples cause fluctuations in the observable distance between a source emitting GWs and an observer. These fluctuations are the stretching and contracting fabric of space-time [79]. GWs are the fundamental ramification of GR, where space and time are married in such as way that GWs are predicted to generate within supernovae and coalescing compact star binaries [80].

1.2.1 The Nature of Gravitational Waves

GWs propagate outward from large disturbances in the fabric of space-time usually caused by phenomena that accelerate masses far off from Earth, in the distant cosmos. The propagating waves decrease in amplitude as they travel through space, making them very weak and difficult to detect by the time they reach Earth [68].

Only a small number of GW emitting sources have been detected to date. Most notably is the binary pulsar-NS system discovered by Hulse and Taylor in 1974. Their Noble Prize winning discovery involved novel techniques for timing the pulsars where they discovered a systematic variation in the timing, indicating a binary system [55]. Further observations of the pulsar PSR B1913+16, by Taylor and his colleague Joel Weisberg in 1981, revealed an orbital period rate of change and loss of energy within the system [130]. This discovery was the first indirect evidence of GWs, supporting the claims of GR, that orbital properties of

coalescing binaries change as energy of the system is carried away in the form of gravitational radiation [34]. Even with binary systems providing verification of the existence of GWs, there was a need for incredibly sensitive instruments to assist in their detection as direct detections remained elusive.

GWs are now confirmed to be small deformities of the four-dimensional space-time metric that propagate away from the most extreme catastrophic events in the Universe (i.e. supernovae or the inspiral, coalescence and ring-down periods of compact star binary mergers) [66]. The power dE/dt emitted from a coalescing compact star binary system is:

$$\frac{dE}{dt} = -\frac{32G^4}{5c^5r^5}(m_1m_2)^2(m_1+m_2) \tag{1.8}$$

The rate of decreased distance dr/dt between two masses, is given by:

$$\frac{dr}{dt} = -\frac{64G^3}{5c^5r^5}m_1m_2(m_1+m_2) \tag{1.9}$$

and thus the orbital frequency $d\omega/dt$ increases at a rate of

$$\frac{d\omega}{dt} = -\frac{3\omega}{2r}\frac{dr}{dt} = \frac{96}{5}\frac{G^{\frac{5}{2}}m_1m_2(m_1+m_2)^{\frac{3}{2}}}{c^5r^{\frac{11}{2}}} \tag{1.10}$$

indicating the emission of GWs during a binary pair's inspiral [25]. This derivation was verified by observations of PSR B1913+16, showing the

pulsar-NS binary system's orbital period to decrease by 2.4×10^{-12} s s^{-1} [130]. In the final seconds before a binary undergoes coalescence, the orbital period will become as small as a few milliseconds, and the majority of the system's orbital energy gets released in the form of GWs [80].

In September 2015, after many decades of planning, testing and improving the instrumentation, a new era of GW astronomy began with the first direct detection of high frequency GW emissions from two stellar mass BHs coalescing by LIGO [6]. With this discovery, gravity was elevated to "important messenger" status, providing useful information from the distant Universe [80]. Since then, direct detections have continued, informing astronomers that Einstein's theory of GR was correct, paving the way for new opportunities to study both GWs and the Universe itself in more depth than ever before [68]

Detection of phenomena in different bands of the EM spectrum (i.e. visible, radio, x-ray, γ-ray, and ultra violet light), provides detailed understanding of the Universe. Direct detection of GWs, has however, extended the limits of our understanding of the universe [5]. Unfortunately, most bands of the EM spectrum are somewhat unusable due to the refraction and/or reflection of a signal as it travels between the source and an observer [112]. GWs are not effected by intervening matter and therefore provide clear and precise details of the sources generating them [80]. With the direct

detection of GWs, previously unexplored territories are becoming available for investigation, as they provide insights into the complex nature of the most catastrophic events to occur within the farthest reaches of the cosmos [77]. These investigations include: the formation of BHs [129], testing the constraints of GR [132][120], searching for a stochastic GWB [9][8], and understanding the physics of NS interiors [112].

GWs cannot yet be detected directly at visible or radio frequencies. Large ground-based laser interferometers are currently the most sensitive observatories to GWs, allowing direct detections of binary compact star system mergers and possibly even unfamiliar sources that are yet to be discovered [4]. However, future plans include a Pulsar Timing Array (PTA) that could provide the best means for detection in the radio regime [77][79]. GW observations with PTAs will be able to detect low frequency (nHz) GWs from SMBH binary systems and higher frequency (kHz) GWs from compact stellar objects. Therefore PTAs are the crucial next step for gaining greater understanding of the physics and inner workings of compact stellar objects [48]. GW astronomy may also provide insights into areas of cosmology as a possible window for observing the early Universe [80].

1.2.2 Gravitational Wave Detectors

Detecting GWs is equivalent to measuring a motion 10,000 times smaller than an atomic nucleus [66]. This is because the amplitude decreases $(1/r)$

with distance away from the source, so even the most catastrophic of events may only yield signals that fade to minuscule amplitudes by the time they reach Earth, if not sooner [68]. Due to the extremely low frequency of GWs, they are incredibly difficult to detect and even detection by a single detector would not provide any means for distinguishing the source's location [4]. Therefore multiple detectors must be implemented to discern the signal's direction, as a few milliseconds of difference in arrival times is enough to estimate the direction with satisfactory precision [68].

The first method for direct GW detection was proposed in 1960 by Joseph Weber, the Weber bar - a large, solid, suspended aluminium bar replicating a giant tuning fork [129]. This idea was later discredited, but may have inspired further research towards GW detection and attempts at proving/disproving GR. With the advancement of technology, large ground-based interferometers were designed. Interferometers detect, collect and study the wealth of astrophysical data gathered in the form of GWs [77]. These instruments are two long identical tunnels at 90° of separation (see Figure §**1.4**). As a GW passes through the Earth, the laser beams transmitting down each tunnel will detect the compression or stretching of space, resulting in a light pattern formed in the recombined beam at the detector [68].

Ground-based Interferometers

The first ground-based interferometer was built in 1999, initial LIGO (iLIGO), comprising of two identical observatories positioned 3000 km apart in: (i) Livingston, Louisiana and (ii) Hanford, Washington of the United States of America [6]. Both observatories have two 4 km long, 1 m wide vacuum chamber tunnels (see Figure §**1.5**) [68]. iLIGO was operational between 2002 and 2010, with assistance from smaller interferometers: Virgo (Italy), TAMA300 (Japan), and GEO600 (Germany) [74]. However, no GWs were detected [4], requiring higher sensitivity and further knowledge to distinguish between a real signal and unwanted instrumental or local environment interference (i.e. seismic/thermal noise, electrical disturbances, and structural expansion/contractions) [68].

The iLIGO operational run provided many insights that were used to improve and refine the model. Redesign provided 10 times greater sensitivity [4]. iLIGO was renamed to advanced LIGO (aLIGO) for its first observational run from September 2015 to January 2016. During this period, aLIGO (with assistance from Virgo) detected three separate stellar mass BH binary mergers: GW150914 (see Figure §**1.5**) [6], GW151012 [1], and GW151226 [2]. Multiple detectors allow for triangulating the source's direction by measuring the arrival time differences between detectors [4].

Even with the sensitivity of ground-based interferometers, the noise from

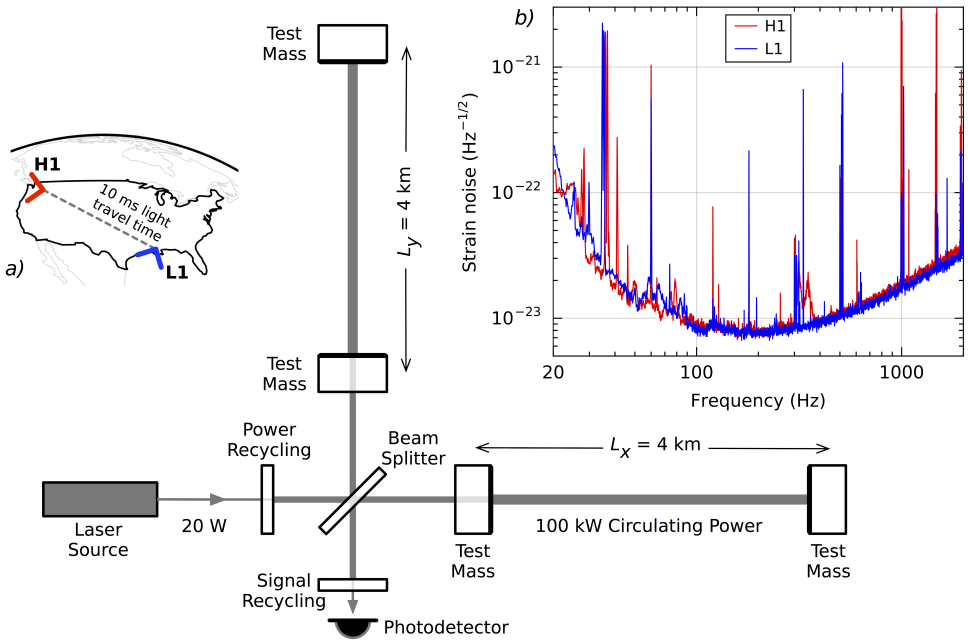

Figure 1.5: **Diagram of the LIGO detector with a) location and orientation of detectors, and b) instrumental strain noise variation over frequency in the detectors [6].**

seismic activity and other environmental disturbances impact the ability to detect GWs [4]. However, these limitations can be overcome with space-based interferometers [77].

Space-based Interferometers

In December 2015, the National Aeronautics and Space Administration (NASA) and the European Space Agency (ESA) launched the first space-based GW detector, the Laser Interferometer Space Antenna (LISA Pathfinder) [74]. This pathfinder mission has been successful,

demonstrating better sensitivity than expected, so its successor, evolved LISA (eLISA) will be set to launch by 2030. eLISA consists of three spacecraft configured in an equilateral triangle with 2.5 Mkm long laser arms emitting between each satellite. eLISA trails the Earth in a heliocentric orbit [20]. Complementing ground-based detectors (i.e. aLIGO and Virgo) which operate in the Hz to kHz bands, eLISA will monitor GWs over μHz to 1-Hz frequencies [74]. To put this into perspective, where aLIGO has detected the final moments of a binary system's merger (followed by some ring-down), the higher sensitivity of eLISA will allow for observations of different types of sources, as well as, mergers occurring a number of years prior ground-based detections [20].

A collaboration of ground- and space-based GW data will allow researchers to make better predictions of mergers and merger rates throughout the cosmos [48]. Not only do these measurements provide tests for GR [66], but sources with precise sky localisation can be used as standard candles - a baseline - to measure the rate of cosmic expansion to high redshift [112]. Other areas of possible research include: studying the formation and evolution of compact binary systems within our Milky Way [102], mapping the geometry of SMBHs [68][79][106], performing dark matter tests [45][74], searching for exoplanets [14], and searching for a GWB that could be carrying information about the primordial universe [9][25][66][80][105].

Pulsar Timing Arrays

Pulsars are the most precise clocks in the Universe due to their extreme rotational regularity, especially MSPs which have a nearly constant spin period [48]. Therefore, a known, well-timed population of MSPs may enable the detection of nHz GWs (inaccessible to LIGO/LISA) as the wave's path would induce small variations in pulse frequency [105]. PTAs are therefore the next ambitious target in GW research, complementing both ground and space-based observatories [66]. High-precision timing of PTAs is expected

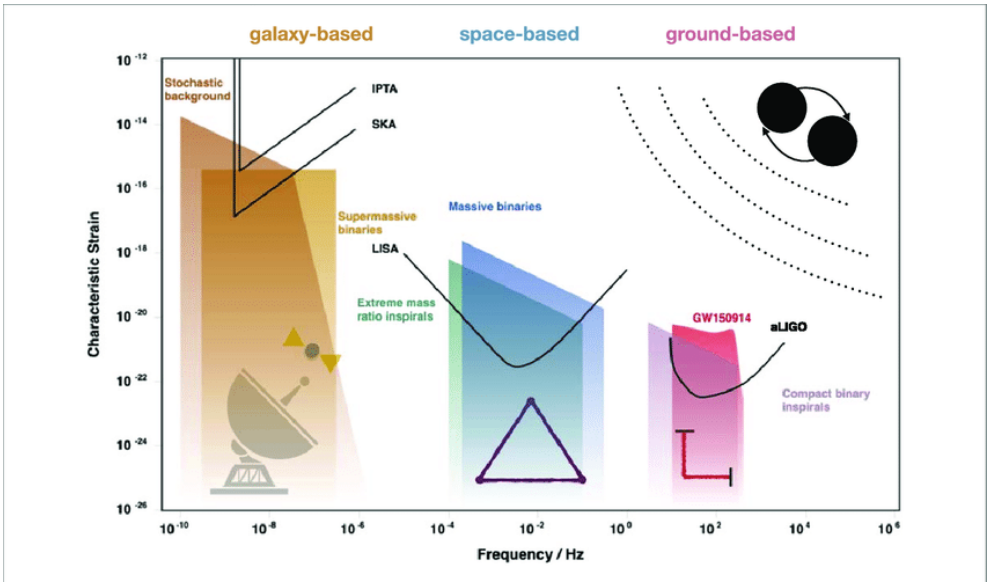

Figure 1.6: **Diagram of the characteristic strain sensitivity for GW detectors as a function of frequency. Predicted GW signals from astrophysical phenomenon are shown [80].**

to provide the detection of GWs from a population of SMBH binaries with masses ranging from 10^7 to 10^{10} $M_\odot$ [37]. PTAs will operate over the

frequency regime from several to 100-nHz, so deviations in TOAs due to GWs are of the order of tens of nanoseconds. The periods of the GWs are of the order of years to decades [105]. By modelling the spectrum of the stochastic GWB (see Figure §**1.6**), theorists predict that they will be able to learn more about the history of SMBH binary mergers over cosmological timescales. LISA and LIGO will never be sensitive to such low-frequency waves; e.g. billion solar mass BH binaries never emit waves in the LIGO/LISA bands (million solar mass BH binaries are predicted to be detectable by LISA) [80]. In an effort to achieve this goal, many collaborations have formed: the European Pulsar Timing Array (EPTA) [66], Parkes Pulsar Timing Array (PPTA) [77], and the North American Nanohertz Observatory for Gravitational Waves (NANOgrav) [8], members of which are also now working together towards an International Pulsar Timing Array (IPTA) collaboration [48].

1.2.3 Gravitational Wave Detections

The first direct detection of a GW was made by aLIGO on the 14th of September 2015 (GW150914). This GW was generated by the inspiral and merger of two stellar mass BHs (36 and 29 $M_\odot$), approximately 1.3 billion light years from Earth, merging into a single 62 $M_\odot$ BH. During the event, 3 $M_\odot$ radiated away in the form of GWs [6]. A second and third merger event (GW151226 and GW151012) were also detected during aLIGO's first observation run, also from stellar mass BH binaries merging [4]. During

aLIGO's second observational run, a further three stellar mass BH binaries mergers were detected (GW170104, GW170814, and GW170608), as well as the first direct detection of GWs produced from a NS binary system coalescing (GW170817) [3].

Each new measurement provides a unique view of the physical properties of GW sources, including their: mass, rotation speed, and orbital diameter - all factors that affect the shape and strength of the detected GW. These properties are determined from the moment to moment changes in the signal observed during the inspiral, merger and ring-down of binary systems [4]. The distance to a source is derived from the luminosity distance of the GW, typically measured in the megaparsec scale (i.e. million of light years from Earth) [80]. Future detections and the amalgamation of ground and space-based data with PTA measurements will be needed to advance this fascinating area of astrophysics [105].

1.3 Pulsar Timing

Pulsars are monitored approximately monthly for a year or more to determine properties such as spin period, distance, mass, etc. They are observable in the optical, radio, x-ray and γ-ray frequencies of the EM spectrum as they emit narrow beams of EM radiation out and along their magnetic poles [26]. As the star rotates, these beams are detectable if they

sweep along the line-of-sight of an observer [73].

Pulsars have been used for a number of applications and research, including but not limited to: the search for nHz GWs [52][66][77][105], testing GR with relativistic binary systems [112][120], exoplanet discovery [14], measuring the electron density distribution within the Interstellar Medium (ISM) through use of the Dispersion Measure (DM) [74], refining the equation of state for dense matter [105][121], and studying the highly magnetized plasma of the magnetosphere and physics of pulsar interiors [62][63]. All of these applications rely heavily on the high precision and accuracy of pulsar timing [80]. The basic concept of pulsar timing (see

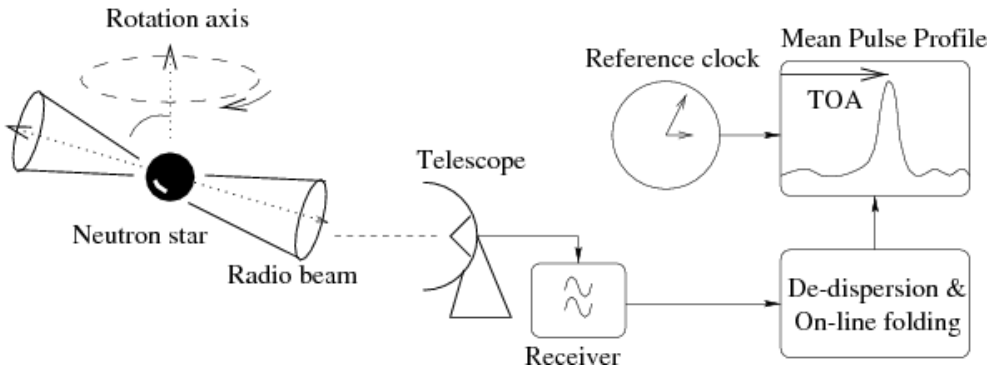

Figure 1.7: **The fundamental process for pulsar observations. Pulses recorded by a radio telescope are dedispersed and added to form a mean pulse profile [70].**

Figure §**1.7**) involves measuring TOAs and disentangling the many phenomena that affect them, primarily: orbital motion and dispersion effects within the ISM [125]. An MSP's average TOAs can be measured to

considerable precision, better than 1 μs [97]. Pulsar signals are given a time-stamp based on the local time of an observatory's clock; they are then dedispersed to reverse the effects of propagation through the ISM, and finally added together to form a stable mean pulse profile [30]. The mean pulse profile for most MSPs is stable at any given frequency and is typically cross-correlated with a template profile of high signal-to-noise, obtained over many observations at a given frequency [112]. This correlation yields a time offset that can then be added to a reference point on the profile, creating the required high-precision TOA measurement [125]. For high-precision TOAs, observations require large, highly sensitive instruments [112]. To model long-term variations also requires a series of TOA measurements that span timescales from years to decades [123]. Precision here is referring to beating down the noise (with large bandwidth, cyrogencially-cooled receiver, high gain antenna, etc.), but high-precision pulsar timing also requires accuracy. Accuracy is about beating down the systematic errors (polarization calibration, clock synchronization, accurate location of telescope, accurate modelling of Earth's location with respect to the solar system barycentre, etc.) [123].

Pulsar timing solutions for newly discovered binary systems can take many months to over a year to disentangle the binary system parameters from astrometric parameters. The basic progression of physical parameters that can be derived are: (i) upon discovery, there is an estimate of spin period

and DM; it may also be possible to determine the rotation measure in a single full-polarization follow-up observation, (ii) depending on the orbital period, it may be possible to determine some of the Keplerian orbital parameters within days (for highly relativistic systems with binary periods of the order of hours) or weeks (for MSPs with WD companions and binary periods of the order of days), (iii) it takes about half a year to separate the spin period derivative from the astrometric parameters (right ascension and declination), and (iv) it takes more than a year to get precise astrometric parameters and start measuring things like parallax (requires high precision), and proper motion (requires high precision or very long time spans). If the observed pulsar is in a binary system, the timing solution will also include five Keplerian orbital parameters: orbital period, projected semi-major axis, eccentricity, time of periastron passage, and the argument of periastron [97]. For better precision, pulsar timing considers each rotation over very long timescales. However, the spin period is not constant as rotational kinetic energy gets released primarily as magnetic dipole radiation and through relativistic particle winds [38]. Pulsar astronomers have derived NS masses and companion masses, placed limitations on the equation of state of nuclear matter, and performed tests of GR using pulsar timing without any need for GW detection [71].

1.3.1 Timing Conversions and Delay Corrections

Cross-correlation techniques are used to compare the average pulse profile to the template profile in the frequency domain. This yields an estimated phase shift ϕ for the observation, which is an added offset to the time of a fiducial point in the pulse profile observations, providing the required TOA measurement [123]. The initial component of the timing model is then defined by a Taylor expansion of the pulsar's rotational phase ϕ over time t.

$$\phi = \phi(t_0) + \nu(t - t_0) + \frac{1}{2}\dot{\nu}(t - t_0)^2 + ... \tag{1.11}$$

where $\nu = d\phi/dt$ is the rotation frequency, $\dot{\nu}$ representing its time derivative, and t_0 is a chosen reference epoch [12]. This description relies on observations taken from an inertial reference frame, but due to the Earth's rotation and its orbit around the Sun, ground-based observatories are not inertial reference frames. Therefore, TOAs require a number of timing conversions and delay corrections to both convert time to an inertial reference frame, and to undo any relativistic and dispersion delays [76]. In order to effectively remove these rotational and orbital motions of the Earth, each measured TOA must be converted to the solar system's barycentre, providing the best approximation of an inertial reference frame [51]. For example, by modelling and correcting for such uncertainties in planetary orbits (mostly Jupiter), NANOGrav have improved the solar system ephemeris by narrowing down the barycentre to within 100 m [122].

A number of delay corrections must also be applied to improve the initial timing model, namely; Einstein delay $\Delta_{E_\odot}$ from relativistic reference frame transformations, Roemer delay $\Delta_{R_\odot}$ from the observatory's motions, Shapiro delay $\Delta_{S_\odot}$ from the presence of bodies in the solar system and their gravitational potential, and the frequency dependant ISM dispersion delay Δ_{DM} [120]. The transformation between a telescope's measured pulse observation time t_{OBS} and proper pulsar emission time t_{PSR} in an approximately inertial reference frame - typically the solar system's barycentre - is modelled by:

$$t_{PSR} = t_{OBS} + \Delta_{CLOCK} - \Delta_{DM} + \Delta_{E_\odot} + \Delta_{R_\odot} + \Delta_{S_\odot} + \Delta_{BINARY} \qquad (1.12)$$

where Δ_{CLOCK} is the correction accounting for differences between the observatory and the solar system's barycentric time standard (regularly updated), and Δ_{BINARY} accounts for additional delays if the pulsar is in a binary system [33].

Dispersion Delay

Dispersion delay Δ_{DM} occurs when radio waves propagate through the ionized gas within the ISM, which causes a timing delay in the EM wave [73]. This delay (see Figure §**1.8**) is a function of radio frequency and the density of charged particles in the ISM along the line-of-sight between the

source and an observer [70]. Dispersion delay can be estimated using

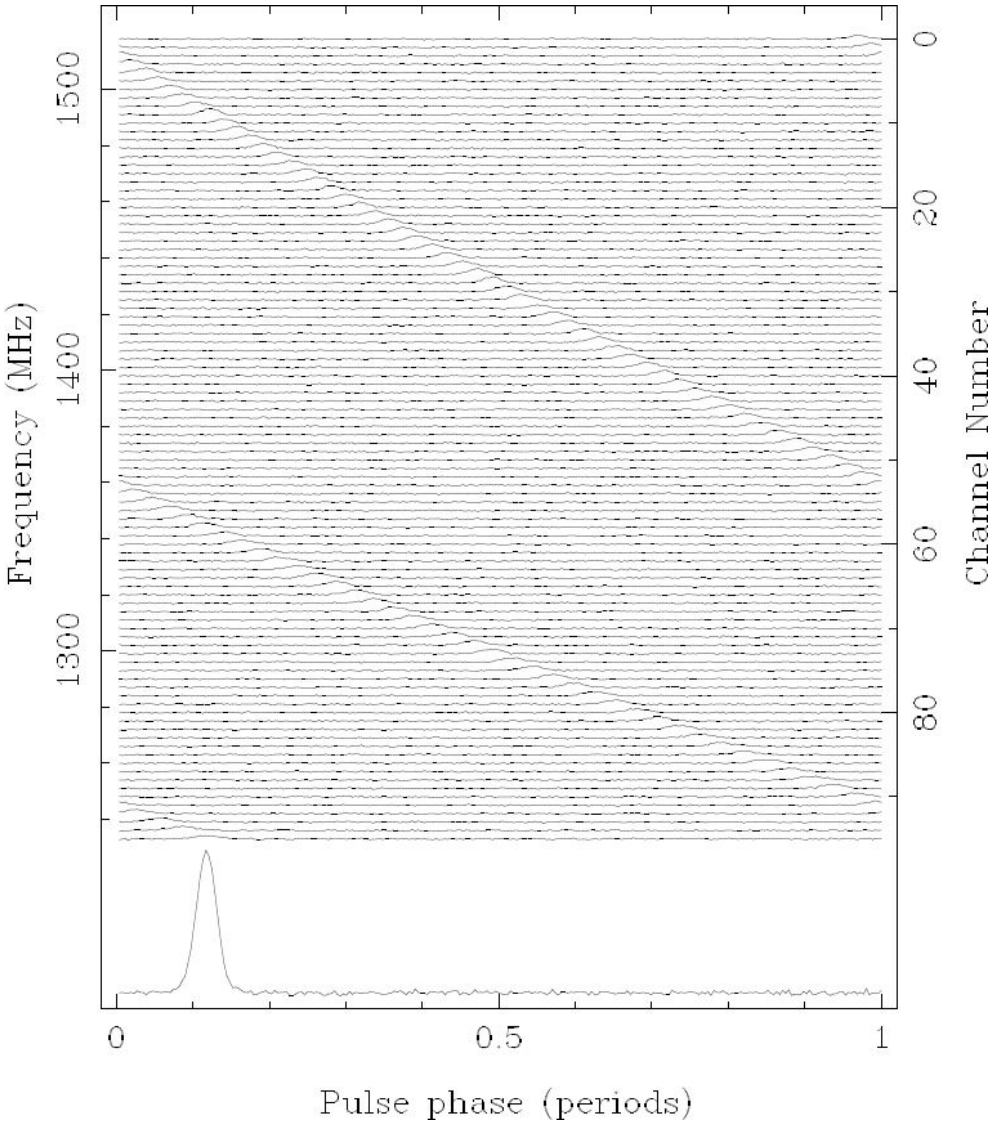

Figure 1.8: **Pulse dispersion delay measurement of the 128 millisecond pulsar B1356-60 with DM of 295 cm^{-3} pc^{-1}. The integrated pulse profile is shown across the bottom of the plot [73].**

observations at different frequencies, where the inherent properties of the

pulsar can be modelled [112]. The delay between two signals at different frequencies is modelled as:

$$\Delta_{\mathrm{DM}} = 4.15 \text{ ms} \times \left[\left(\frac{\nu_1}{\mathrm{GHz}} \right)^{-2} - \left(\frac{\nu_2}{\mathrm{GHz}} \right)^{-2} \right] \times \left(\frac{\mathrm{DM}}{\mathrm{cm}^{-3}\mathrm{pc}} \right) \tag{1.13}$$

between frequencies ν_1 and ν_2.

DM is defined as the column density of free electrons in the ISM along the line-of-sight as:

$$\mathrm{DM} = \int_0^d n_e dl \tag{1.14}$$

where n_e is the free electron density (in electrons per cm^{-3}), and d the distance (in parsecs) to the pulsar [118]. Then the pulsar distance may be derived using a model of galactic free electron distribution. The DM must also be calculated at different epochs as the ISM is not stationary [119]. Ultimately, DMs limit timing precision, so these perturbations must be corrected to improve the TOA model fit accuracy [70].

Einstein Delay

The transformation of the reference frame from an observer's point of view to that of an observer at the solar system's barycentre is fairly straightforward in regards to correcting for the difference in time. However, these two points of reference are affected differently by relativistic time dilation from the rotating Earth, as well as gravitational redshift caused by the presence of the Sun and planets. Gravitational redshift may also arise from a companion star if the

pulsar is in a binary system[33]. Einstein delay $\Delta_{E_\odot}$ accounts for and corrects the time dilation of the solar system[112].

Roemer Delay

Roemer delay $\Delta_{\mathrm{R}_\odot}$ accounts for the extra time that the pulsar signal takes to reach the Solar system's barycentre after being detected by an observer[70]. This measurement requires prior knowledge of: (i) the observatory's position with respect to the Earth's centre, (ii) the Earth's position from the barycentre, and (iii) the position of the pulsar, in order to effectively model and remove this effect [48].

Shapiro Delay

Shapiro delay $\Delta_{\mathrm{S}_\odot}$ accounts for the variation in the speed of pulsar signal as it propagates through the curvature of space-time caused by the presence of some body of mass within the solar system - mostly the Sun and major planets (see Figure §**1.9**). The total Shapiro delay from all masses is the sum of all individual delays Δ_{S_i}.

$$\Delta_{\mathrm{S}_\odot} = \sum_i \Delta_{\mathrm{S}_i} \tag{1.15}$$

where

$$\Delta_{\mathrm{S}_i} = \frac{GM_i}{c^3} \ln[R(1+\cos\theta)] \tag{1.16}$$

Here M_i is the mass of the i'th object, R the magnitude of the vector between observatory and the object, and θ the pulsar-observatory mass angle[48]. Calculated $\Delta_{E_\odot}$, $\Delta_{R_\odot}$, and $\Delta_{S_\odot}$ can be seen in the form of signatures in timing residual plots as phase differences between observed and predicted TOAs [112].

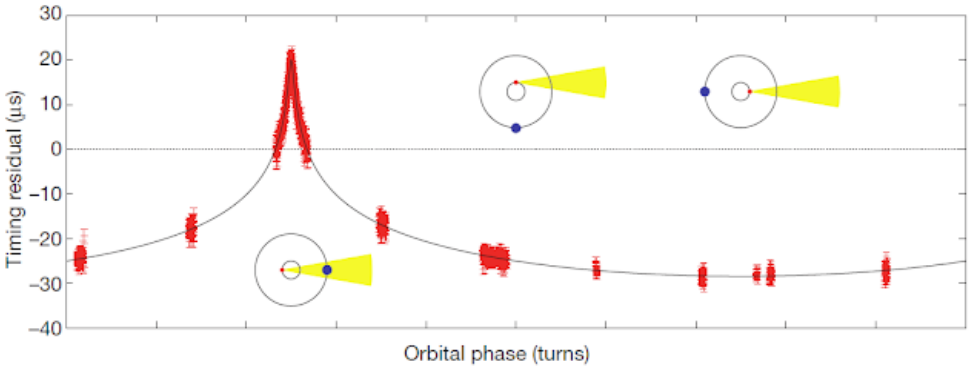

Figure 1.9: **Shapiro delay measurement from a pulsar binary system where a pulsar (red), emits the EM radio beam (yellow), past a binary companion (blue) when propagating along a path towards the Earth. The sharp peak in pulse delay occurs when the line-of-sight passes closest to the companion star of the binary pair [30].**

Binary Delay

The binary delay Δ_{BINARY}, represents each of the Roemer, Einstein, and Shapiro delays in regards to the orbital effects of a pulsar in a binary system. Binary system orbital parameters are described by five of the Keplerian parameters: orbital period decay P_b, orbital eccentricity e, relativistic time dilation T_0, longitude of periastron ω, and the projected

semi-major axis x.

Modern relativistic pulsar timing models include post-Keplerian (PK) parameters (time derivatives of Keplerian parameters) to effectively model the binaries orbital phase, defined by an eccentric anomaly u, true anomaly $A_e(u)$, and longitude ω:

$$u - e\sin(u) = 2\pi\left[\left(\frac{t_{\rm PSR} - T_0}{P_b}\right) - \frac{\dot{P}_b}{2}\left(\frac{t_{\rm PSR} - T_0}{P_b}\right)^2\right] \tag{1.17}$$

$$A_e(u) = 2\tan^{-1}\left[\left(\frac{1+e}{1-e}\right)^{1/2}\tan\frac{u}{2}\right] \tag{1.18}$$

$$\omega = \omega_0 + \left(\frac{P_b\dot{\omega}}{2\pi}\right)A_e(u) \tag{1.19}$$

where ω_0 is the reference value of ω at time T_0. The $\Delta_{\rm BINARY}$ terms are then measured as follows:

$$\Delta_{\rm E} = \gamma\sin(u) \tag{1.20}$$

$$\Delta_{\rm R} = x\sin(\omega)[\cos(u) - e(1+\delta_r)] + x[1 - e^2(1+\delta_\Delta)^2]^{1/2} \tag{1.21}$$

$$\Delta_S = -2r\log\{1 - e\cos(u) - s[\sin(u)(\cos(u) - e) + (1-e)^2\cos(\omega)\sin(u)]\} \tag{1.22}$$

where γ represents the combined time dilation and gravitational redshift due to a pulsar's orbit, $s = sin(i)$ (where i is the inclination angle) is the shape and r the range of the Shapiro delay [112]. The inherent properties of

a binary pulsar are modelled with respect to the solar system's barycentre, and with all appropriate orbital delays corrected for. Timing residuals are produced for each TOA, describing the difference between observed and predicted TOAs [97].

Pulsar timing residuals can be corrected for by applying the least squares algorithm to minimize the model goodness-of-fit,

$$\chi^2 = \sum_{i=1}^{N} \left(\frac{R_i}{\sigma_i} \right)^2 \tag{1.23}$$

where σ_i is the standard deviation, R_i the timing residual of the i^{th} TOA in proper time, where N_i is the nearest integer turn [48].

$$R_i = \frac{\phi_i - N_i}{\nu} \tag{1.24}$$

With sufficient signal-to-noise, timing residuals are expected to exhibit white Gaussian noise if the model parameters perfectly describe the data [123]. Investigations of time and frequency variations provide the basis of all pulsar timing, where variations could indicate errors within the model or the observing instrument. The TOA estimates are then used to update the pulsar timing model parameters [120]. The Root Mean Squared error (RMSE) statistic characterizes the residuals, which include both noise and systematic errors. The best RMSE values are typically below 100ns over

time scales of 5 or more years [97].

1.4 General Relativity

The Universal Gravity theory postulates that mass takes either one of two forms: (i) gravitational mass m_g or (ii) inertial mass m_i, where motion of free falling objects in the gravitational field of a spherical body of mass M takes the form:

$$\frac{d^2\vec{r}}{dt^2} = -\frac{m_g}{m_i}\frac{M}{r^3}\vec{r} \tag{1.25}$$

where r is the radius and $\vec{r}$ the position vector from position a to position b [82]. Galileo investigated the motion of free falling objects to find them identical regardless of mass or structure, (i.e. $m_g \propto m_i$ being proportional for all bodies), implying free fall universality at 9.81 m s^{-2} near the Earth's surface [39][81].

In GR, Einstein assumed Galileo's observation to be universally valid - a fundamental principle - for all physical processes. He called this the "principle of equivalence" sometimes referred to as the "uniqueness of free fall principle", which states that m_g and m_i masses are the same (i.e. acceleration and gravity are synonymous). The equivalence principle is now the foundation of GR, where the difference between Newton's and Einstein's view are considered as the "weak" and "strong" equivalence principles respectively [34]. The weak equivalence principle holds equality

of gravitational and inertial masses if restricted to Newton's laws of free falling bodies in a non-accelerated reference frame, whilst Einstein's equivalence principle includes the Lorentz and positional invariance factors, and applies to all laws of nature which must obey this principle. Because other gravitational theories may come along and disprove either some parts or all of GR, a structured set of protocols have been set up to determine possible violations [112].

The process of testing a theory involves formulating a predicted hypothesis to match against experimental data, where a single contradiction could discredit the idea. Unfortunately, methods used to test theories do not shed light on information like which features are determining success or failure in a given experiment. In 1922, Sir Arthur Eddington created the Parametrized Post-Newtonian (PPN) method for the purpose of testing GR, by invoking Einstein's non-linear gravity equations as lowest-order deviations from Newton's Universal Gravity, allowing some approximations to be determined when studying gravity in weak-field conditions. PPN parametrized the GR space-time curvature γ^{PPN} produced in the presence of mass, and non-linearity in superposition β^{PPN} of the law of Universal Gravity [32] as:

$$\beta^{\mathrm{PPN}} = \gamma^{\mathrm{PPN}} = 1 \tag{1.26}$$

This was later updated by Kenneth Nordtvedt Jr. (1969) and Clifford Will (1971) to include eight extra parameters describing other violations of symmetry in GR, including; Lorentz invariance (ξ), preferred inertial frame effects ($\alpha_1, \alpha_2, \alpha_3$) and the conservation of energy and momentum of a system ($\zeta_1, \zeta_2, \zeta_3, \zeta_4$), so that:

$$\xi = \alpha_1 = \alpha_2 = \alpha_3 = \zeta_1 = \zeta_2 = \zeta_3 = \zeta_4 = 0 \tag{1.27}$$

with higher order terms added for increased accuracy [83][132]. However, the additional eight-dimensional PPN parameter space overly constrain tests of GR in solar system experiments due to the extremely weak gravitational fields under these conditions. The time delay β^{PPN}, observed from light deflection effects of the Sun (discovered by testing GR with observations from the Cassini space probe [14]) and perihelion precession deviations γ^{PPN} (exhibited by Mercury) were compared to those predicted by Newtonian physics [34] as:

$$|\beta^{\text{PPN}} - 1| \leq 6 \times 10^{-4} \tag{1.28}$$

$$|\gamma^{\text{PPN}} - 1| \leq 2 \times 10^{-3} \tag{1.29}$$

1.4.1 Testing GR with NS-NS Binary Systems

Pulsars are also excellent natural space-based laboratories that can be utilized for testing Einstein's theory of GR and other feasible theories of gravitation [126]. Pulsar timing provides a means to track the rotational

phase of pulsars to high precision and make incredibly accurate astrometric measurements which assist in testing gravitational theories in the strong-field regime. GR tests via pulsar timing can be classified into weak- and strong-field equivalence principles, or by verifying that PK parameters match GR predictions over alternative theories [112]. Timing analysis of pulsar signals provides a means for measuring five Keplerian, and a number of PK orbital parameters. The PK parameters are relativistic corrections to the orbital description of a binary NS system [61]. If two PK parameters are measured, relevant parameters of a binary system can be derived, whereas three or more PK parameters provide new tests of GR [113].

PSR B1913+16

The 1974 discovery of the first double NS system PSR B1913+16 by Hulse and Taylor, one of which is a pulsar, revealed a decrease in the orbital period at a rate consistent with the GR prediction of energy loss as GW. This discovery provided strong indirect evidence that supported Einstein's prediction [55]. PSR B1913+16 is in a highly eccentric 7.75 hr orbit with another NS at 3.3l s separation and with velocities $\sim$400 km s^{-1}, providing the perfect system and parameters to test GR in the strong-field regime [112]. For this system, the advance of periastron $\dot{\omega}$, gravitational redshift γ, and orbital period derivative $\dot{P}_b$ are well measured and are in agreement with predictions from GR (see Table §**1.1**). The main thing to note here is that $\dot{P}_b$ confirms the loss of energy within this system in the form of GWs

[130].

Parameter	Value
Orbital period, P_b	0.322997462727 (days)
Projected semi-major axis, x	2.341774 (sec)
Eccentricity, e	0.6171338
Longitude of periastron, ω	226.57518 (deg)
Epoch of periastron, T_0	46443.99588317 (MJD)
PK Parameter	Value
Advance of periastron, $\dot{\omega}$	4.226607 (deg/yr)
Gravitational redshift, γ	4.294 (ms)
Orbital period derivative, $\dot{P}_b$ (10^{-12})	-2.4211

Table 1.1: PSR B1913+16 Paramters

PSR B1534+12

A similar test was repeated in 1997 for the much closer and brighter double NS system PSR B1534+12, which has a wider, less eccentric and longer 10.1 hr orbit. The narrow peak pulse profile observed here enables timing measurements to higher precision than PSR B1913+16. The edge-on orientation of PSR B1534+12 provided three PK parameters (see Table §**1.2**) and also the additional measurements of the Shapiro delay parameters: range r and shape s, providing a different test of GR [113].

PSR J0737-3039

The first double pulsar system, PSR J0737-3039, was found in 2003 consisting of two radio pulsars, PSR J0737-3039A with a period of 22 ms, and PSR J0737-3039B with a period of 2.7 s. These pulsars are in a tight orbit with

Parameter	Value
Orbital period, P_b	0.420737299122 (days)
Projected semi-major axis, x	3.729464 (sec)
Eccentricity, e	0.2736775
Longitude of periastron, ω	274.57679 (deg)
Epoch of periastron, T_0	50260.92493075 (MJD)
PK Parameter	Value
Advance of periastron, $\dot{\omega}$	1.75578 (deg/yr)
Gravitational redshift, γ	2.070 (ms)
Orbital period derivative, $\dot{P}_b$ (10^{-12})	-0.137
Shape of Shapiro delay, s	0.975
Range of Shapiro delay, r	6.7 (μs)

Table 1.2: PSR B1534+12 Parameters

a 2.4 hr period. This is classed as an exotic system as this is the first of which both NS are observed as pulsars. The almost edge-on orientation of this binary, as viewed form Earth, provides a unique testing ground for GR [18]. In addition to running tests of GR similar to those for PSR B1534+12 with PK Shapiro delay parameters, the double pulsar system allows projected semi-major axis measurements (see Table §**1.3**) from both pulsars yielding a new test of gravitation theories due to the extra constraint. This constraint is obtained by computing a precise mass ratio R of the system, derived from Kepler's third law as:

$$R = \frac{m_A}{m_B} = 1.069 \text{ M}_\odot \tag{1.30}$$

where m_A and m_B represent the masses of PSR J0737-3039A, and PSR J0737-3039B respectively [61]. The measured relativistic corrections of PSR J0737-3039 assigned to a Keplerian description of the system's orbital motion

Parameter	Value
Orbital period, P_b	0.102251563 (days)
Projected semi-major axis, x	1.41504 (sec)
Eccentricity, e	0.087779
Longitude of periastron, ω	73.805 (deg)
Epoch of periastron, T_0	52870.0120589 (MJD)
PK Parameter	Value
Advance of periastron, $\dot{\omega}$	16.9 (deg/yr)
Gravitational redshift, γ	0.38 (ms)
Orbital period derivative, $\dot{P}_b$ (10^{-12})	-1.2
Shape of Shapiro delay, s	0.9995
Range of Shapiro delay, r	5.6 (μs)
Mass Ratio of System, R	1.069 ($M_\odot$)

Table 1.3: PSR J0737-3039 Parameters

finds that PK parameters agree with GR predictions, confirming Einstein's predictions to within 0.05% uncertainty, the most precise gravitational test result to date [60].

1.4.2 Testing GR with a NS-WD Binary System

In exceptional cases, the orbital geometry of a binary pulsar system can be verified by determining the system's orientation using a classical geometric model, thus providing an independent prediction of relativistic effects. PSR J0437-4715, the closest and brightest millisecond pulsar known to date, resides within a nearly circular orbit with a low-mass helium WD companion. High-precision timing of this MSP led to the determination of the three-dimensional structure of its orbit and confirmation that the observed Shapiro delay is consistent with the geometrically derived

constraint on the system's orbital inclination [126].

The importance of accurate instrumental calibration for high-precision pulsar timing was also first highlighted during an analysis of PSR J0437-4715 (amongst the most highly susceptible pulsars to calibration errors [123]), where systematic effects were shown to influence the pulsar's timing residuals. Calibration errors between linear and circular polarization states were also shown to affect the pulse shape when forming the total intensity profile of the pulsar signal. Simply put, calibration errors result in pulse TOA errors, where a 1% calibration error can produce a 100ns shift in the measured TOA [101]. This relationship between the level of timing precision and polarimetric calibration motivated the efforts of Britton (2000), who proposed the Stokes invariant interval for pulsar timing [15][17]. These efforts are the main reason why we can achieve the sensitivity required for testing GR with PSR J0437-4715.

Following on from and improving upon these efforts, further developments have led to state-of-the-art polarimetric techniques; MEM [125] (see Section §**2.1.2**), MTM [124] (see Section §**2.1.3**), and METM [123] (see Section §**2.1.4**) which have been integrated throughout the research undertaken during this thesis.

1.5 Thesis Outline

A list of pulsars, for which polarization calibration is important, was identified by van Straten in 2013 [123]. These pulsars were determined based on the fraction their current timing residuals that could be improved by removing instrumental calibration errors. For this research, we have processed five of these pulsars - the most susceptible to instrumental calibration errors - using state-of the-art, high fidelity polarimetric calibration techniques. The data used are available from the Parkes Pulsar Data Archive [50], a large archive of high quality pulsar observation data spanning years to decades. These data are freely and public available, and therefore no new observations were required. Our analysis required some configuration of the software. Firstly, we needed to adapt the METM scripts that were configured on Swinburne University's old gSTAR supercomputer, to run on their new OzSTAR supercomputer. This required rewriting the software's scripts from PBS to SLURM commands. Secondly, we needed to integrate CoastGuard - a Python application for performing the desired automated Radio Frequency Interference (RFI) excision [65] - into the Pulsar Calibration Pipeline (PSRPL). Thirdly, once our data was cleaned, integrated and calibrated for the chosen pulsars, we produced the pulse TOA estimates and analysed them with two software packages: (i) TEMPO2 [51] to model the white noise, and (ii) TempoNest [66] to model the red noise in the data. Finally we compared the TOA

residual data achieved through PSRPL between the typical method of calibration, which is based on the Ideal Feed Assumption (IFA), and van Straten's (2013) METM calibration method using Scalar Template Matching (STM) and Matrix Template Matching (MTM) techniques. Each combination (i.e. IFA/STM, IFA/MTM, METM/MTM and METM/STM) produces an RMSE and reduced (χ^2/N) statistic for each model. By comparing these results we aimed to show that METM paired with MTM will improve the PTA experimental sensitivity over long periods of time, compared to the other conventional models.

Chapter 2

Research Design

This chapter describes the methodology, instrumentation, software, and analysis procedures used to improve pulsar timing residuals by employing better instrumental calibration techniques. Section §**2.1** provides an overview of polarimetric calibration and the methods of polarimetry for high precision, high-fidelity pulsar timing used, tested and compared on our chosen pulsar timing data. Section §**2.2** details the instrumentation and additional software used throughout this research, including how it will be applied to the data and for what reasons or benefits. Section §**2.3** discusses the development and deployment of PSRPL and the procedures used therein to improve instrumental calibration. And finally, Section §**2.4** will explain the methods of analysis and the importance of the statistical data retrieved throughout this thesis.

2.1 Background

Pulsars emit weak, narrow beams of EM radiation out and along their magnetic poles, and these beams are detectable if they sweep across an observer's line-of-sight as the pulsar rotates [73]. By modelling the phase of this periodic signal, the pulsar's spin period and spin-down rate can be determined to relatively high precision [90]. Noise can be present in the instruments used for detection (i.e. radiometer noise and other instrumental effects) which causes artefacts to be produced during observations [125].

Known pulsars are observed regularly on at least a monthly basis over long periods of time (i.e. spanning years to decades) [50]. For frequently observed pulsars, a series of pulses can be averaged over time to increase the signal-to-noise ratio, driving down the noise in the data to obtain clearer (less noisy) signals [112]. This technique produces an average pulse profile which is purely derived from observational data. An average pulse profile is considered inherently stable and can be cross-correlated with a model pulsar template to provide accurate TOA measurements. Timing residuals - errors in the timing model indicating poor model fit - are then calculated from the resulting TOAs minus the timing model. Incorrectly modelled or unmodelled physical phenomena and noise (see Section §**2.4.1**) in the timing model tends to show as some apparent structure in the timing residuals. With longer observations and regular updates to the timing

model, these discrepancies can be better constrained and parametrised to improve TOA measurements. The process of template matching - comparing predicted TOAs against a noise-free model template against a timing model yields a pulsar's physical parameters [123]. Timing models describe a pulsar system and account for the numerous delays encountered by EM radiation when propagating between the source and observer [51]. The model fitting method implements least-squares minimisation which aims to minimise the reduced χ^2/N statistic which is an objective measure of goodness-of-fit (see Section §**2.4.2**) [123].

TOA precision is heavily dependent on the telescope, the back-end receiver used, and the intrinsic properties of the pulsar. This means that a pulsar is only detectable if the pulse produced exceeds the noise in the signal, especially the noise generated in the telescope receiver. The system equivalent flux density (ΔS_{sys} in Jy) - the observable strength of a source due to system temperature (T_{sys}) - is given by the radiometer equation, which is used to derive the sensitivity of the radio receiver to pulsar signals.

$$\Delta S_{\text{sys}} = \frac{T_{\text{sys}}}{G\sqrt{n_p t_{\text{obs}} \Delta f}} \tag{2.1}$$

where T_{sys} is the system temperature (in Kelvins), t_{obs} is the integration time, n_p is the number of polarizations used, G is the gain of the telescope (Jy K^{-1}) and Δf is the observational bandwidth (MHz). Calculating ΔS_{sys}

yields the performance of a system. The Parkes 64-m radio telescope's 20-cm Multibeam receiver has an system performance $\Delta S_{\rm sys}$ of 30 Jy [71]. To maximise sensitivity the receiver should be cooled [75]. Longer observations in wider bandwidths with both polarisations recorded are required to improve the measured TOA estimates to high-precision [111].

A pulsar's intrinsic properties can also affect TOA precision. For example, brighter pulsars with narrow mean pulse profile produce the lowest timing errors [70]. While taking these factors into consideration, pulsar timing aims to measure and model the pulse phase as a function of time for every single rotation of the star to a high level of accuracy in order to predict future TOAs [49]. Precision TOAs will provide improved detection sensitivity in the search for low frequency GWs via PTAs [123]. High-precision pulsar timing requires many TOA measurements from the brightest and fastest MSPs as they exhibit sharp, narrow pulse profiles [69].

2.1.1 Polarimetric Calibration

EM waves are composed of both an electric and magnetic field with orthogonality (at right angles to each other). Polarisation identifies the geometrical orientation of waves oscillations. Polarisation of a transverse EM wave e.g. a pulsar signal, refers to the direction (linear and/or circular polarisation states) of the electric field. The linear plane of polarization can change as the wave propagates along the line-of-sight path between the

source and a distant observer. The circular polarisation describes the constant rate of rotation, either left- or right-handed, as the plane as the wave travels [95]. These changes in orientation of light are caused by

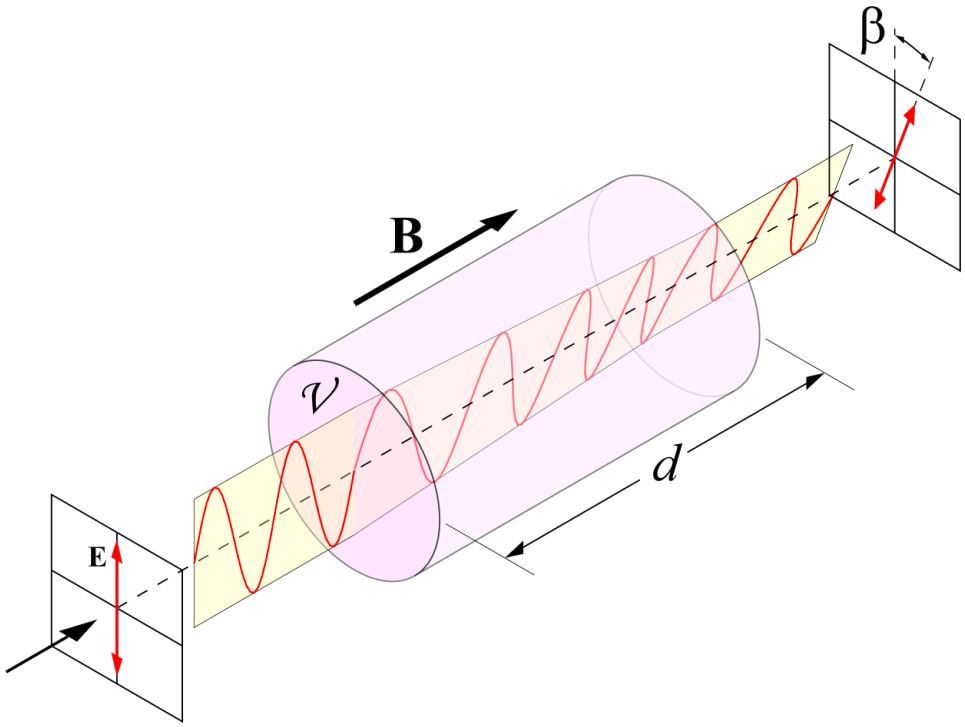

Figure 2.1: **A conceptual diagram of a beam of polarised EM radiation passing through a birefringent material such as the gas and dust clouds in the ISM, with known length and applied magnetic field strength [35].**

Faraday rotation or the Faraday Effect (see Figure §**2.1**), named after its discoverer Michael Faraday who found the link between light and magnetism in 1845. Faraday rotation is a magneto-optical phenomenon which occurs when light passes through birefringent materials, such as radio waves through the ionised ISM, within the presence of a parallel magnetic

field. Faraday depth ϕ is used to describe the amount of Faraday rotation along the line-of-sight and is related to the rotation measure, RM, by

$$\phi = \mathrm{RM}\lambda^2 \tag{2.2}$$

where λ is the wavelength (in meters) and the Faraday rotation measure RM (in rad s^{-2}) is defined by

$$\mathrm{RM} = 0.81 \int_0^D n_e \boldsymbol{B} \cdot d\boldsymbol{l} \tag{2.3}$$

where D is the pulsar distance (pc), n_e is the electron density (cm^{-3}), $\boldsymbol{B}$ is the magnetic field vector in μG and $d\boldsymbol{l}$ is the elemental vector along the line-of-sight between the pulsar and observer [43]. Faraday rotation measures of linearly polarised pulsar radiation have been used to study the ISM and measure the diffuse, large-scale galactic magnetic fields of our Milky Way galaxy [43][44][84].

Polarisation measurements are important for providing insights into the propagation and emission of radio waves through the ISM, and combined with pulse profile shapes can be used to describe the pulsar emission properties [23]. The polarisation state of a signal is represented by the four Stokes parameters, named after Sir George Gabriel Stokes [115] who first

defined them, as

$$S = \begin{bmatrix} S_0 \\ S_1 \\ S_2 \\ S_3 \end{bmatrix} = \begin{bmatrix} I \\ Q \\ U \\ V \end{bmatrix} \tag{2.4}$$

where I is the total intensity of the signal, Q, U and V measures the difference in the flux densities of the; horizontal and vertical linear polarisations, ± 45 degree linear polarisations, left and right circular polarisations respectively (see Figure §**2.2**). These Stokes parameters can be characterised as the sums

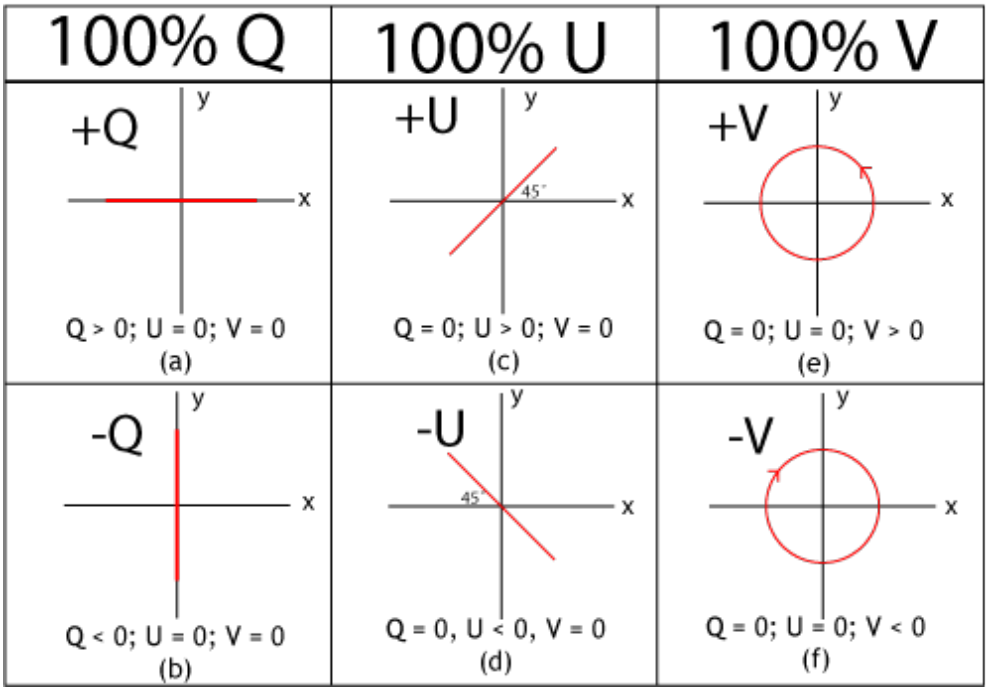

Figure 2.2: **Stokes Q, U and V parameters and their relationship for polarisation ellipse, its orientation, and the direction of rotation [23].**

and differences of measured electric field vectors for a signal, by

$$\begin{bmatrix} I \\ Q \\ U \\ V \end{bmatrix} = \begin{bmatrix} E_x^2 + E_y^2 \\ E_x^2 - E_y^2 \\ 2E_x E_y \cos\Delta\phi \\ 2E_x E_y \sin\Delta\phi \end{bmatrix} \tag{2.5}$$

where $\Delta\phi = \phi_y - \phi_x$ is the phase difference at time $t = 0$, and the E_x and E_y terms are the amplitudes of the two complex-valued components of the transverse electric field vector [23]

$$e(t) = \begin{bmatrix} E_x(t) \\ E_y(t) \end{bmatrix} \tag{2.6}$$

with measurable properties of $e(t)$ described by the coherency matrix

$$\rho = \langle e(t) \otimes e^{\dagger}(t) \rangle \tag{2.7}$$

where angle brackets denote time averaging, $\otimes$ denotes the tensor product and $\dagger$ indicates the Hermitian transpose of $e(t)$. The coherency matrix is also the linear combination of Hermitian basis matrices, defined by

$$\rho = \frac{1}{2} \sum_{k=0}^{3} S_k \sigma_k = \frac{(S_0\sigma_0 + \boldsymbol{S} \cdot \boldsymbol{\sigma})}{2} \tag{2.8}$$

with σ_0 as the identity matrix, $\boldsymbol{\sigma} = (\sigma_1,\ \sigma_2,\ \sigma_3)$ is a three-vector with matrix-valued components, σ_1, σ_2, σ_3 are the Pauli spin matrices, S_0 is the total intensity (i.e. Stokes I), and $S = (S_1, S_2, S_3)$ [16]. The polarisation measurement equation - the basis by which pulsar polarisation is used to model an unknown instrumental response - is based on the congruence transformation of the coherency matrix [125],

$$\rho^{'} = J\rho J^{\dagger} \tag{2.9}$$

where J is the complex-valued Jones matrix

$$J = \begin{bmatrix} j_{xx} & j_{xy} \\ j_{yx} & j_{yy} \end{bmatrix} \tag{2.10}$$

.

The Ideal Feed Assumption (IFA) is the typical assumption model amongst the radio astronomy community for dealing with radio sources and their polarisation states. IFA assumes the receptors have perfect orthogonal polarisation, the reference noise source is 100% linearly polarised, and that the artificial noise source (e.g. noise diode) used to calibrate the response illuminates both receptors equally (equal in phase and amplitude) [94]. During the reception of radio waves, instrumental distortion is introduced and must be corrected. The instrumental response can be determined by

observing at least two calibrated, well known sources of polarised radiation; this response can then be inverted to calibrate observations of other sources. Alternatively, in the scenario where there are not enough calibrator sources, instrumental calibration can be performed by fitting polarimetric data to a predictive model. This method is known as Measurement Equation Modelling (MEM) [125].

2.1.2 Measurement Equation Matching

MEM was developed by van Straten (2004) to determine the polarimetric response exhibited by radio observatory instrumentation [125]. The polarization measurement equation forms the basis through which measured quantities are related to the intrinsic polarisation of radio sources and are used to model the unknown instrumental response [42].

Radio pulsar observations exhibit exceptional stability over much longer time-scales than calibration observations. Multiple on-pulse longitudes from single pulsars may be included as unique and stable input source polarizations. Any non-pulsed background polarization is also effectively eliminated by subtracting the off-pulse mean from each integration pulse profile. For these reasons, radio pulsar observations are an excellent source for constraining the polarization measurement equation. The conventional means for solving this equation is through least-squares minimisation which requires a scalar figure-of-merit function (i.e. the reduced χ^2/N) to indicate

goodness-of-fit, and the calculation of both its gradient and curvature with respect to the model parameters [125].

MEM was used to determine the instrumental response of the Parkes Multibeam receiver which has an artificial reference noise source (e.g. noise diode) to ideally inject 100% linearly polarised signal into the telescopes receiver feed horn with a position angle of 45°. Dual-polarisation observations were taken with Parkes for the nearest and brightest MSP discovered to date, PSR J0437-4715, and the bright radio galaxy 3C218, known as Hydra A. These observations took place on the 19th and 20th of July, 2003. The two 64-MHz bands were centred at 1341 and 1405 MHz, and were two-bit sampled and processed by the second generation of the Caltech-Parkes-Swinburne Recorder (CPSR-II). The detector's power and sampling thresholds were monitored and updated every second. The Stokes parameters were derived from the signal's polarisation and integrated as a function of topocentric pulse phase - pulse phase measured from a particular point on the earth's surface - with data averaged over 5 minute intervals. The produced mean pulse profiles were uncalibrated with 2048 phase bins (equivalent to a time resolution of approximately 2.8 μs. Results indicated that the reference signal produced by the Parkes Multibeam receiver's noise diode was not actually 100% linearly polarised, but approximately 90% linear and 3% circularly polarised. The position angle was also shown not to be exactly 45°. The edges of the observing band were

severely depolarised as a result of frequency aliasing and scattered power (a digitisation effect [123]) during down conversion. To model the reference signal, Stokes I was set to unity to produce an intermediate flux scale, while Stokes Q, U and V varied as free model parameters. The reduced χ^2/N merit function was evaluated at 1.05, indicating a good fit across each frequency channel. From here, assuming the measured Stokes parameters are normally distributed, the standard errors in each model parameter could be derived [125].

2.1.3 Matrix Template Matching

Matrix Template Matching (MTM) was developed by van Straten (2006) as a new method for improving pulsar timing analysis. Compared to conventional methods based on only the total intensity (i.e. Scalar Template Matching (STM)), the MTM method takes additional timing information from the polarisation data of a pulsar signal by modelling the transformation between two polarised light curves in the Fourier domain [124], where STM measures TOAs using only the observed total intensity light curve [125]. This technique models the transformation between calibrated pulsar timing templates with high signal-to-noise and the uncalibrated pulsar observations, effectively estimating the instrumental response and improving pulsar timing precision. A number of MSPs are predicted to exhibit greater precision and accuracy of TOA estimates derived from polarimetric data using MTM compared to those derived from

only the total intensity using conventional methods [124].

For MTM, a high signal-to-noise pulse profile was obtained by averaging over many pulse profiles, creating a template to which individual observations are matched. The best fit phase shift from this method of template matching was then used to compute the pulse TOAs [125]. For MTM, by taking the observed Stokes parameters derived from the pulsar signal and their discrete Fourier transforms, one can model the phase shift between the template and observed total intensity profiles in the Fourier domain. The best fit model parameters for minimising the merit function (i.e. the reduced χ^2/N statistic) can then be determined using the Levenberg-Marquardt method. TOA estimates derived from the polarisation profile are expected to have greater precision than those derived from the total intensity profile alone. However, the effectiveness of MTM depends on both the degree of polarisation and the variability of the polarisation vector as a function of pulse phase, as these properties determine the extent to which the phase shift is correlated with the free parameters in the timing model. Furthermore, instrumental distortions seen in the analysis of STM are predicted to produce systematic timing errors of the same order as the RMSE timing residuals in the current best data sets. These errors are completely eliminated using MTM. Therefore, it is expected that MTM will perform better than conventional methods in the majority of experiments. MTM also allows for fully calibrating the

instrumental response using a single observation of a well-determined pulsar [124].

2.1.4 Measurement Equation Template Matching

METM was developed by van Straten (2013) combining the temporal variations built into MEM [125] with the stability of MTM [124] polarimetric calibration models to further improve the precision and accuracy of pulse TOAs. METM derives the instrumental response of the 64-m Parkes radio telescope from regular observations of the MSP PSR J0437-4715 whose mean polarised emission is assumed to be constant over time. METM provides high-fidelity polarimetry over long time scales. This technique was applied to calibrate 7.2 years of high-precision PSR J1022+1001 timing data followed by MTM for TOA estimation and demonstrated improved timing residuals compared to conventional methods. METM's high level of precision allowed for the first measurements of the secular variation of the projected semi-major axis, the precession of periastron, and the Shapiro delay [123].

2.2 Instrumentation

In addition to the use of METM [123] for instrumental calibration, and MTM [124] for estimating TOAs, a number of other software and instrumentation are worth discussing as they are a key component in our TOA analysis. This

section will discuss each of these tools and their use/benefits for improving the timing solutions.

2.2.1 The Parkes Observatory

The Parkes Observatory is a 64-m radio telescope (see Figure §**2.3**) located in Parkes, New South Wales, Australia. Led by the Commonwealth Scientic and Industrial Research Organisation (CSIRO), Parkes began operations in 1961 as part of the Australian Telescope National Facility (ATNF). The 64-m parabolic dish is the second largest single-dish radio telescope in the southern hemisphere. Since it was commissioned, Parkes is now 10,000 times more sensitive with many upgrades made over the past decades to keep up with the ever-evolving, cutting edge of radio astronomy [7]. Parkes typically operates at cm wavelengths, although can be used from 80-MHz to 22-GHz frequencies. Parkes has discovered more than 1000 radio pulsars [88].

There are two main receivers on the Parkes telescope, the 21-cm Multibeam, and the Ultra Wide-bandwidth Low (UWL) receiver. The Multibeam receiver was introduced in 1996 consisting of 13 circular beam horns, to allow simultaneous observations of 13 independent patches of sky, configured in a hexagonal cluster at the prime focus of the 64-m dish. Each beam is capable of detecting the orthogonal linear polarisations of a signal. The Multibeam receiver was primarily designed to achieve low system noise

temperatures for making deep, large area surveys of neutral hydrogen emission from external galaxies to high precision [114]. The UWL receiver

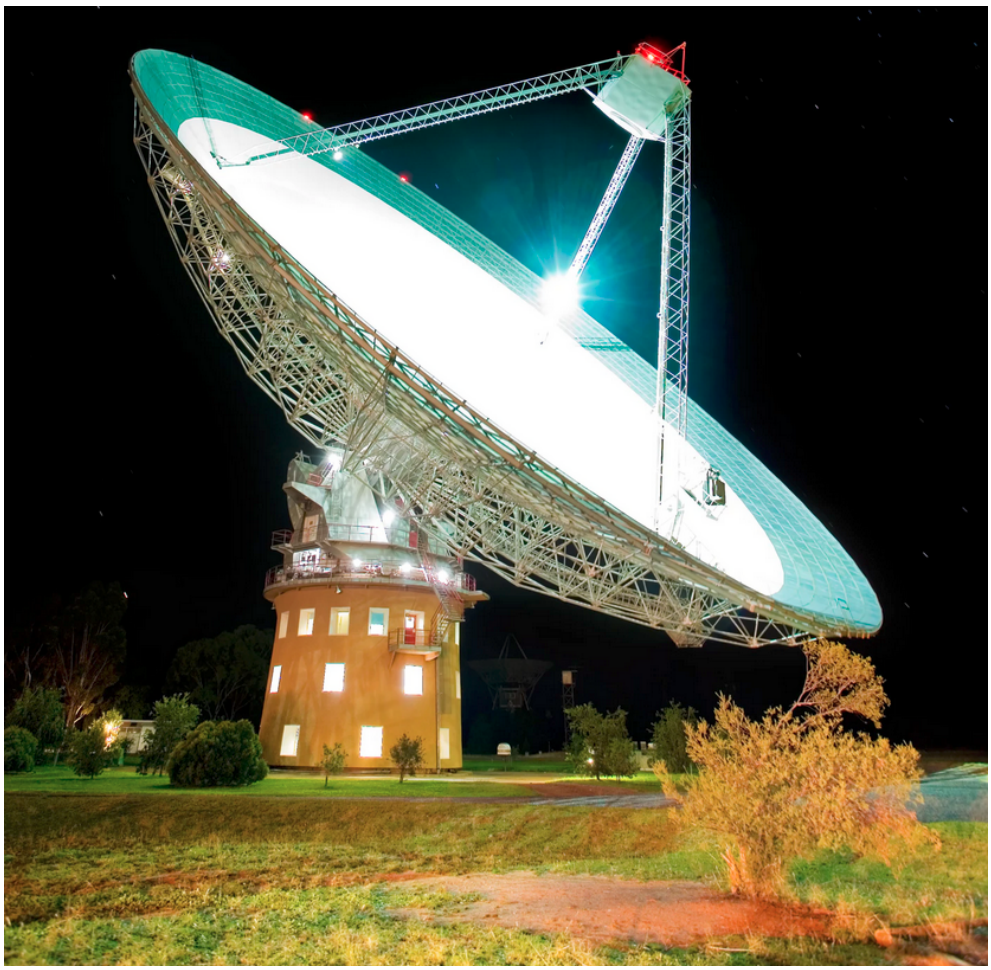

Figure 2.3: **The Parkes 64-m telescope [89]**

began operations in 2018, providing continuous coverage over a wide frequency range from 700 MHz to 4.2 GHz [31].

Pulsar observations recorded at Parkes are stored in the CSIRO Data

Access Portal. The Parkes Pulsar Data Archive contains all of the observed pulsar data recorded at Parkes, including the metadata describing these observations and the recorded signal from the instrument [7]. All data in the archive are stored in a standard PSRFITS format based on the Flexible Image Transport System (FITS). PSRFITS is one of the file formats used by PSRCHIVE, an open source object-orientated data analysis software tool for viewing, editing, and pre-processing pulsar data for timing analysis. PSRCHIVE also allows for data calibration, statistical analysis and producing quality plots for data visualization [53].

Pulsar data were processed using the Swinburne University of Technology's Centre for Astrophysics and Supercomputing has operated a supercomputer facility since 1998, providing tools for a range of astronomical research, including processing of radio telescope data. These supercomputers are available to Swinburne University researchers and their collaborators. Until the latest supercomputer was installed in 2018, its predecessor, the GPU Supercomputer for Theoretical Astrophysical Research (gSTAR) was the show-runner, performing to well beyond 100 Teraflop/s. The next generation of supercomputer, OzSTAR, was designed with Petaflop/s performance to assist in the computational efforts required for research by Swinburne's Centre of Excellence in Gravitational Wave Discovery (OzGrav). The OzSTAR supercomputer is one of Australia's most powerful computers with a peak performance of 1.2 Petaflop/s, empowering OzGrav

to pursue the detection of GWs from SMBHs [21].

2.2.2 CoastGuard

The first stage in our signal processing pipeline is Radio Frequency Interference (RFI) mitigation. Developed by Lazarus in 2006 [64], CoastGuard is a python scripted, automated pipeline for the application of sophisticated RFI mitigation techniques. CoastGuard is compatible with psrchive to read and write data files, allowing good-quality RFI removal to be integrated with relative ease. CoastGuard implements a number of RFI excision algorithms that can be applied simultaneously to clean pulsar timing data. These algorithms are: (i) the rcvrstd algorithm which zero-weights any unnecessary frequency channels beyond the range of the telescope's receiver response, or channels within bad frequency intervals, (ii) the surgical algorithm which finds and removes profiles corrupted by RFI, (iii) the bandwagon algorithm which removes any sub-integrations and/or channels that have a large portion of masked data, and (iv) the hotbins algorithm which replaces any off-pulse profile phase bin outliers with locally sourced noise. Both rcvrstd and surgical algorithms were intended to be used in dual application for RFI mitigation, where standard deviation, mean, range, and maximum amplitudes of the Fourier transform are computed for each sub-integration and channel pair's mean-subtracted residuals, in order to remove any biases that could be present in the software.

These algorithms were chosen for being highly sensitive to radio frequency interference signals, and for each metric a $N_{sub} \times N_{chan}$ matrix is produced where any trends among the columns and rows are removed as they account for slow variations in time and shape of the band-pass filter. Any outlier values of 5 σ from the median are removed, as well as any pulse profiles that are determined to be outliers. Both BANDWAGON and HOTBINS are optional algorithms for quality control, to be used in the case of observations that may still require to be cleaned manually after RCVRSTD and SURGICAL are complete. This feature allows the user to detect any observations over-contaminated by RFI that may have been overlooked [64].

2.2.3 Tempo2

Pulsar TOAs are measured from radio observatory data acquired over many years [50]. Systematic deviations in the timing residuals may appear when calculating the differences between the actual TOAs and best-fit model TOAs, indicative that the model does not fully describe the true pulsar parameters [120]. These discrepancies may be caused by a number of different effects: (i) pulsar spin irregularities (e.g. timing noise and glitches), (ii) orbital dynamics, (iii) astrometry, (iv) ISM (e.g. DM variations), (v) solar system delays, (vi) time delays, (vii) instrumental noise, and (viii) GWs. The precision of estimated model parameters can be improved with longer data sets that span years to decades; therefore,

long-term stability is also a key requirement of high-precision pulsar timing [51].

The TEMPO software package was designed as a mathematical model for pulse arrival time analysis. TEMPO was introduced with the demand for better pulsar timing models, which grew with the number of pulsar detections and discoveries being made. However, TEMPO algorithms used to perform the necessary timing conversions and delay corrections (see Section §**1.3**) were implemented with limited accuracy. Additionally, the software was capable of analysing only one pulsar at a time and yielding timing residuals of ∼100 ns. With a need for improving pulsar timing to greater precision, especially for GW detection via PTAs, TEMPO2 was born, with design based on the original TEMPO but with improved algorithms and the added ability to analyse multiple pulsars simultaneously [33].

TEMPO2 uses an initial model to generate a set of pre-fit residuals. The timing model parameters are then adjusted via linear least-squares minimization to improve the model fit. During the fitting process, TOAs are modelled as the sum of a deterministic signal based on a timing model and a white noise component that describes the TOA uncertainties. However, for realistic data, this assumption is rarely true. For example, if either: additional stochastic processes (e.g. the GWB), or red noise intrinsic to the pulsar (e.g. rotational irregularities in the NS), are present

in the data, then these contributions will bias the timing model and will affect the overall accuracy of pulsar parameter estimates [51]. This issue is addressed by the TEMPO2 plug-in TEMPONEST [67] which enables analysis of linear or non-linear red noise, and/or additional stochastic parameters in the timing model, using the Bayesian inference tool, MULTINEST [36], while still using TEMPO2 to evaluate the timing model [67].

2.3 Methodology

Research began with the following question in mind: "By how much can pulsar timing precision and accuracy be improved through better polarimetric calibration?". To answer this question, we first developed and extended PSRPL, which was originally designed and maintained by van Straten and colleagues since 2006 [116]. We introduced state-of-the-art RFI mitigation algorithms and analysis software for performing the necessary timing conversions and delay corrections, as well as for modelling the white and red noise components in the timing data. This is a novel idea, as these respective software are designed with individual capabilities for improving the performance of pulsar timing techniques, yet they have never before been used collaboratively. PSRPL largely automates the processing and analysis of large amounts of pulsar timing data. We then both tested and configured PSRPL with PSR J0437-4715 data from the Parkes Observatory Pulsar Data Archive which was recorded using the CASPSR instrument on

the Parkes 64-m dish, spanning approximately 8 years for each pulsar in our analysis [50]. PSRPL is freely available for use.

PSRPL was originally operating on Swinburne's gSTAR supercomputer via Portable Batch System (PBS) [117] command scripts. However, gSTAR was decommissioned sometime between late 2018 and early 2019 rendering PSRPL obsolete. In order to resurrect PSRPL, these scripts had to be adapted to use SLURM [110] commands on the new OzSTAR supercomputer [56]. These scripts automate the process launching multiple data analysis tasks in parallel on the cluster, and issue commands as required to perform the different steps required for polarimetric calibration and pulsar timing analysis. Once the PSRPL environment is set up, the CoastGuard RFI mitigation software [64] was integrated to clean the data. With RFI excised data in hand, five-minute integrations can then be produced for a chosen pulsar (e.g. PSR J0437-4715) and a calibrator (e.g. HYDRA), then divided into observing sessions. When the five-minute integrations are prepared and any bad integrations are removed for both the pulsar and calibrator, then the data is ready for polarimetric calibration. From this point, one can either use PSRPL to calibrate pulsar observations using only the pulsed noise diode (IFA) or the METM procedure [123], in which a high signal-to-noise, well-calibrated, template polarization profile for PSR J0437-4715 is created and used to generate a large set of models for calibrating the remaining pulsars in our sample.

The calibrated archives have integration lengths of approximately one hour. The data are zapped to remove any faulty edges, and then integrated over frequency. A template profile is chosen from the produced list, determined by highest signal-to-noise ratio for the integrated total of each observing session. MTM [124] is then used to produce TOA estimates.

At this stage in the pipeline, we are ready for analysis and plotting using the TEMPO2 [51] and TEMPONEST [67] software. TEMPO2 will perform the necessary timing conversion and delay corrections, and also allows for the modelling of the white noise component in the timing data [51]. TEMPONEST is then used to perform the analysis of any additional stochastic parameters and model the red noise component [67].

To summarize, our research question will be addressed using a quantitative research methodology that includes analysis of existing data and comparison of descriptive statistics that characterise different aspects of the noise that are important in pulsar timing experiments. Our experimental procedure includes the following steps [116]:

1. Download and configure the PSRPL environment
2. Clean up the data (using CoastGuard)
3. Prepare five-minute integrations

4. Calibrate the data

   a) Apply IFA to all pulsars

   b) Apply MEM to PSR J0437-4715 and produce a well-calibrated template

   c) Apply METM to PSR J0437-4715 and produce a database of solutions

   d) Apply METM solutions to all pulsars

5. Produce TOA estimates

   a) Using STM

   b) Using MTM

6. Analyse TOAs

   a) Using TEMPO2

   b) Using TEMPONEST

2.4 Analysis

In this research, we study 5 pulsars observed with roughly a monthly cadence using the Parkes 64-m radio telescope [7]. We selected the top pulsars (listed in Table §**2.1**) that are most susceptible to calibration error, as predicted by van Straten (2013), relative to the arrival time precision reported in the PPTA second data release (2020). The pulsar observations used throughout this analysis were obtained using the 20-cm Multibeam receiver [114], with

Table 2.1
Relative Arrival Time Uncertainties and Systematic Timing Error

PSR	τ_β (ns)	σ_τ (ns)	τ_β/σ_τ	$\hat{\sigma}_\varphi$
J0437-4715	205	116	1.77	0.85
J1744-1134	108	385	0.28	1.56
J2129-5721	225	964	0.23	1.15
J1600-3053	119	572	0.21	0.90
J1022+1001	278	1555	0.18	0.68
J2145-0750	147	955	0.15	0.95
J1730-2304	196	1322	0.15	0.71
J1909-3744	22	152	0.14	1.02
J1045-4509	338	2570	0.13	0.88
J1643-1224	269	2248	0.12	0.91
J1732-5049	74	635	0.12	0.96
J1603-7202	143	1316	0.11	0.85
J1857+0943	121	1208	0.10	0.89

Table 2.1: Predicted Timing Error for 1% Calibration Error
A list of PPTA pulsars observed at 20-cm which are susceptible to calibration errors. τ_β is the predicted timing error for a 1% calibration error [123]. σ_τ is the current best timing precision recorded in the PPTA second data release [58]). τ_β/σ_τ is the fraction of current timing residual that could be due to calibration error. $\hat{\sigma}_\varphi$ is the relative uncertainty of MTM versus STM [123].

256 MHz of bandwidth divided into 1024 frequency channels and folded into 1024 phase bins. Each pulsar is observed for about an hour depending on its flux density [53].

2.4.1 Arrival Time Estimates

If all physical effects are correctly modelled and all sources of experimental uncertainty are accounted, then ideal pulsar timing residuals will be

consistent with zero. Pulsar timing residuals which have deviated from zero are the result of either: (i) incorrect parameters in the timing model, (ii) inadequate estimation of TOA errors, or (iii) incorrectly or incompletely modelled physical phenomena affecting TOAs. We characterise the precision and accuracy of our TOA estimates via the reduced χ^2/N and weighted RMSE (wRMSE) (see Section §**2.4.2**) of the post-fit residuals [123].

Estimated uncertainties are correct if the recorded profiles are characterised solely by white noise (i.e. radiometer noise) and if the profile template precisely represents the intrinsic shape of the integrated pulse profile [51]. Unfortunately, a number of other factors can lead to errors in the uncertainty estimations, including: unmitigated RFI, temporal variations (e.g. in mean profile shape), artefacts from instrumental instabilities, and/or imperfect profile templates [69]. Therefore, we use TEMPONEST to evaluate the scalar multiplicative correction factor (EFAC) and quadrature-added error (EQUAD) terms (see Section §**2.4.3**), which mathematically model the uncorrelated noise from physical processes that introduce uncertainty in the TOAs [67]. In summary, we first used TEMPO2 [51, 33] to model the arrival time estimates and produce best-fit timing parameters for each pulsar, starting with the timing parameters that were used to fold the CASPSR data. We then used TEMPONEST to model the additional white noise (described by EFAC and EQUAD) and red noise (a

power law described by $A_{\rm red}$, and β) in the signal from each pulsar, starting with uniform priors on the logarithms of the white and red noise model parameters (see Section §**2.4.4**) [67]. After subtracting the red noise model produced by TEMPONEST, we computed the post-fit reduced χ^2/N and wRMSE statistics. These statistics, combined with EFAC and EQUAD, should then fully describe the white noise, and the timing solutions should have reduced χ^2/N equal to unity."

2.4.2 Statistical Parameters

The reduced χ^2/N statistic is a test for measuring the goodness-of-fit between experimental data and a best fit timing model. Optimal model parameter values are obtained by minimising the reduced χ^2/N statistic.

$$\chi^2/N = \sum_{i=1}^{N} \frac{(x_i - \mu_i)^2}{\sigma_i^2} \tag{2.11}$$

where N represents the degrees-of-freedom (i.e. the number of observations minus the number of fitted parameters), x_i represents the $i^{\rm th}$ observation, μ_i is the model prediction for the $i^{\rm th}$ value, and σ_i is the estimated uncertainty of the $i^{\rm th}$ observation. In general, the reduced χ^2/N statistic should approach unity when there is a good fit between the data and the model. A reduced $\chi^2/N > 1$ indicates that either the model does not fully describe the data or the uncertainty has been underestimated, while $\chi^2/N < 1$ indicates that the data have been over fitted (i.e. the model is

improperly fitting the noise) or the error variance is overestimated [12].

As uncertainties of TOAs can significantly vary, it is customary to compute a wRMSE value,

$$\text{wRMS} = \sqrt{\sum_{i}^{n} \sigma_i (\mu_i - x_i)^2} \tag{2.12}$$

where σ_i represents the i^{th} weight.

2.4.3 EQUAD and EFAC

Each TOA is treated as the sum of the timing model (deterministic terms), plus white noise (radiometer noise, pulse-phase jitter, and instrumental effects), plus red noise (GWs, pulsar spin noise, and noise from the ISM). The uncertainties of timing residuals typically reflect the uncorrelated radiometer noise. Therefore, TOA estimates typically underestimate the errors induced by unmitigated RFI, temporal variations in profile shape, instrumental instabilities, and/or imperfect pulsar templates [69].

These underestimations can directly affect the timing model parameter estimates. To overcome this problem, EFAC can be applied to TOAs to adjust uncertainties by a constant scale factor. A second possible solution is to increase the uncertainties by EQUAD, adding a constant noise level to account for any additional scatter in the TOAs. To improve the TOA uncertainties for a given pulsar, the EQUAD (Q) and EFAC (F) parameters

can be applied to counter any additional noise and provide optimal TOAs by adjusting the uncertainty as:

$$\sigma'^2 = F\sigma_0^2 + Q \tag{2.13}$$

EFAC and EQUAD values are typically applied to all TOAs in a pulsar data timing set and are adjusted until the reduced χ^2/N of the fitted model reaches unity [107].

2.4.4 Red and White Noise Amplitudes

TEMPONEST models correlated red noise, intrinsic to the pulsar, if and when present in TOAs. Red noise in TOAs may be present due to a stochastic GWB dominating the timing residuals. Unfortunately, the presence of red noise in the signal would cause fluctuations and delays in GW detections by PTA's by possibly 10 or more years when compared to predicted TOAs from white noise dominated models [67]. However, although the underlying processes behind red noise are unknown [69], the red noise in TOAs can be parametrised based on the red noise amplitude ($A_{\rm red}$ in units of $\rm yr^{(3/2)}$) and spectral index (β) [90]. TEMPONEST uses Bayesian methods to model TOAs in the presence of red noise as a power law red noise model [67]. The power law is derived as follows:

$$P_r(f) = \frac{A_{\rm red}^2}{12\pi^2}\left(\frac{f}{f_{\rm yr}}\right)^{\beta} \tag{2.14}$$

where $f_{\rm yr}$ is a reference frequency of 1 cycle per year [90]. This technique is used to model the red noise in TOAs and better determine the timing model parameters [67].

Chapter 3

Results

Throughout this chapter we present the results of our analysis on a sample of five MSPs, chosen based on their high levels of susceptibility to calibration errors (see Table §**2.1**), as predicted by van Straten (2013). Our analysis has involved the novel approach of incorporating both new and improved (i.e. state-of-the-art) pulsar timing tools into one optimal pulsar timing polarimetric calibration pipeline, PSRPL, with the aim of reducing such calibrations errors and improving pulsar timing precision and accuracy. Our prime method of instrumental calibration is the METM algorithm [123], followed by MTM for TOA estimation [124]. Our findings are compared to the TOA residuals derived using conventional methods (i.e. IFA and STM), given the same 20-cm CASPSR data from Parkes. The results for each pulsar are: (i) tabulated as the red and white noise timing data statistics, (ii) plotted as the post-fit uncertainty-weighted timing

residuals, (iii) plotted as the white (i.e. red noise reduced) timing residuals, and (iv) plotted as corner plots that depict the two-dimensional likelihood surfaces and one-dimensional marginalised distributions for each of the white noise and red noise parameters of interest, as derived from the chains output by the MultiNest Bayesian inference tool used by TempoNest to explore the joint parameter space. All results provided are derived from TEMPO2 [51] and TEMPONEST [67] with some additional post processing used to produce the corner plots. The sections in this chapter are separated as follows: Section §**3.1** PSR J0437-4715, §**3.2** PSR J1022+1001, §**3.3** PSR J1045-4509, §**3.4** PSR J1600-3053, and §**3.5** PSR J1643-1224. A discussion of these results is then provided in the next chapter (see Section §**4.1**).

3.1 PSR J0437-4715

Our first target is the closest, brightest MSP and is one of the most precisely located objects beyond the solar system. Located 157 pc (4.8×10^{15} km) from Earth [127], PSR J0437-4715 is named by its right ascension (RA) 04:37:15 (h:m:s) and declination (DEC) -47:15:08 (deg:m:s) coordinates on the celestial sphere. This neutron star is in a 5.7 day orbital period binary system with a low mass WD companion. Furthermore, PSR J0437-4715 is an MSP, completing one full rotation every 5.75 ms [57]. The long-term rotational stability of PSR J0437-4715 is among the most accurate of the known pulsars, rivalling the timing stability of even the best

man-made atomic clocks [71]. Observable across visible, x-ray, and radio wavelengths, this binary MSP is one of (if not the most) frequently observed pulsars to date, due to its location and brightness [126]. At 20-cm wavelengths, PSR J0437-4715 has a full-width half-maximum of 130 μs and an average flux density of 140 mJy, making it a prime target for high-precision pulsar timing research. In the van Straten (2013) paper, this object is predicted to be one of the most susceptible (207 ns) to 1% calibration error [123].

Table 3.1

METHOD	wRMSE (μs)	RMSE (μs)	EFAC	EQUAD (μs)	$\log_{10}(A_{\rm red})$	β
METM/MTM	0.468	0.061	2.8(4)	0.057(6)	-13.52(6)	-3.0(3)
METM/STM	0.522	0.149	9.5(1)	0.02(2)	-13.8(2)	-4.0(9)
IFA/MTM	0.466	0.068	3.0(3)	0.065(5)	-13.56(7)	-3.2(3)
IFA/STM	0.783	0.589	12.4(6)	0.48(6)	-13.8(5)	-4(2)

Table 3.1: PSR J0437-4715 Timing Noise Statistics for 340 TOAs
The columns are defined as follows: wRMSE the weighted post-fit timing residual RMSE, RMSE the white noise (red noise removed) timing residual RMSE, EFAC the scalar multiplier by which all error bars are scaled, EQUAD the quadrature-added error, $A_{\rm red}$ the (dimensionless) red noise amplitude, and β the red noise slope.

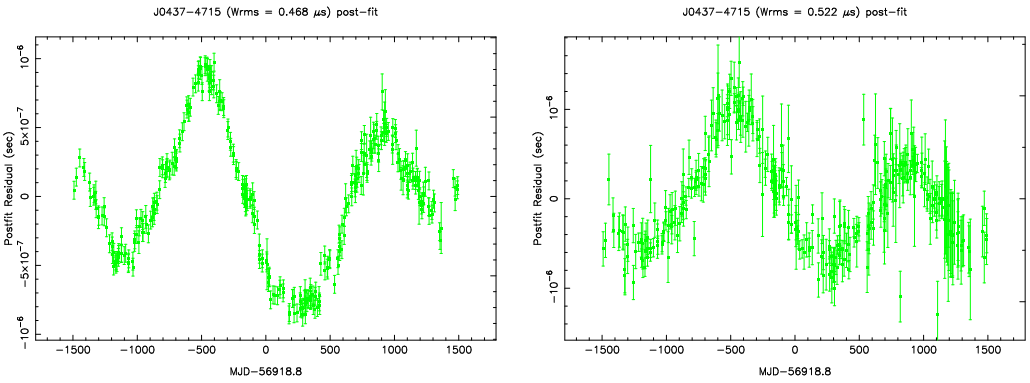

(a) METM/MTM

(b) METM/STM

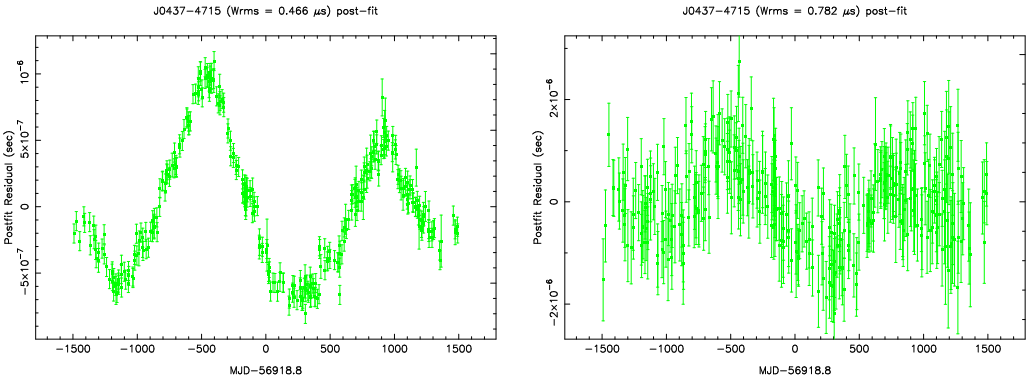

(c) IFA/MTM

(d) IFA/STM

Figure 3.1: PSR J0437-4715 Post-fit Residuals

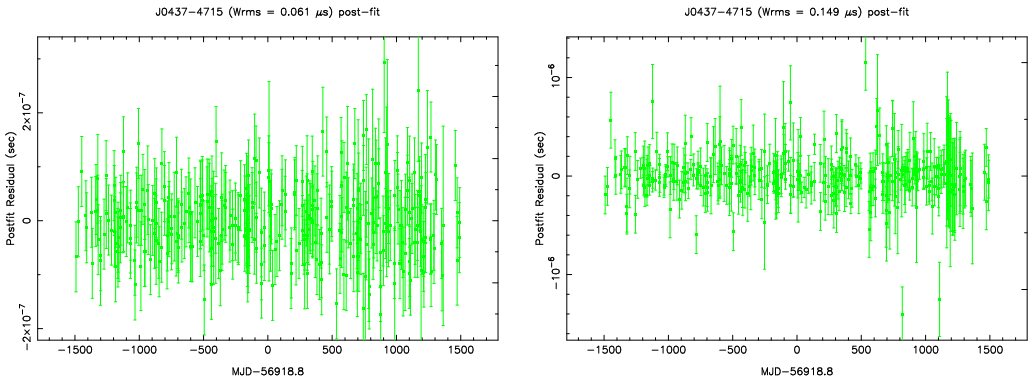

(a) METM/MTM

(b) METM/STM

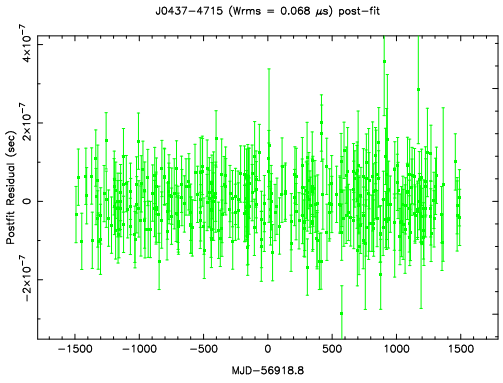

(c) IFA/MTM

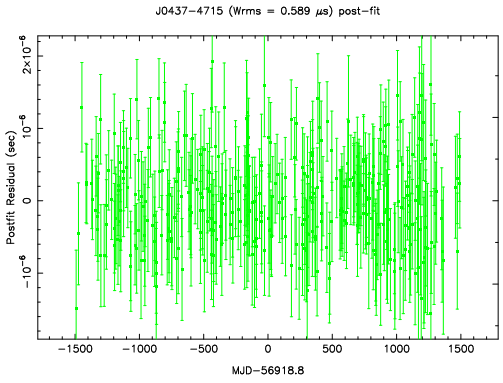

(d) IFA/STM

Figure 3.2: PSR J0437-4715 White Noise Residuals

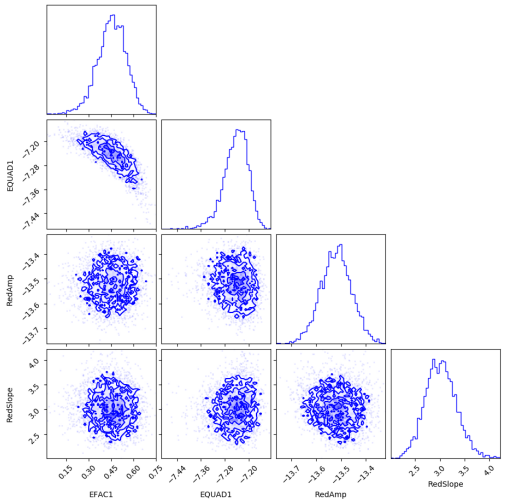

(a) METM/MTM

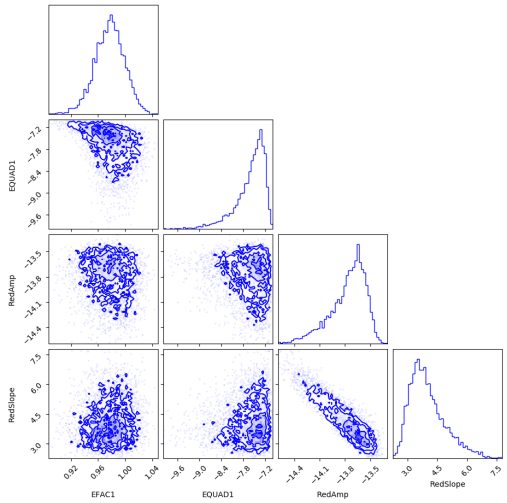

(b) METM/STM

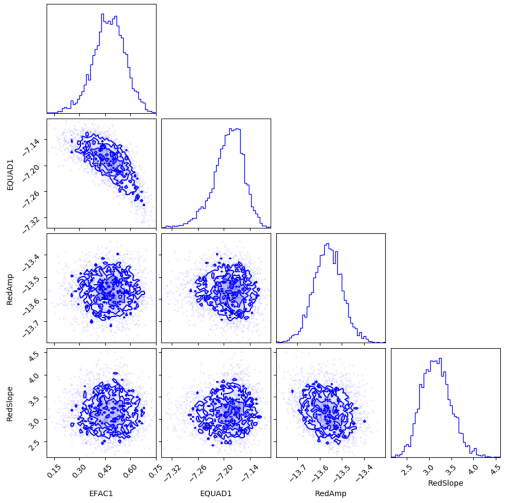

(c) IFA/MTM

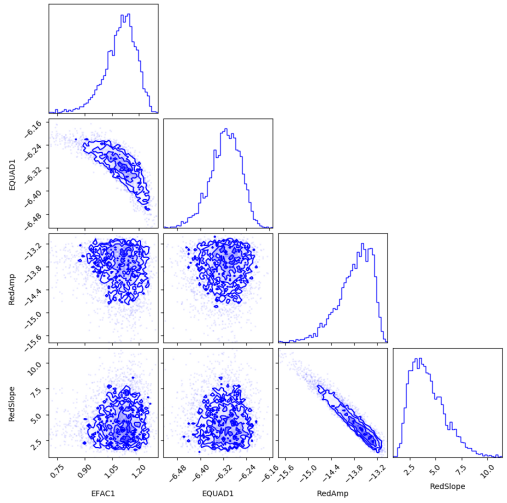

(d) IFA/STM

Figure 3.3: PSR J0437-4715 Corner Plots

3.2 PSR J1022+1001

The second target, and second highest of susceptible pulsars, PSR J1022+1001, has a predicted timing improvement of 282 ns for 1% calibration error through the use of better instrumental calibration [123]. Similar to PSR J0437-4715, this neutron star is a 16.5 ms MSP in a 7.8 day period orbit binary system with a low mass WD companion [19]. Historically, the pulsar has also been known to exhibit poor timing properties [54]. However, van Straten (2013) demonstrated improved post-fit residuals with uncertainty-weighted standard deviation of 880 ns for PSR J1022+1001, two times smaller than conventional methods of instrumental calibration (e.g. IFA) and TOA estimation (e.g. STM), through his use of the METM polarimetric calibration technique and MTM TOA estimation method [123].

Table 3.2

METHOD	wRMSE (μs)	RMSE (μs)	EFAC	EQUAD (μs)	$\log_{10}(A_{\rm red})$	β
METM/MTM	1.294	1.178	0.8(1)	1.1(1)	—	—
METM/STM	1.711	1.647	1.5(1)	1.1(2)	—	—
IFA/MTM	1.309	1.279	0.9(1)	1.1(1)	—	—
IFA/STM	2.015	2.015	1.3(1)	1.5(2)	—	—

Table 3.2: PSR J1022+1001 Timing Noise Statistics for 173 TOAs

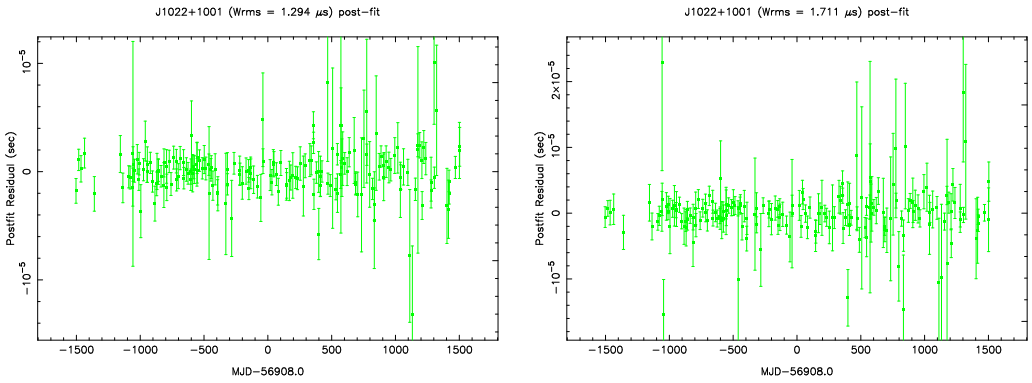

(a) METM/MTM

(b) METM/STM

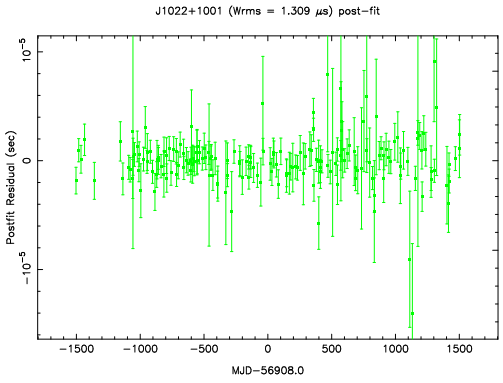

(c) IFA/MTM

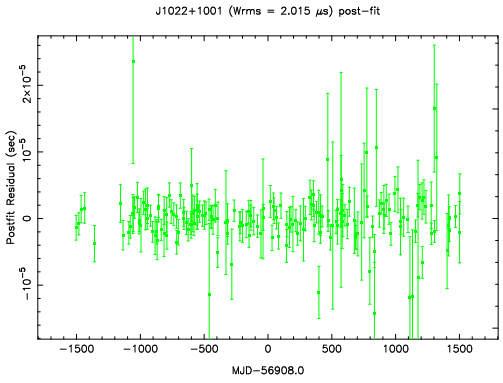

(d) IFA/STM

Figure 3.4: PSR J1022+1001 Post-fit Residuals

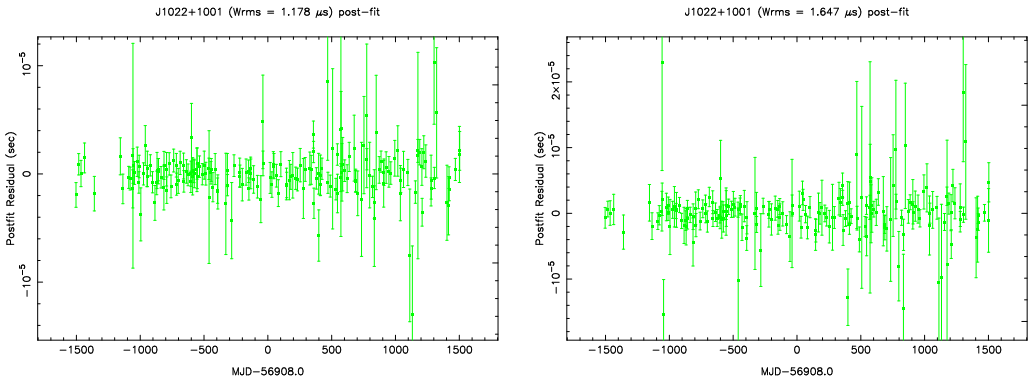

(a) METM/MTM

(b) METM/STM

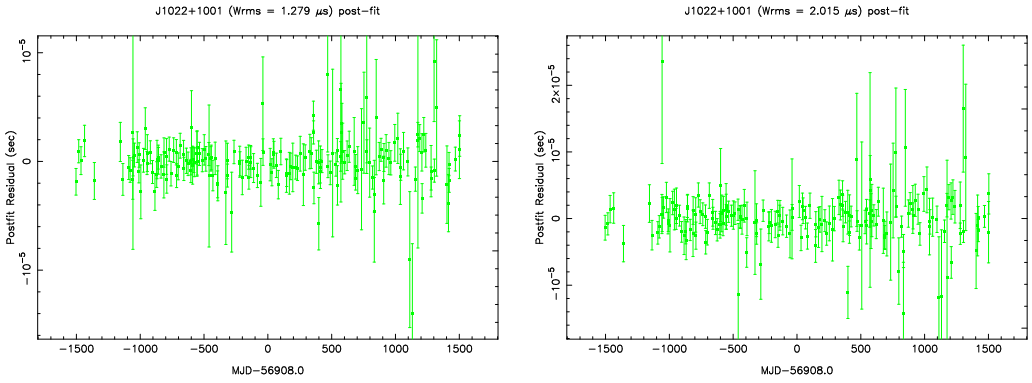

(c) IFA/MTM

(d) IFA/STM

Figure 3.5: PSR J1022+1001 White Noise Residuals

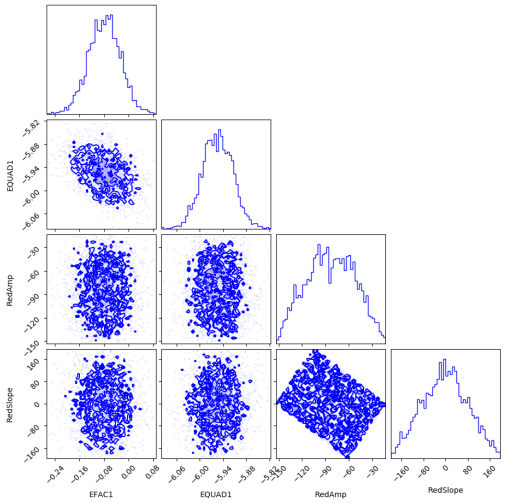

(a) METM/MTM

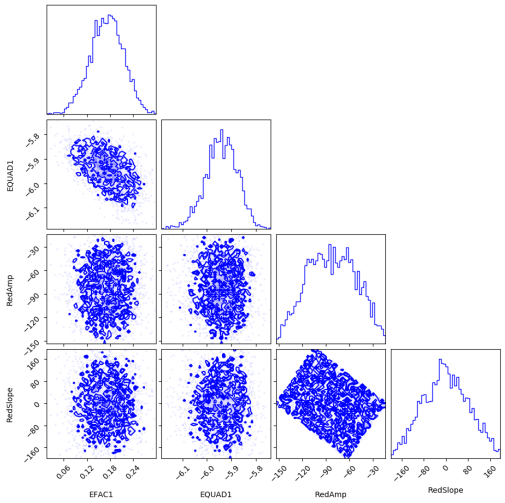

(b) METM/STM

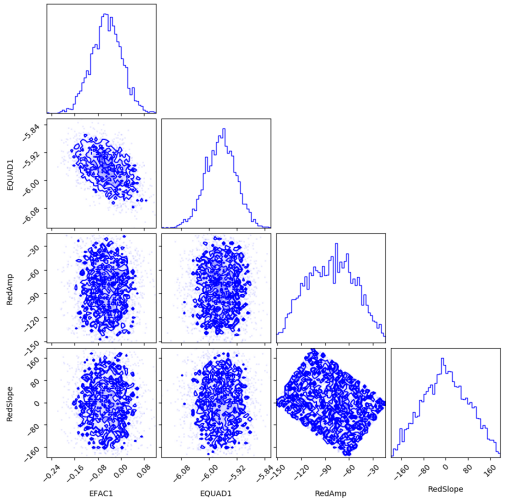

(c) IFA/MTM

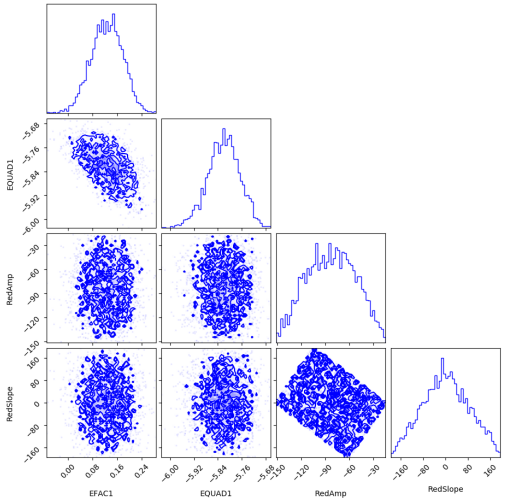

(d) IFA/STM

Figure 3.6: PSR J1022+1001 Corner Plots

3.3 PSR J1045-4509

The binary MSP PSR J1045-4509 has a pulse period of 7.5 ms, is a pulsar with a low mass companion in a 4.1 day orbital period, is located 3.2 kpc from Earth, has a strong mean flux density of 30 mJy at 400-MHz, and is therefore one of the most luminous pulsars [13]. Furthermore, van Straten (2013) predicts that PSR J1045-4509 is the most susceptible to calibration error (388 ns for a 1% calibration error), but is also the noisiest with an RMSE of 2.57 μs (20 times larger than the timing error due to 1% calibration error), suggesting it would take a very large calibration error for METM to have a significant impact [123].

Table 3.3

METHOD	wRMSE (μs)	RMSE (μs)	EFAC	EQUAD (μs)	$\log_{10}(A_{\rm red})$	β
METM/MTM	4.044	1.616	0.6(2)	0.6(6)	-12.4(1)	-2.6(8)
METM/STM	7.442	4.829	0.5(7)	5.4(5)	-12.3(2)	-2.4(9)
IFA/MTM	4.274	1.624	0.7(1)	0.5(5)	-12.3(1)	-2.4(7)
IFA/STM	5.167	4.191	1.1(7)	4(1)	-12.2(1)	-1.5(9)

Table 3.3: PSR J1045-4509 Timing Noise Statistics for 137 TOAs

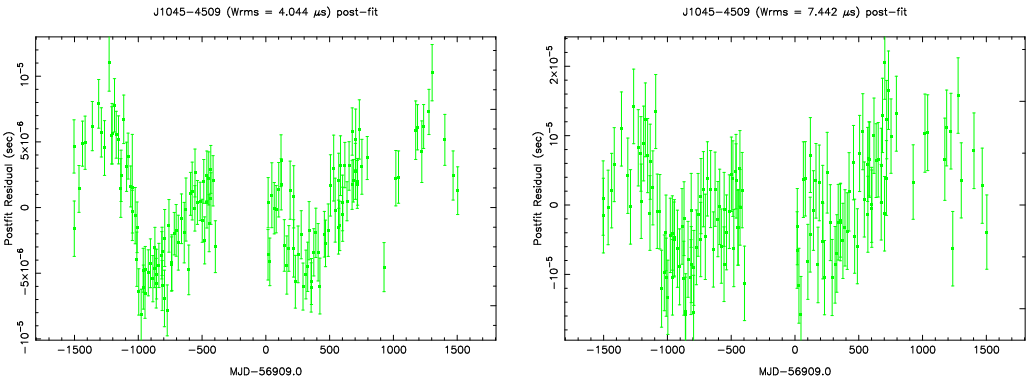

(a) METM/MTM

(b) METM/STM

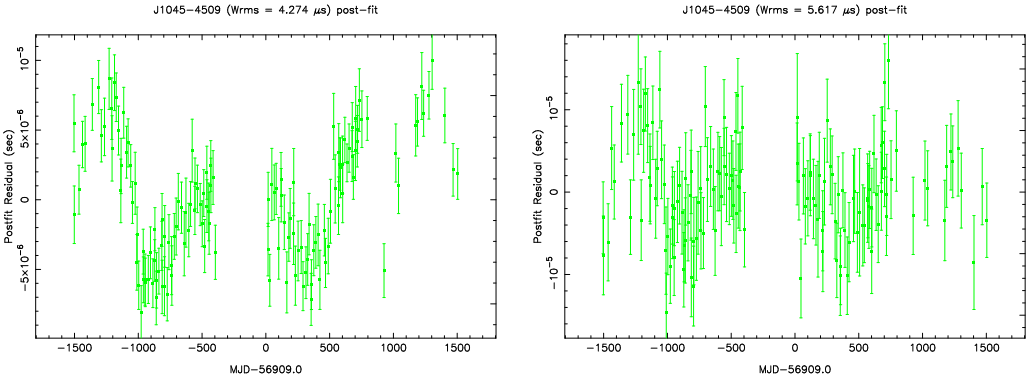

(c) IFA/MTM

(d) IFA/STM

Figure 3.7: PSR J1045-4509 Post-fit Residuals

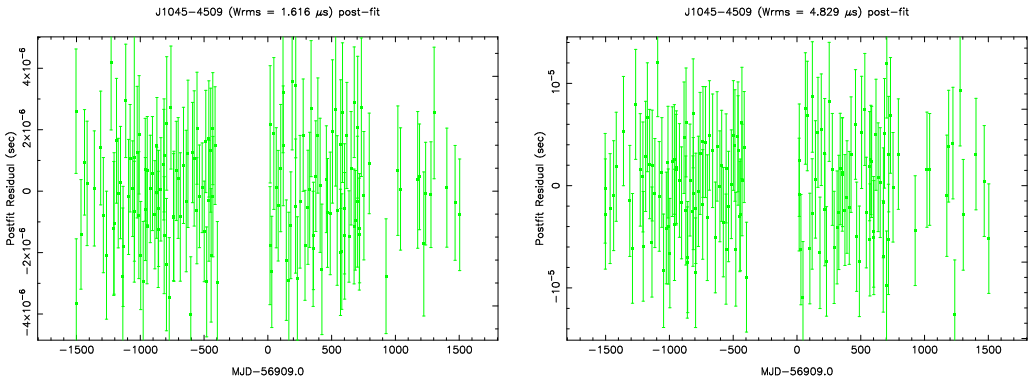

(a) METM/MTM

(b) METM/STM

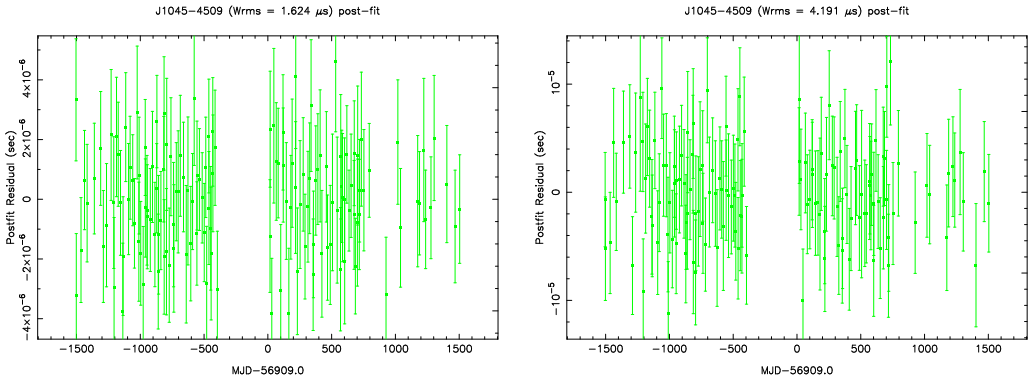

(c) IFA/MTM

(d) IFA/STM

Figure 3.8: PSR J1045-4509 White Noise Residuals

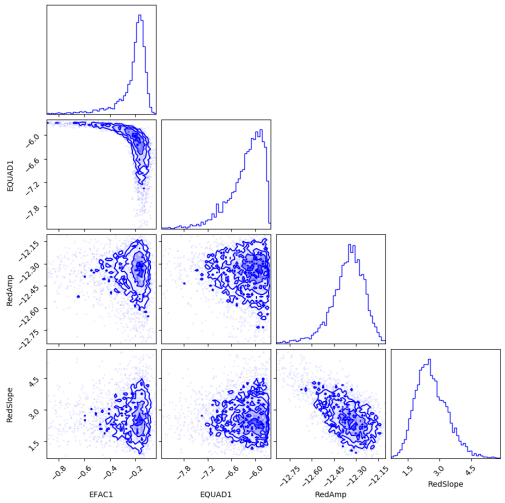

(a) METM/MTM

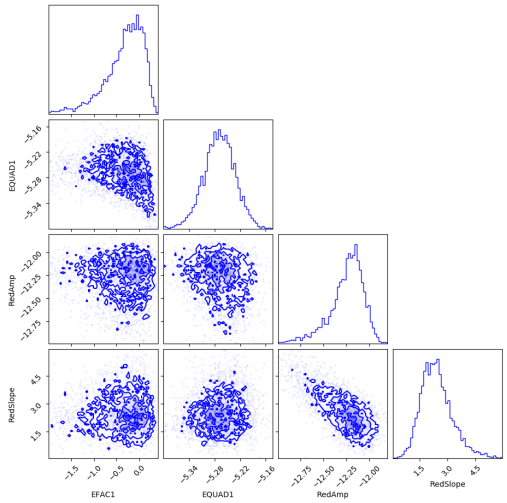

(b) METM/STM

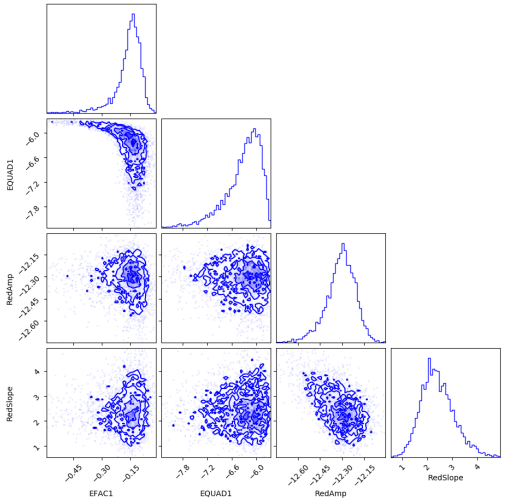

(c) IFA/MTM

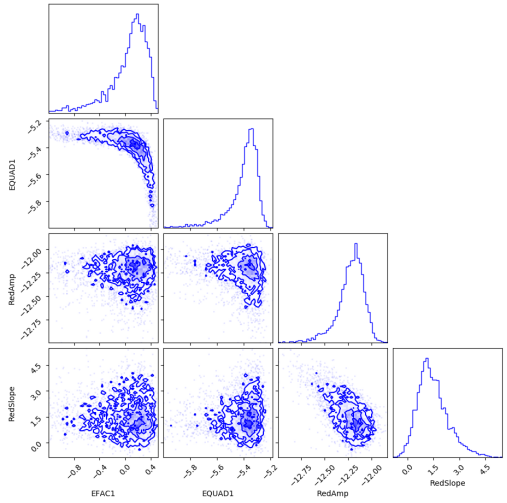

(d) IFA/STM

Figure 3.9: PSR J1045-4509 Corner Plots

3.4 PSR J1600-3053

PSR J1600-3053 is both dim and distant from Earth with a relatively low flux density of 3.2 mJy at 20-cm wavelengths. However, Ord et al. (2016) were capable of achieving sub-millisecond timing residuals for this pulsar after finding a very narrow feature in its pulse profile through coherent de-dispersion [86]. PSR J1600-3053 is also a 3.6 ms pulsar in a binary system with a 14.3 day orbital period. An 115 ns error in TOA estimation is predicted (for a 1% calibration error for this pulsar) by van Straten (2013) [123].

Table 3.4

METHOD	wRMSE (μs)	RMSE (μs)	EFAC	EQUAD (μs)	$\log_{10}(A_{\rm red})$	β
METM/MTM	1.160	0.295	0.7(2)	0.1(1)	-13.3(2)	-2.54
METM/STM	1.321	0.485	0.8(5)	0.4(1)	—	—
IFA/MTM	1.391	0.300	0.8(2)	0.1(1)	-13.4(2)	-2.76
IFA/STM	1.411	0.349	1.1(5)	0.2(2)	—	—

Table 3.4: PSR J1600-3053 Timing Noise Statistics for 141 TOAs

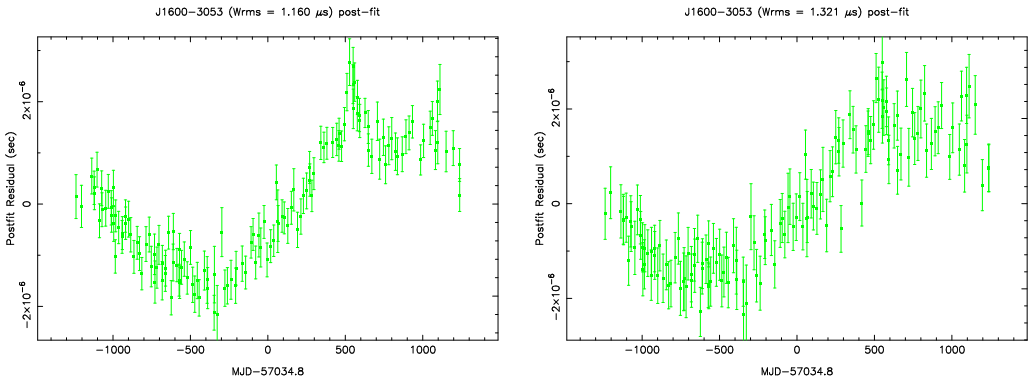

(a) METM/MTM

(b) METM/STM

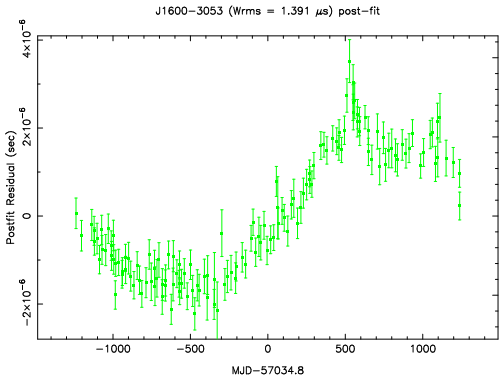

(c) IFA/MTM

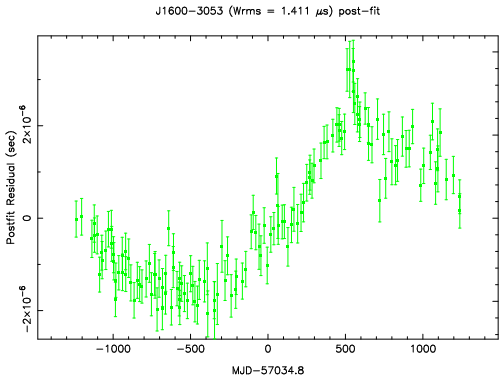

(d) IFA/STM

Figure 3.10: PSR J1600-3053 Post-fit Residuals

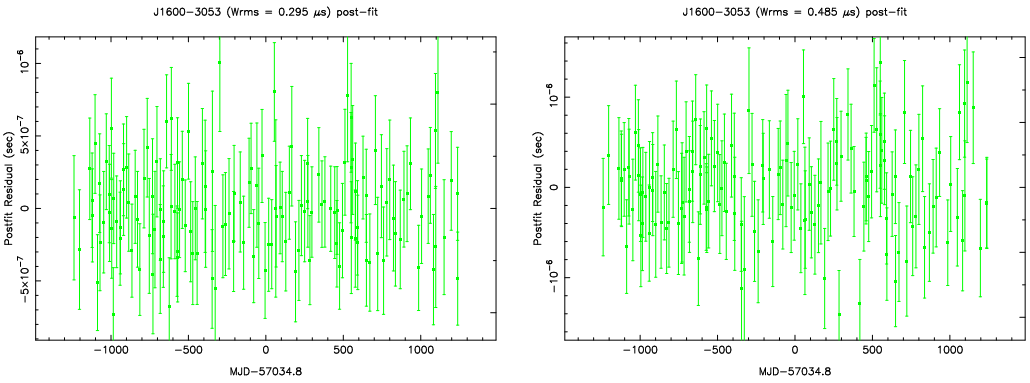

(a) METM/MTM

(b) METM/STM

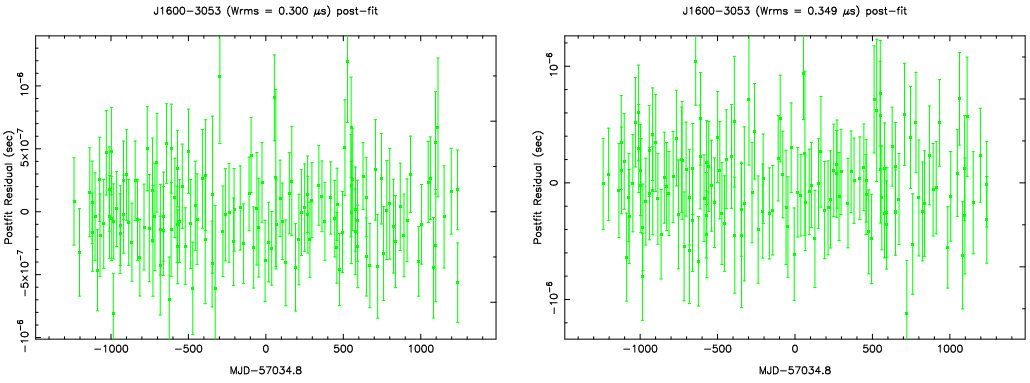

(c) IFA/MTM

(d) IFA/STM

Figure 3.11: PSR J1600-3053 White Noise Residuals

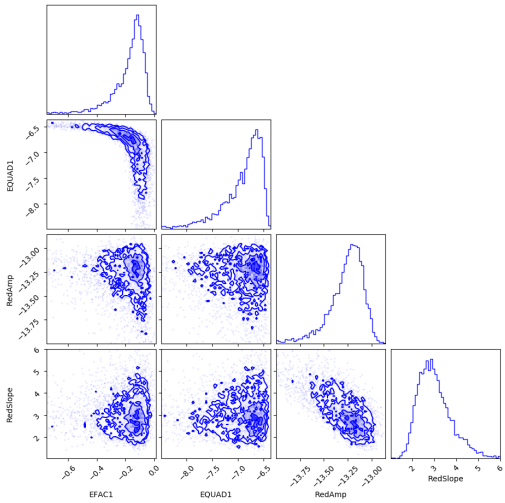

(a) METM/MTM

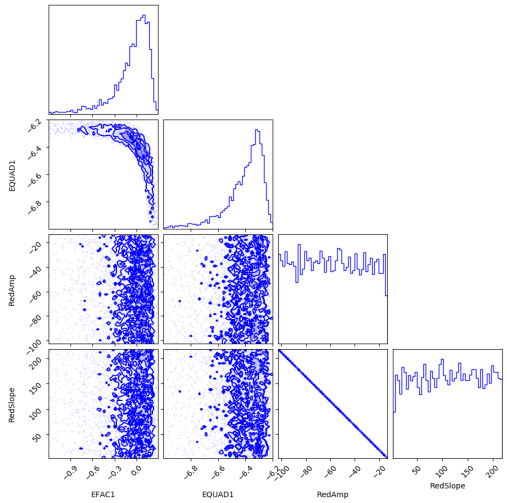

(b) METM/STM

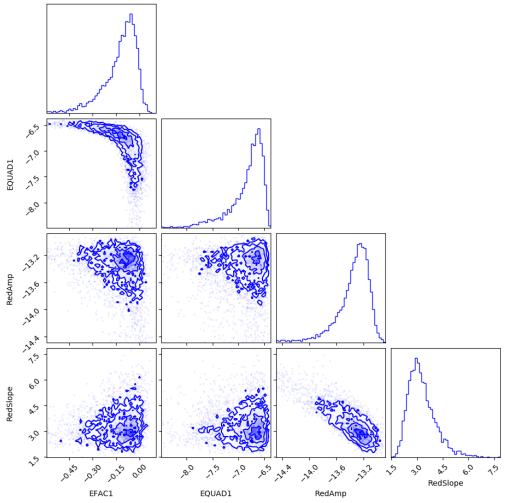

(c) IFA/MTM

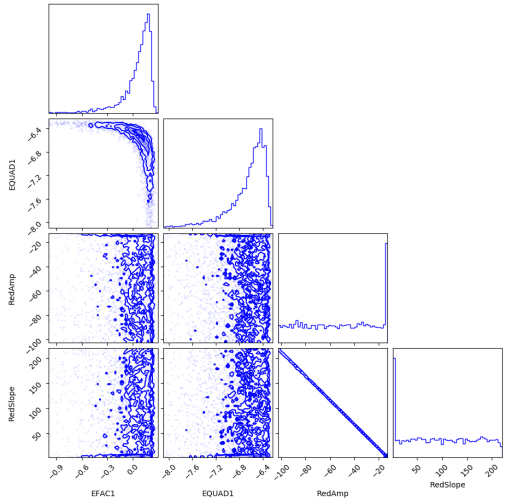

(d) IFA/STM

Figure 3.12: PSR J1600-3053 Corner Plots

3.5 PSR J1643-1224

PSR J1643-1224 is a luminous pulsar with a 4.6 ms rotational period, in a circular binary orbit of 147 days, with a low mass companion between 0.1-0.3 $M_{\odot}$, at least 5 kpc from Earth [72]. The low eccentricity of this pulsar results in a covariant longitude and epoch [128] causing PSR J1643-1224 to exhibit long-term rotational variability (i.e. the pulse profile exhibits changes over long time scales) [8]. This effect, intrinsic to the pulsar, could also be detrimental to the accuracy of pulsar timing analysis [128]. PSR J1643-1224 is predicted to have a 266 ns timing error to 1% instrumental calibration error, the third highest pulsar susceptibility predicted in van Straten (2013) [123].

Table 3.5

METHOD	wRMSE (μs)	RMSE (μs)	EFAC	EQUAD (μs)	$\log_{10}(A_{\rm red})$	β
METM/MTM	1.985	0.600	0.4(4)	0.4(3)	-12.60(7)	-1.7(3)
METM/STM	2.197	1.041	1.2(4)	0.5(4)	-12.43(7)	-1.2(4)
IFA/MTM	1.999	0.642	0.5(4)	0.4(3)	-12.64(8)	-1.8(3)
IFA/STM	2.250	1.075	1.0(6)	0.8(4)	-12.45(7)	-1.3(4)

Table 3.5: PSR J1643-1224 Timing Noise Statistics for 143 TOAs

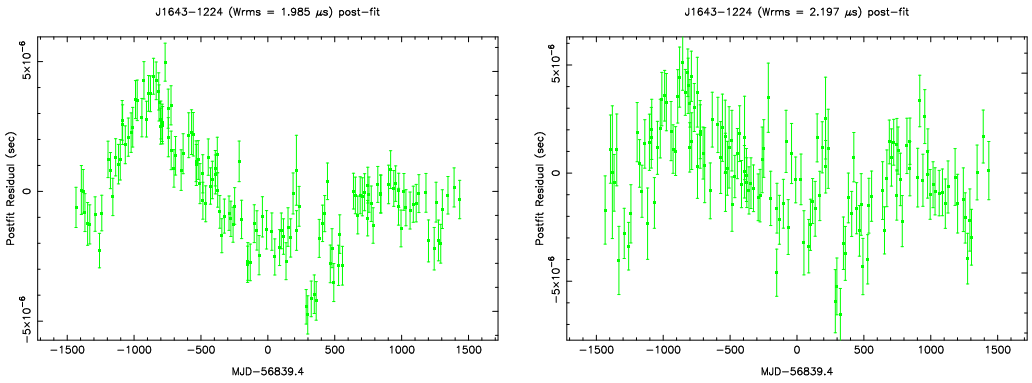

(a) METM/MTM

(b) METM/STM

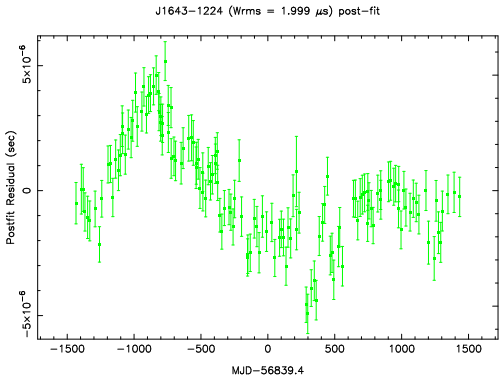

(c) IFA/MTM

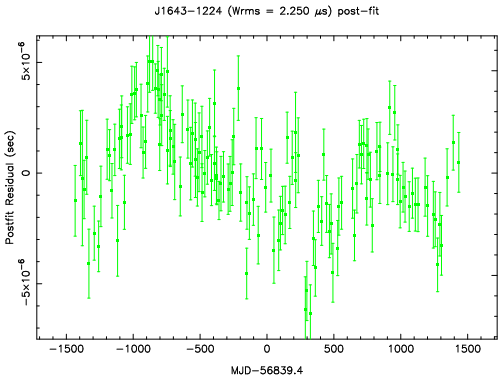

(d) IFA/STM

Figure 3.13: PSR J1643-1224 Post-fit Residuals

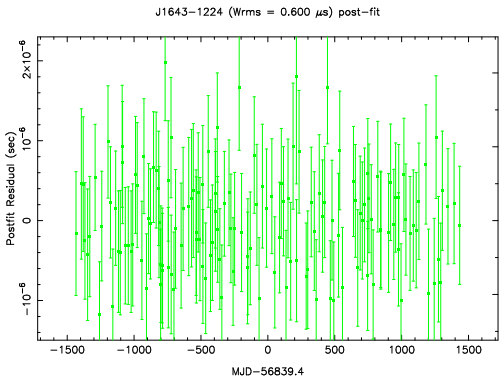

(a) METM/MTM

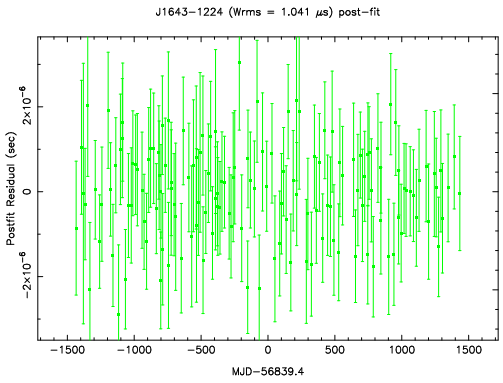

(b) METM/STM

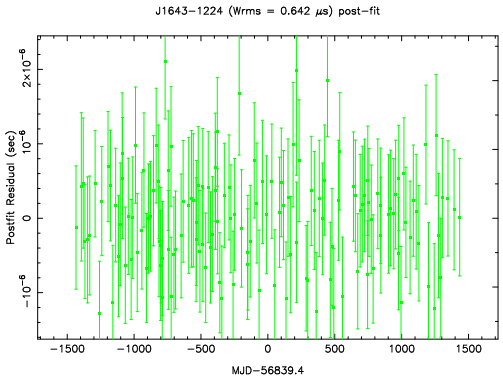

(c) IFA/MTM

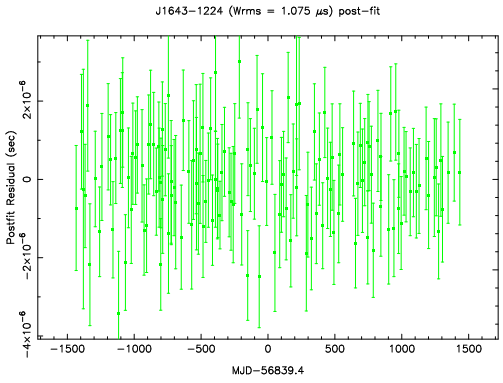

(d) IFA/STM

Figure 3.14: PSR J1643-1224 White Noise Residuals

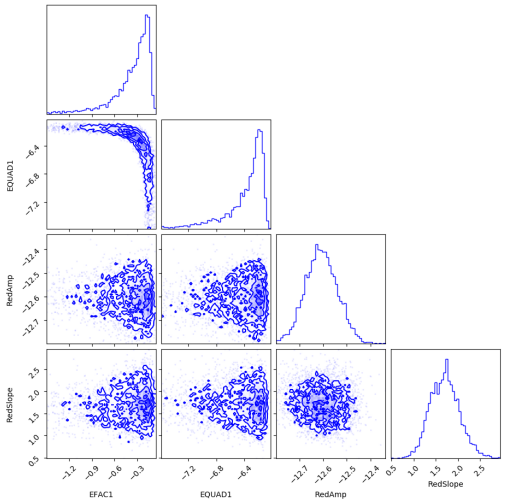

(a) METM/MTM

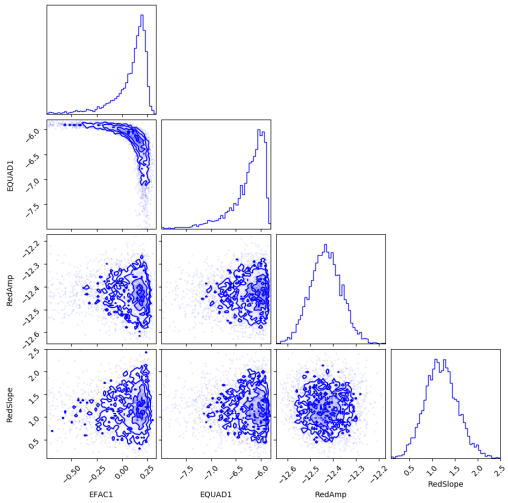

(b) METM/STM

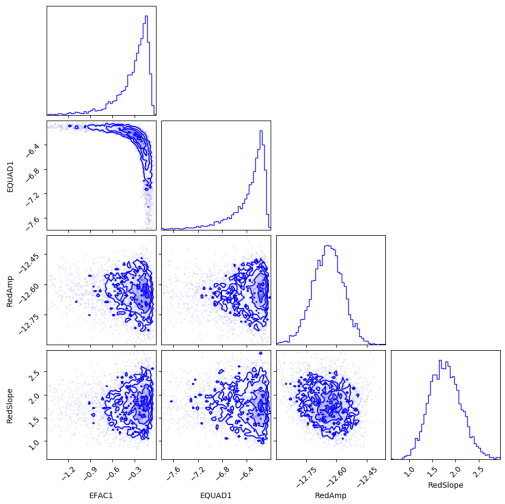

(c) IFA/MTM

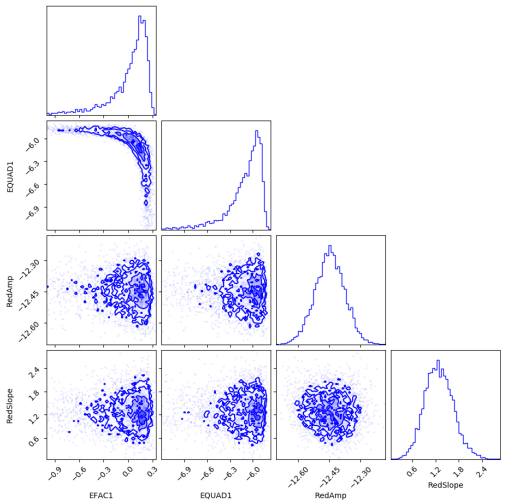

(d) IFA/STM

Figure 3.15: PSR J1643-1224 Corner Plots

Chapter 4

Conclusions

We have taken the novel approach of incorporating state-of-the-art pulsar timing tools into one pulsar calibration pipeline, PSRPL, and applied this improved methodology on a sample of MSPs predicted by van Straten (2013) to be the most susceptible to calibration error [123]. We have performed this analysis and compared the results across four models: (i) calibration via METM followed by MTM for predicting TOA estimates, and similarly, (ii) METM/STM, (iii) IFA/MTM, and (iv) IFA/STM. For each pulsar in our sample, we have shown that METM and MTM yield arrival times with the highest precision and accuracy (e.g. the least white noise and red noise), and should be incorporated in TOA analyses over conventional methods for obtaining high-precision, high-fidelity TOA measurements.

4.1 Discussion

For PSR J0437-4715, we have calibrated 8.169 years of 20-cm CASPSR data from Parkes using PSRPL to produce a total of 340 TOA estimates. It is important to note, that the reduced χ^2/N parameter is no longer a meaningful statistic for model comparison, as TEMPONEST is effectively pushing this value towards unity, by tweaking the EFAC and EQUAD parameters. Large values of EFAC mean that TEMPONEST has determined that the error bars on TOAs are underestimated [67], which is apparent for PSR J0437-4715 (see Table §**3.1**), where TEMPONEST has determined these error bars should be approximately 9 and 13 times larger than estimated for METM and IFA models respectively. Therefore, EFAC shows that MTM does a much better job of estimating the uncertainty in TOAs. Such additional noise is typically attributed to pulse jitter. However, pulse jitter should equally impact MTM because jitter is intrinsic to the pulsar and not modelled by MTM. Of the MTM-derived TOAs, the combination of METM and MTM algorithms appears to produce the best uncertainty estimates. IFA/STM is the worst-case scenario (see Figure §**3.2**) and therefore our baseline for model comparison with a white noise TOA residual RMSE of 589 ns. The METM/STM model (149 ns) indicates that METM has corrected systematic distortions to the total intensity profile which has reduced the noise by about 75% from IFA/STM. METM/MTM (66 ns) shows that MTM is able to further reduce the noise by another 56%, better

than the 15% improvement predicted in column 3 of Table 1 in van Straten (2006) or column 2 of Table 1 in van Straten (2013). It could be that MTM is also mopping up residual calibration errors. IFA/MTM (68 ns) is also showing that MTM is capable of performing well and mopping up any calibration errors in IFA-calibrated data, performing 88% better than STM for the IFA-derived models. Additionally, the corner plots (see Figure §**3.3**) show the correlation, if any, between white noise (i.e. EFAC and EQUAD) and red noise (i.e. $A_{\rm red}$ and β) parameters which are determined for each model via TEMPONEST. Here we see a strong anti-correlation between the white noise parameters EFAC and EQUAD, where as EFAC increases, EQUAD decreases, and vice versa. For STM-derived solutions, TEMPONEST has also determined a correlation between the red noise parameters $A_{\rm red}$ and β. However, this correlation is not clearly present in the MTM-derived TOA solutions.

From the 8.229 years of 20-cm CASPSR data, 173 TOA estimates were produced through PSRPL for PSR J1022+1001. Our results show IFA/STM to be our baseline model for comparison with a white noise TOA residual RMSE of 2.015 μs (see Figure §**3.5**). METM/STM (1.647 μs) has reduced the noise by 18%. IFA/MTM (1.279 μs) has improved upon IFA/STM by 36.5%. METM/MTM has produced the best white noise RMSE of 1.178 μs, 28.5% better than METM/STM, and although less than the predicted 32% improvement by van Straten (2013), has performed 8%

better than IFA/MTM. This may be explained by the fact that the 400 MHz bandwidth of our CASPSR data is more than 6 times larger than that of the two 64-MHz CPSR2 bands analysed by van Straten (2013) [123]. PSR J1022+1001 is known to exhibit strong variations in profile shape as a function of radio frequency [29] and, when coupled with interstellar scintillation, these spectral variations translate into temporal variations of the average pulse profile formed by integrating over all frequencies (e.g. Ramachandran & Kramer 2003 [96]). Dividing the 400-MHz CASPSR band into sub-bands and/or employing frequency-dependent template matching methods (e.g. Pennucci 2019 [92]) may improve the results for PSR J1022+1001 in future work. As indicated by the rectangular uniform distribution of RedAmp versus RedSlope in Figure 3.6, our data fail to constrain $A_{\rm red}$ and β for all models, even after searching over many orders of magnitude (see Figure §**3.6**). It is important to note here that we varied the orthometric amplitude (H3) and ratio (STIG) parameters in TEMPO2 only for the MTM-derived TOA data and then held these values fixed at the best-fit MTM-derived solutions when analysing STM data.

In the cases of PSR J1045-4509 and J1600-3053, we find that METM/STM produces the worst case scenarios of white noise TOA residuals with an RMSE of 4.829 μs and 485 ns respectively. In the case of PSR J1045-4509, approximately a years worth of data is missing around 56500-56900 MJD for this MSP, which could affect the ability to accurately determine the red

noise signal from the data. For PSR J1600-3053, the corner plots of the STM-derived TOAs presented in Figure §**3.12** appear to indicate that the red noise parameters are not constrained by the data. Therefore, these values are not reported in Table §**3.4**. The fact that the red noise parameters are constrained in the MTM-derived TOAs leads us to suspect that the STM-derived TOAs may be contaminated by one or more outliers that must be identified and excised after developing an objective method for doing so in future work. However, the METM/MTM-derived white noise TOA residuals are the best for both pulsars with RMSE of 1.616 μs for PSR J1045-4509 and 295 ns for PSR J1600-3053. METM/MTM has performed 66.5% and 39% better than METM/STM in both cases respectively, better than the respective 12% and 10% improvements predicted by van Straten (2013).

The final pulsar in our sample of MSPs, PSR J1643-1224, has shown a strong relationship between EFAC and EQUAD, and between $A_{\rm red}$ and β (see Figure §**3.15**). IFA/STM is the baseline model with a white noise RMSE of 1.075 μs. METM/STM yields a white noise RMSE of 1.041 μs for a 3% improvement. IFA/MTM (642 ns) has improved upon IFA/STM by 40%. The METM/MTM-derived solutions (600 ns) are 42% better than METM/STM, and 6.5% better than IFA/MTM. This is a large improvement compared to the predicted improvement of 9% for 1% calibration error by van Straten (2013). METM has corrected systematic

timing distortions of the total intensity profile for all the pulsars in the sample, where MTM has also mopped up any residual calibration errors.

For two pulsars in our sample (PSR J0437-4715 and PSR J1643-1224), MTM has marginally decreased the red noise in the timing residuals. For the METM-calibrated data of PSR J0437-4715 and for both METM- and IFA-calibrated data of PSR J1643-1224, the MTM-derived TOAs have a red noise amplitude that is smaller than that of the STM-derived TOAs (by about 1 standard deviation). In both cases, the exponent on the power-law relation that is used to model the red noise is also smaller, but this is not statistically significant.

We have shown that utilising METM for instrumental calibration, followed by MTM produces the best TOA estimates, yielding a significant reduction in noise which should, in principle, increase experimental sensitivity. With increased sensitivity, one may estimate new model parameters that were previously unattainable in a pulsar system, such as the Shapiro delay measured for PSR J1022+1001 by van Straten (2013) [123]. Furthermore, we notice that for each pulsar in our sample, data calibrated using IFA followed by MTM can produce TOAs nearly as good as those derived from the METM calibrations.

4.2 Future Work

The results presented in this paper report on our analysis undertaken using the 20-cm band CASPSR dataset from Parkes. In future, we could expand the scope of this analysis to apply PSRPL to different PPTA data and instruments, such as the historical datasets taken with the Parkes Digital Filter Bank (PDFB) to test for increased sensitivity due to better instrumental calibration methods. The PDFB shows evidence of non-linear response that introduces around 5% to 10% over-polarization that cannot be calibrated using MEM. By extending PSRPL with new model parameters that describe non-linear instrumental response (to first order), we may be able to better understand this by studying it in more detail. Similarly, PSRPL can be applied to new data from observations taken with the Parkes Ultra Wide-bandwidth Low (UWL) receiver [47]. Instrumental calibration via METM should also be applied to different telescopes internationally.

The METM instrumental calibration method used throughout this research produces a 1-Dimensional mean pulse profile template based on the polarization of the signal [123]. A 2-Dimensional method has been developed by Pennucci (2019), which includes: (i) a frequency-dependent rotation to account for DM variability averaging bandwidth, (ii) using Principle Component Analysis to find a reduced basis in which to quantify

spectral variation of the mean pulse profile, (iii) selecting eigenvector profiles based on signal-to-noise, to indicate the number of orthogonal elements (in addition to the mean pulse profile) needed to capture the profile evolution, (iv) wavelet smoothing the mean and eigenvector profiles to produce smooth, high-fidelity templates, and (v) using B-splines to interpolate the frequency evolution of projected coordinate coefficients used in the linear combinations of eigenprofiles. Pennucci's template matching method is able to model the profile variations in the frequency domain while simultaneously measuring the DM variation and phase shift of the observation [92]. We propose combining this method with MTM to create something that models the: (i) variation of pulse shape with frequency, (ii) differential DM at epoch, and (iii) possible residual calibration errors that vary with frequency by modelling all four Stokes parameters.

Another interesting area of investigation would be to test and determine the optimal method for RFI mitigation as RFI is an ongoing problem in radio astronomy through the overuse of the radio spectrum by the communications industry; to date, no ideal method has been determined. For the analysis reported in this thesis, PSRPL utilised the COASTGUARD algorithm [65] for RFI excision. We propose the integration of multiple RFI mitigation packages and employing different combinations of them through different versions of the PSRPL pipeline to determine the optimal one.

Finally, we come back to our ultimate goal of the thesis, which was to increase the sensitivity of PTAs to low frequency (nHz) gravitational waves. We have shown that improved high-fidelity, high-precision pulsar timing through better instrumental calibration (for a small sample of MSPs predicted to be the most susceptible to polarimetric calibration errors) achieves better precision than predicted by van Straten (2013). The next step is to then develop this finding to see if we have increased sensitivity to such an extent that we can place more stringent constraints on the stochastic GWB.

GLOSSARY

ACRONYM	Words
aLIGO	advanced LIGO
ARC	Australian Research Council
ATNF	Australian Telescope National Facility
BH	Black Hole
CASPER	Collaboration for Astronomy Signal Processing and Electronics Research
CASPSR	CASPER-Parkes-Swinburne Recorder
CPSR-II	Caltech-Parkes-Swinburne Recorder (Gen. II)
CSIRO	Commonwealth Scientific and Industrial Research Organisation
DM	Dispersion Measure
EFAC	Scalar Multiplicative Error Correction Factor
EHT	Event Horizon Telescope
EQUAD	Quadrature-added Error

ACRONYM	Words
eLISA	evolved LISA
EM	Electromagnetic
EPTA	European Pulsar Timing Array
ESA	European Space Agency
FITS	Flexible Image Transport System
GR	General Relativity
GW	Gravitational Wave
GWB	Gravitational Wave Background
H-R	Hertzsprung-Russell
iLIGO	inital LIGO
IFA	Ideal Feed Assumption
IPTA	International Pulsar Timing Array
ISM	Interstellar Medium
LIGO	Laser Interferometer GW Observatory
LISA	Laser Interferometer Space Antenna
MEM	Measurement Equation Matching
METM	Measurement Equation Template Matching
MSP	Millisecond Pulsar
MTM	Matrix Template Matching
NANOgrav	North American Nanohertz Observatory for GWs
NASA	National Aeronautics and Space Administration

ACRONYM	Words
NS	Neutron Star
OzGRAV	ARC Centre of Excellence in GW Discovery
PBS	Portable Batch System
PDFB	Parkes Digital Filter Bank
PK	Post-Keplarian
PPN	Parameterized Post-Newtonian
PSR	Pulsar
PSRPL	Pulsar Calibration Pipeline
RMSE	Root Mean Squared Error
SMBH	Supermassive Black Hole
STM	Scalar Template Matching
TOA	Time-of-arrival
UWL	Ultra Wide-bandwidth Low-frequency
WD	White Dwarf
wRMSE	Weighted Root Mean Squared Error

Bibliography

[1] B. P. Abbott et al. "Binary Black Hole Mergers in the First Advanced LIGO Observing Run". In: *Physical Review X* 6.4, 041015 (Oct. 2016), p. 041015. DOI: 10.1103/PhysRevX.6.041015. arXiv: 1606.04856 [gr-qc].

[2] B. P. Abbott et al. "GW151226: Observation of Gravitational Waves from a 22-Solar-Mass Binary Black Hole Coalescence". In: *Physical Review Letters* 116.24, 241103 (June 2016), p. 241103. DOI: 10.1103/PhysRevLett.116.241103. arXiv: 1606.04855 [gr-qc].

[3] B. P. Abbott et al. "GW170817: Observation of Gravitational Waves from a Binary Neutron Star Inspiral". In: *Physical Review Letters* 119.16, 161101 (Oct. 2017), p. 161101. DOI: 10.1103/PhysRevLett.119.161101. arXiv: 1710.05832 [gr-qc].

[4] B. P. Abbott et al. "GWTC-1: A Gravitational-Wave Transient Catalog of Compact Binary Mergers Observed by LIGO and Virgo during the First and Second Observing Runs". In: *Physical Review X*

9.3, 031040 (July 2019), p. 031040. DOI: 10.1103/PhysRevX.9.031040. arXiv: 1811.12907 [astro-ph.HE].

[5] B. P. Abbott et al. "Multi-messenger Observations of a Binary Neutron Star Merger". In: *Astrophysical Journal, Letters* 848.2, L12 (Oct. 2017), p. L12. DOI: 10.3847/2041-8213/aa91c9. arXiv: 1710.05833 [astro-ph.HE].

[6] B. P. Abbott et al. "Observation of Gravitational Waves from a Binary Black Hole Merger". In: *Physical Review Letters* 116.6, 061102 (Feb. 2016), p. 061102. DOI: 10.1103/PhysRevLett.116.061102. arXiv: 1602.03837 [gr-qc].

[7] *About Parkes radio telescope*. URL: https://www.csiro.au/en/Research/Facilities/ATNF/Parkes-radio-telescope/About-Parkes.

[8] Z. Arzoumanian et al. "The NANOGrav 11 Year Data Set: Pulsar-timing Constraints on the Stochastic Gravitational-wave Background". In: *Astrophysical Journal* 859.1, 47 (May 2018), p. 47. DOI: 10.3847/1538-4357/aabd3b. arXiv: 1801.02617 [astro-ph.HE].

[9] Z. Arzoumanian et al. "The NANOGrav Nine-year Data Set: Limits on the Isotropic Stochastic Gravitational Wave Background". In: *Astrophysical Journal* 821.1, 13 (Apr. 2016), p. 13. DOI: 10.3847/0004-637X/821/1/13. arXiv: 1508.03024 [astro-ph.GA].

[10] W. Baade and F. Zwicky. "Cosmic Rays from Super-novae". In: *Proceedings of the National Academy of Science* 20.5 (May 1934), pp. 259–263. DOI: 10.1073/pnas.20.5.259.

[11] D. C. Backer, S. R. Kulkarni, C. Heiles, M. M. Davis, and W. M. Goss. "A millisecond pulsar". In: *Nature* 300.5893 (Dec. 1982), pp. 615–618. DOI: 10.1038/300615a0.

[12] M. Bailes. "The art of precision pulsar timing". In: *Relativity in Fundamental Astronomy: Dynamics, Reference Frames, and Data Analysis*. Ed. by Sergei A. Klioner, P. K. Seidelmann, and Michael H. Soffel. Vol. 261. IAU Symposium. Jan. 2010, pp. 212–217. DOI: 10.1017/S1743921309990421.

[13] M. Bailes et al. "Discovery of three binary millisecond pulsars". In: *The Astrophysical Journal* 425 (1994). DOI: 10.1086/187306.

[14] B. Bertotti, L. Iess, and P. Tortora. "A test of general relativity using radio links with the Cassini spacecraft". In: *Nature* 425.6956 (Sept. 2003), pp. 374–376. DOI: 10.1038/nature01997.

[15] M. C. Britton. "Radio Astronomical Polarimetry and the Lorentz Group". In: *The Astrophysical Journal Letters* 532 (2000), pp. 1240–1244. DOI: 10.1086/308595.

[16] M. C. Britton. "Radio Astronomical Polarimetry and the Lorentz Group". In: *The Astrophysical Journal* 532.2 (Apr. 2000), pp. 1240–1244. DOI: 10.1086/308595.

[17] M. C. Britton, W. van Straten, M. Bailes, M. Toscano, and R. N. Manchester. "High Precision Timing of PSR J0437-4715". In: *IAU Colloq. 177: Pulsar Astronomy - 2000 and Beyond*. Ed. by M. Kramer, N. Wex, and R. Weilebinski. Vol. 202. Astronomical Society of the Pacific Conference Series. 2000, p. 73.

[18] M. Burgay et al. "The Highly Relativistic Binary Pulsar PSR J0737-3039A: Discovery and Implications". In: *Binary Radio Pulsars*. Ed. by Fred A. Rasio and Ingrid H. Stairs. Vol. 328. Astronomical Society of the Pacific Conference Series. July 2005, p. 53. arXiv: astro-ph/0405194 [astro-ph].

[19] F. Camilo, D. J. Nice, J. A. Shrauner, and J. H. Taylor. "Princeton Arecibo Declination Strip Survey for Millisecond Pulsars". In: *The Astrophysical Journal* 469 (1996), p. 819. DOI: 10.1086/177829.

[20] C. Caprini et al. "Science with the space-based interferometer eLISA. II: gravitational waves from cosmological phase transitions". In: *Journal of Cosmology and Astroparticle Physics* 2016.4, 001 (Apr. 2016), p. 001. DOI: 10.1088/1475-7516/2016/04/001. arXiv: 1512.06239 [astro-ph.CO].

[21] *Centre for Astrophysics and Supercomputing*. URL: https://astronomy.swin.edu.au/supercomputing/.

[22] S. Chandrasekhar. "The Maximum Mass of Ideal White Dwarfs". In: *Astrophysical Journal* 74 (July 1931), p. 81. DOI: 10.1086/143324.

[23] S. Chandrasekhar. "The transfer of radiation in stellar atmospheres". In: *Bulletin of the American Mathematical Society* 53(7) (), 641–712. DOI: 10.1090/s0002-9904-1947-08825-x.

[24] K. Chen and M. Ruderman. "Pulsar Death Lines and Death Valley". In: *Astrophysical Journal* 402 (Jan. 1993), p. 264. DOI: 10.1086/172129.

[25] T. Chow. *Gravity, black holes, and the very early universe: an introduction to general relativity and cosmology*. Springer, 2008.

[26] J. Condon and S. M. Ransom. *Essential radio astronomy*. Princeton University Press, 2016.

[27] N. Copernicus. *De revolutionibus orbium coelestium*. Nicolaus Copernicus, 1543.

[28] H. T. Cromartie et al. "Relativistic Shapiro delay measurements of an extremely massive millisecond pulsar". In: *Nature Astronomy* 4(1) (2019), 72–76. DOI: 10.1038/s41550-019-0880-2.

[29] S. Dai et al. "A study of multifrequency polarization pulse profiles of millisecond pulsars". In: *Monthly Notices of the Royal Astronomical Society* 449 (2015), 3223–3262. DOI: 10.1093/mnras/stv508.

[30] P. B. Demorest, T. Pennucci, S. M. Ransom, M. S. E. Roberts, and J. W. T. Hessels. "A two-solar-mass neutron star measured using Shapiro delay". In: *Nature* 467.7319 (Oct. 2010), pp. 1081–1083. DOI: 10.1038/nature09466. arXiv: 1010.5788 [astro-ph.HE].

[31] A. Dunning, M. Bowen, M. Bourne, D. Hayman, and S. L. Smith. "An ultra-wideband dielectrically loaded quad-ridged feed horn for radio astronomy". In: *IEEE-APS Topical Conference on Antennas and Propagation in Wireless Communications (APWC)* (2015). DOI: 10.1109/apwc.2015.7300180.

[32] A. S. Eddington. *The mathematical theory of relativity*. Cambridge University Press, 1924.

[33] R. T. Edwards, G. B. Hobbs, and R. N. Manchester. "TEMPO2, a new pulsar timing package - II. The timing model and precision estimates". In: *Monthly Notices of the RAS* 372.4 (Nov. 2006), pp. 1549–1574. DOI: 10.1111/j.1365-2966.2006.10870.x. arXiv: astro-ph/0607664 [astro-ph].

[34] A. Einstein. "Die Grundlage der allgemeinen Relativitätstheorie". In: *Annalen der Physik* 354.7 (Jan. 1916), pp. 769–822. DOI: 10.1002/andp.19163540702.

[35] *Faraday effect*. URL: https://en.wikipedia.org/wiki/Faraday_effect#/media/File:Faraday-effect.svg.

[36] F. Feroz, M. P. Hobson, and M. Bridges. "MultiNest: an efficient and robust Bayesian inference tool for cosmology and particle physics". In: *Monthly Notices of the Royal Astronomical Society* 398(4) (2009), 1601–1614. DOI: 10.1111/j.1365-2966.2009.14548.x.

[37] R. S. Foster and D. C. Backer. "Constructing a Pulsar Timing Array". In: *Astrophysical Journal* 361 (Sept. 1990), p. 300. DOI: 10.1086/169195.

[38] B. M. Gaensler and P. O. Slane. "The Evolution and Structure of Pulsar Wind Nebulae". In: *Annual Review of Astronomy and Astrophysics* 44(1) (2006), pp. 17–47. DOI: 10.1146/annurev.astro.44.051905.092528.

[39] G. Galilei. *Sidereus nuncius magna, longeque admirabilia spectacula pandens lunae facie, fixis innumeris, lacteo circulo, stellis nebulosis, ... Galileo Galileo : nuper a se reperti beneficio sunt observata in apprime vero in quatuor planetis circa Iovis stellam disparibus intervallis, atque periodis, celeritate mirabili circumvolutis ... atque Medicea sidera nuncupandos decrevit.* Galileo Galilei, 1610. DOI: 10.3931/e-rara-695.

[40] C. Goddi et al. "First M87 Event Horizon Telescope Results and the Role of ALMA". In: *The Messenger* 177 (Sept. 2019), pp. 25–35. arXiv: 1910.10193 [astro-ph.HE].

[41] T. Gold. "Rotating Neutron Stars as the Origin of the Pulsating Radio Sources". In: *Nature* 218.5143 (May 1968), pp. 731–732. DOI: 10.1038/218731a0.

[42] J. P. Hamaker. "Understanding radio polarimetry". In: *Astronomy and Astrophysics Supplement Series* 143(3) (2000), 515–534. DOI: 10.1051/aas:2000337.

[43] J. L. Han, R. N. Manchester, A. G. Lyne, G. J. Qiao, and W. V. Straten. "Pulsar Rotation Measures and the Large-Scale Structure of the Galactic Magnetic Field". In: *The Astrophysical Journal* 642(2) (2006), 868–881. DOI: 10.1086/501444.

[44] J. L. Han, R. N. Manchester, W. V. Straten, and P. Demorest. "Pulsar Rotation Measures and Large-scale Magnetic Field Reversals in the Galactic Disk". In: *The Astrophysical Journal Supplement Series* 234(1) (2018), p. 11. DOI: 10.3847/1538-4365/aa9c45.

[45] S. W. Hawking. "Particle creation by black holes". In: *Communications in Mathematical Physics* 43.3 (Aug. 1975), pp. 199–220. DOI: 10.1007/BF02345020.

[46] A. Hewish, S. J. Bell, J. D. H. Pilkington, P. F. Scott, and R. A. Collins. "Observation of a Rapidly Pulsating Radio Source". In: *Nature* 217.5130 (Feb. 1968), pp. 709–713. DOI: 10.1038/217709a0.

[47] G. Hobbs et al. "An ultra-wide bandwidth (704 to 4032 MHz) receiver for the Parkes radio telescope". In: *Publications of the Astronomical Society of Australia* 37 (2020). DOI: 10.1017/pasa.2020.2.

[48] G. Hobbs et al. "The International Pulsar Timing Array project: using pulsars as a gravitational wave detector". In: *Classical and Quantum*

Gravity 27.8, 084013 (Apr. 2010), p. 084013. DOI: 10.1088/0264-9381/27/8/084013. arXiv: 0911.5206 [astro-ph.SR].

[49] G. Hobbs et al. "The International Pulsar Timing Array project: using pulsars as a gravitational wave detector". In: *Classical and Quantum Gravity* 27 (2010). DOI: 10.1088/0264-9381/27/8/084013.

[50] G. Hobbs et al. "The Parkes Observatory Pulsar Data Archive". In: *Publications of the Astronomy Society of Australia* 28.3 (Aug. 2011), pp. 202–214. DOI: 10.1071/AS11016. arXiv: 1105.5746 [astro-ph.IM].

[51] G. B. Hobbs, R. T. Edwards, and R. N. Manchester. "TEMPO2, a new pulsar-timing package - I. An overview". In: *Monthly Notices of the RAS* 369.2 (June 2006), pp. 655–672. DOI: 10.1111/j.1365-2966.2006.10302.x. arXiv: astro-ph/0603381 [astro-ph].

[52] G. B. Hobbs et al. "Gravitational-Wave Detection Using Pulsars: Status of the Parkes Pulsar Timing Array Project". In: *Publications of the Astron. Soc. of Australia* 26.2 (June 2009), pp. 103–109. DOI: 10.1071/AS08023. arXiv: 0812.2721 [astro-ph].

[53] A. Hotan, W. V. Straten, and R. N. Manchester. "psrchive and psrfits: An Open Approach to Radio Pulsar Data Storage and Analysis". In: *Publications of the Astronomical Society of Australia* 21(3) (2004), 302–309. DOI: 10.1071/as04022.

[54] A. W. Hotan, M. Bailes, and S. M. Ord. "PSR J1022+1001: profile stability and precision timing". In: *Monthly Notices of the Royal Astronomical Society* 355(3) (2004), pp. 941–949. DOI: 10.1111/j.1365-2966.2004.08376.x.

[55] R. A. Hulse and J. H. Taylor. "Discovery of a pulsar in a binary system." In: *Astrophysical Journal, Letters* 195 (Jan. 1975), pp. L51–L53. DOI: 10.1086/181708.

[56] J. Hurley. *Centre for Astrophsyics and Supercomputing*. URL: https://astronomy.swin.edu.au/supercomputing/.

[57] S. Johnston et al. "Discovery of a very bright, nearby binary millisecond pulsar". In: *Nature* 361(6413) (1993), pp. 613–615. DOI: 10.1038/361613a0.

[58] M. Kerr et al. "The Parkes Pulsar Timing Array project: second data release". In: *Publications of the Astronomical Society of Australia* 37 (2020), e020. DOI: 10.1017/pasa.2020.11.

[59] R. P. Kerr. "Gravitational Field of a Spinning Mass as an Example of Algebraically Special Metrics". In: *Physical Review Letters* 11.5 (Sept. 1963), pp. 237–238. DOI: 10.1103/PhysRevLett.11.237.

[60] M. Kramer et al. "Tests of General Relativity from Timing the Double Pulsar". In: *Science* 314.5796 (Oct. 2006), pp. 97–102. DOI: 10.1126/science.1132305. arXiv: astro-ph/0609417 [astro-ph].

[61] M. Kramer et al. "The Double Pulsar – A New Testbed for Relativistic Gravity". In: *Binary Radio Pulsars*. Ed. by Fred A. Rasio and Ingrid H. Stairs. Vol. 328. Astronomical Society of the Pacific Conference Series. July 2005, p. 59. arXiv: astro-ph/0405179 [astro-ph].

[62] J. M. Lattimer and M. Prakash. "The equation of state of hot, dense matter and neutron stars". In: *Physics* 621 (Mar. 2016), pp. 127–164. DOI: 10.1016/j.physrep.2015.12.005. arXiv: 1512.07820 [astro-ph.SR].

[63] J. M. Lattimer and M. Prakash. "The Physics of Neutron Stars". In: *Science* 304.5670 (Apr. 2004), pp. 536–542. DOI: 10.1126/science.1090720. arXiv: astro-ph/0405262 [astro-ph].

[64] P. Lazarus. *coastguard*. 2006. URL: https://github.com/plazar/coastguard.

[65] P. Lazarus et al. "Prospects for high-precision pulsar timing with the new Effelsberg PSRIX backend". In: *Monthly Notices of the Royal Astronomical Society* 458.1 (May 2016), pp. 868–880. DOI: 10.1093/mnras/stw189. arXiv: 1601.06194 [astro-ph.IM].

[66] L. Lentati et al. "European Pulsar Timing Array limits on an isotropic stochastic gravitational-wave background". In: *Monthly Notices of the RAS* 453.3 (Nov. 2015), pp. 2576–2598. DOI: 10.1093/mnras/stv1538. arXiv: 1504.03692 [astro-ph.CO].

[67] L. Lentati et al. "temponest: a Bayesian approach to pulsar timing analysis". In: *Monthly Notices of the Royal Astronomical Society* 437(3) (2013), 3004–3023. DOI: 10.1093/mnras/stt2122.

[68] LIGO Scientific Collaboration et al. "Advanced LIGO". In: *Classical and Quantum Gravity* 32.7, 074001 (Apr. 2015), p. 074001. DOI: 10.1088/0264-9381/32/7/074001. arXiv: 1411.4547 [gr-qc].

[69] K. Liu et al. "Prospects for high-precision pulsar timing". In: *Monthly Notices of the Royal Astronomical Society* 417(4) (2001), 2916–2926. DOI: 10.1111/j.1365-2966.2011.19452.x.

[70] D. R. Lorimer. "Binary and Millisecond Pulsars". In: *Living Reviews in Relativity* 11 (Nov. 2008), p. 8. DOI: 10.12942/lrr-2008-8. arXiv: 0811.0762 [astro-ph].

[71] D. R. Lorimer and M. Kramer. *Handbook of pulsar astronomy*. Cambridge University Press, 2012.

[72] D. R. Lorimer et al. "Four new millisecond pulsars in the galactic disk". In: *The Astrophysical Journal* 439 (1995), p. 933. DOI: 10.1086/175230.

[73] A. G. Lyne and F. Graham-Smith. *Pulsar astronomy*. Cambridge Univ. Pr., 1990.

[74] M. Maggiore. "Gravitational wave experiments and early universe cosmology". In: *Physics Reports* 331.6 (July 2000), pp. 283–367. DOI: 10.1016/S0370-1573(99)00102-7. arXiv: gr-qc/9909001 [gr-qc].

[75] D. Manchester et al. "The Parkes multi-beam pulsar survey - I. Observing and data analysis systems, discovery and timing of 100 pulsars". In: *Monthly Notices of the Royal Astronomical Society* 328(1) (2001), 17–35. DOI: doi:10.1046/j.1365-8711.2001.04751.x.

[76] R. N. Manchester, G. B. Hobbs, A. Teoh, and M. Hobbs. "The Australia Telescope National Facility Pulsar Catalogue". In: *Astronomical Journal* 129.4 (Apr. 2005), pp. 1993–2006. DOI: 10.1086/428488. arXiv: astro-ph/0412641 [astro-ph].

[77] R. N. Manchester et al. "The Parkes Pulsar Timing Array Project". In: *Publications of the Astron. Soc. of Australia* 30, e017 (Jan. 2013), e017. DOI: 10.1017/pasa.2012.017. arXiv: 1210.6130 [astro-ph.IM].

[78] C. F. McKee and E. C. Ostriker. "Theory of Star Formation". In: *Annual Review of Astron and Astrophys* 45.1 (Sept. 2007), pp. 565–687. DOI: 10.1146/annurev.astro.45.051806.110602. arXiv: 0707.3514 [astro-ph].

[79] H. Middleton, W. Del Pozzo, W. M. Farr, A. Sesana, and A. Vecchio. "Astrophysical constraints on massive black hole binary evolution from pulsar timing arrays". In: *Monthly Notices of the RAS* 455.1 (Jan. 2016), pp. L72–L76. DOI: 10.1093/mnrasl/slv150. arXiv: 1507.00992 [astro-ph.CO].

[80] C. M. F. Mingarelli and A. B. Mingarelli. "Proving the short-wavelength approximation in Pulsar Timing Array gravitational-wave background searches". In: *Journal of Physics Communications* 2.10, 105002 (Oct. 2018), p. 105002. DOI: 10.1088/2399-6528/aae06d. arXiv: 1806.06979 [astro-ph.IM].

[81] A. Motte. "The Mathematical Principles of Natural Philosophy". In: (1729). URL: https://en.wikisource.org/wiki/The_Mathematical_Principles_of_Natural_Philosophy_(1846).

[82] I. Newton. *Philosophiae Naturalis Principia Mathematica. Auctore Js. Newton*. Jussu Societatis Regiae ac Typis Josephi Streater, 1687. DOI: 10.3931/e-rara-440.

[83] K. Nordtvedt. "Equivalence Principle for Massive Bodies Including Rotational Energy and Radiation Pressure". In: *Physical Review* 180.5 (Apr. 1969), pp. 1293–1298. DOI: 10.1103/PhysRev.180.1293.

[84] A. Noutsos et al. "Recent and Future Measurements of Pulsar Rotation Measures and the Structure of the Large-Scale Galactic Magnetic Field". In: *The Astrophysical Journal* (2011). DOI: 10.1063/1.3615089.

[85] J. R. Oppenheimer and G. M. Volkoff. "On Massive Neutron Cores". In: *Physical Review* 55.4 (Feb. 1939), pp. 374–381. DOI: 10.1103/PhysRev.55.374.

[86] S. M. Ord, B. A. Jacoby, A. W. Hotan, and M. Bailes. "High-precision timing of PSR J1600-3053". In: *Monthly Notices of the Royal Astronomical Society* 371(1) (2006), pp. 337–342. DOI: doi:10.1111/j.1365-2966.2006.10646.x.

[87] F. Pacini. "Rotating Neutron Stars, Pulsars and Supernova Remnants". In: *Nature* 219.5150 (July 1968), pp. 145–146. DOI: 10.1038/219145a0.

[88] *Parkes 64 metre radio telescope: COSMOS*. URL: http://astronomy.swin.edu.au/cosmos/P/Parkes+64+metre+radio+telescope.

[89] *Parkes radio-telescope gets an upgrade*. URL: https://cosmosmagazine.com/space/parkes-radio-telescope-gets-an-upgrade.

[90] A. Parthasarthy et al. "Timing of young radio pulsars I: Timing noise, periodic modulation and proper motion". In: *Monthly Notices of the Royal Astronomical Society* (2019). DOI: 10.1093/mnras/stz2383.

[91] H. Pasan and K. A. I. L. Gamalath. "Simulation of Rotating Black Holes". In: 114 (Nov. 2018), pp. 106–125.

[92] T. T. Pennucci. "Frequency-dependent Template Profiles for High-precision Pulsar Timing". In: *The Astrophysical Journal* 871(1) (2019), p. 34. DOI: 10.3847/1538-4357/aaf6ef.

[93] M. A. C. Perryman et al. "The Hipparcos Catalogue." In: *Astronomy and Astrophysics* 500 (July 1997), pp. 501–504.

[94] *PSRCHIVE user documentation: pac.* URL: http://psrchive.sourceforge.net/manuals/pac/.

[95] V. Radhakrishnan and D. J. Cooke. "Magnetic Poles and the Polarization Structure of Pulsar Radiation". In: *Astrophysical Letters* 3 (Jan. 1969), p. 225.

[96] R. Ramachandran and M. Kramer. "Unusual profile variations in pulsar PSR J1022+1001 – Evidence for magnetospheric "return currents"?" In: *Astronomy and Astrophysics* 407 (2003), 1085–1095. DOI: 10.1051/0004-6361:20031036.

[97] S. M. Ransom. "Pulsars are cool. Seriously." In: *Neutron Stars and Pulsars: Challenges and Opportunities after 80 years*. Ed. by Joeri van Leeuwen. Vol. 291. IAU Symposium. Mar. 2013, pp. 3–10. DOI: 10.1017/S1743921312023046. arXiv: 1211.3138 [astro-ph.HE].

[98] D. H. Roberts and P. A. Sturrock. "The Braking Index and Period-Pulse Distribution of Pulsars." In: *Astrophysical Journal* 172 (Mar. 1972), p. 435. DOI: 10.1086/151363.

[99] H. N. Russell. "Relations Between the Spectra and Other Characteristics of the Stars". In: *Popular Astronomy* 22 (June 1914), pp. 331–351.

[100] N. Sahu, A. W. Graham, and B. L. Davis. "Black Hole Mass Scaling Relations for Early-type Galaxies. I. M BH-M, sph and M BH-M, gal".

In: *The Astrophysical Journal* 876(2) (2019), p. 155. DOI: 10.3847/1538-4357/ab0f32.

[101] J. S. Sandhu et al. "The Proper Motion and Parallax of PSR J0437-4715". In: *The Astrophysical Journal Letters* 478 (1997), pp. L95–L98. DOI: 10.1086/310562.

[102] M. Sasaki, T. Suyama, T. Tanaka, and S. Yokoyama. "Primordial Black Hole Scenario for the Gravitational-Wave Event GW150914". In: *Physical Review Letters* 117.6, 061101 (Aug. 2016), p. 061101. DOI: 10.1103/PhysRevLett.117.061101. arXiv: 1603.08338 [astro-ph.CO].

[103] M. Schmidt. "3C 273 : A Star-Like Object with Large Red-Shift". In: *Nature* 197.4872 (Mar. 1963), p. 1040. DOI: 10.1038/1971040a0.

[104] K. Schwarzschild. "On the Gravitational Field of a Point Mass According to Einstein's Theory". In: American Association of Physics Teachers, 1982, p. 19.

[105] A. Sesana, A. Vecchio, and C. N. Colacino. "The stochastic gravitational-wave background from massive black hole binary systems: implications for observations with Pulsar Timing Arrays". In: *Monthly Notices of the RAS* 390.1 (Oct. 2008), pp. 192–209. DOI: 10.1111/j.1365-2966.2008.13682.x. arXiv: 0804.4476 [astro-ph].

[106] N. I. Shakura and R. A. Sunyaev. "Reprint of 1973A&A....24..337S. Black holes in binary systems. Observational appearance." In: *Astronomy and Astrophysics* 500 (June 1973), pp. 33–51.

[107] R. M. Shannon et al. "Limitations in timing precision due to single-pulse shape variability in millisecond pulsars". In: *Monthly Notices of the Royal Astronomical Society* 443(2) (2014), 1463–1481. DOI: 10.1093/mnras/stu1213.

[108] S. L. Shapiro and S. A. Teukolsky. *Black holes, white dwarfs, and neutron stars : the physics of compact objects*. Wiley-VCH, 1983.

[109] F. H. Shu, F. C. Adams, and S. Lizano. "Star formation in molecular clouds: observation and theory." In: *Annual Review of Astron and Astrophys* 25 (Jan. 1987), pp. 23–81. DOI: 10.1146/annurev.aa.25.090187.000323.

[110] *Slurm: Creating a Job*. URL: https://supercomputing.swin.edu.au/docs/2-ozstar/oz-slurm-create.html.

[111] I. H. Stairs. "Pulsar Observations II. – Coherent Dedispersion Polarimetry, and Timing". In: *Single-Dish Radio Astronomy: Techniques and Applications*. Ed. by S. Stanimirovic, D. Altschuler, P. Goldsmith, and C. Salter. Vol. 278. Astronomical Society of the Pacific Conference Series. 2002, pp. 251–269.

[112] I. H. Stairs. "Testing General Relativity with Pulsar Timing". In: *Living Reviews in Relativity* 6.1, 5 (Sept. 2003), p. 5. DOI: 10.12942/lrr-2003-5. arXiv: astro-ph/0307536 [astro-ph].

[113] I. H. Stairs et al. "Measurement of Relativistic Orbital Decay in the PSR B1534+12 Binary System". In: *Astrophysical Journal* 505.1 (Sept. 1998), pp. 352–357. DOI: 10 . 1086 / 306151. arXiv: astro-ph/9712296 [astro-ph].

[114] L. Staveley-Smith et al. "The Parkes 21 cm Multibeam Receiver". In: *Publications of the Astronomical Society of Australia* 13(3) (1996), 243–248. DOI: 10.1017/s1323358000020919.

[115] G. G. Stokes. "On the Change of Refrangibility of Light". In: *Mathematical and Physical Papers* (1852), 267–414. DOI: 10.1017/cbo9780511702266.012.

[116] W. V. Straten. *psrpl download and configure*. URL: http://psrchive.sourceforge.net/manuals/psrpl/download.shtml.

[117] *Submitting Jobs*. URL: https://supercomputing.swin.edu.au/g2/user-guide/submitting-jobs/.

[118] J. H. Taylor and J. M. Cordes. "Pulsar Distances and the Galactic Distribution of Free Electrons". In: *Astrophysical Journal* 411 (July 1993), p. 674. DOI: 10.1086/172870.

[119] J. H. Taylor, R. N. Manchester, and A. G. Lyne. "Catalog of 558 Pulsars". In: *Astrophysical Journals* 88 (Oct. 1993), p. 529. DOI: 10.1086/191832.

[120] J. H. Taylor and J. M. Weisberg. "Further Experimental Tests of Relativistic Gravity Using the Binary Pulsar PSR 1913+16". In: *Astrophysical Journal* 345 (Oct. 1989), p. 434. DOI: 10.1086/167917.

[121] R. C. Tolman. "Static Solutions of Einstein's Field Equations for Spheres of Fluid". In: *Physical Review* 55.4 (Feb. 1939), pp. 364–373. DOI: 10.1103/PhysRev.55.364.

[122] M. Vallisneri et al. "Modelling the Uncertainties of Solar System Ephemerides for Robust Gravitational-wave Searches with Pulsar-timing Arrays". In: *The Astrophysical Journal* 893 (2020), p. 112. DOI: 10.3847/1538-4357/ab7b67.

[123] W. van Straten. "High-fidelity Radio Astronomical Polarimetry Using a Millisecond Pulsar as a Polarized Reference Source". In: *Astrophysical Journal, Supplement* 204.1, 13 (Jan. 2013), p. 13. DOI: 10.1088/0067-0049/204/1/13. arXiv: 1212.3446 [astro-ph.IM].

[124] W. van Straten. "Radio Astronomical Polarimetry and High-Precision Pulsar Timing". In: *Astrophysical Journal* 642.2 (May 2006), pp. 1004–1011. DOI: 10.1086/501001. arXiv: astro-ph/0510334 [astro-ph].

[125] W. van Straten. "Radio Astronomical Polarimetry and Point-Source Calibration". In: *Astrophysical Journal, Supplement* 152.1 (May 2004), pp. 129–135. DOI: 10 . 1086 / 383187. arXiv: astro-ph/0401536 [astro-ph].

[126] W. van Straten et al. "A test of general relativity from the three-dimensional orbital geometry of a binary pulsar". In: *Nature* 412.6843 (July 2001), pp. 158–160. arXiv: astro-ph/0108254 [astro-ph].

[127] J. P. W. Verbiest et al. "Precision Timing of PSR J0437-4715: An Accurate Pulsar Distance, a High Pulsar Mass, and a Limit on the Variation of Newton's Gravitational Constant". In: *The Astrophysical Journal* 679(1) (2008), pp. 675–680. DOI: 10.1086/529576.

[128] J. P. W. Verbiest et al. "Timing stability of millisecond pulsars and prospects for gravitational-wave detection". In: *Monthly Notices of the Royal Astronomical Society* 400(2) (2009), pp. 951–968. DOI: 10.1111/j.1365-2966.2009.15508.x.

[129] J. Weber. "Detection and Generation of Gravitational Waves". In: *Physical Review* 117.1 (Jan. 1960), pp. 306–313. DOI: 10.1103/PhysRev.117.306.

[130] J. M. Weisberg and J. H. Taylor. "Gravitational radiation from an orbiting pulsar." In: *General Relativity and Gravitation* 13.1 (Jan. 1981), pp. 1–6. DOI: 10.1007/BF00766292.

[131] J. Whelan and I. Iben. "Binaries and Supernovae of Type I". In: *Astrophysical Journal* 186 (Dec. 1973), pp. 1007–1014. DOI: 10.1086/152565.

[132] C. M. Will. "Theoretical Frameworks for Testing Relativistic Gravity. II. Parametrized Post-Newtonian Hydrodynamics, and the Nordtvedt Effect". In: *The Astrophysical Journal* 163 (1971), p. 611. DOI: 10.1086/150804.

[133] S. E. Woosley and T. A. Weaver. "The Evolution and Explosion of Massive Stars. II. Explosive Hydrodynamics and Nucleosynthesis". In: *The Astrophysical Journal Supplement Series* 101 (1995), p. 181. DOI: 10.1086/192237.